Enlightening the dark

Exploring the dark sector with gamma-rays and neutrinos

Klop, L.B.

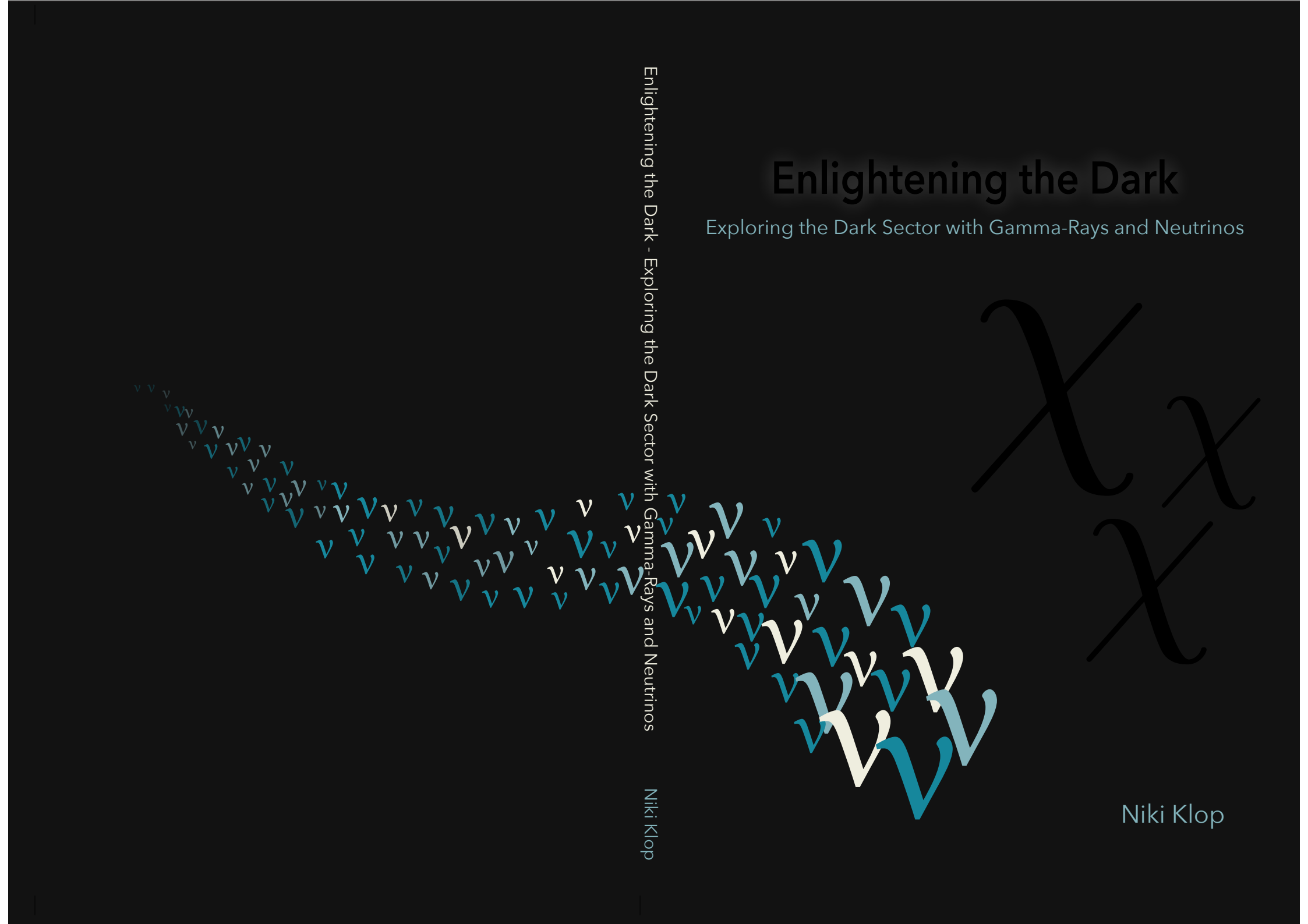
Enlightening the Dark
Exploring the Dark Sector with Gamma-Rays and Neutrinos
Niki Klop
Enlightening the Dark - Exploring the Dark Sector with Gamma-Rays and Neutrinos
Niki Klop

Enlightening the Dark

Exploring the Dark Sector with Gamma-Rays and Neutrinos

This work has been accomplished at the Gravity and AstroParticle Physics in Amsterdam (GRAPPA) center of excellence and the Institute for Theoretical Physics (ITFA) of the University of Amsterdam (UvA).

Cover design: Robbie Rens

ISBN 978-94-6323-454-2

Enlightening the Dark

Exploring the Dark Sector with Gamma-Rays and Neutrinos

ACADEMISCH PROEFSCHRIFT

ter verkrijging van de graad van doctor
aan de Universiteit van Amsterdam
op gezag van de Rector Magnificus
prof. dr. ir. K.I.J. Maex
ten overstaan van een door het College
voor Promoties ingestelde commissie,
in het openbaar te verdedigen in de Agnietenkapel
op donderdag 17 januari 2019, te 14.00 uur

door

Lydia Bernice Klop

geboren te Oud-Beijerland

Promotiecommissie

Promotor		
	dr. S. Ando	Universiteit van Amsterdam
Co-Promotor		
	dr. G. Bertone	Universiteit van Amsterdam
Overige leden		
	Prof. dr. M.P. Decowski	Universiteit van Amsterdam
	Prof. dr. S.B. Markoff	Universiteit van Amsterdam
	Prof. dr. A.P. Colijn	Universiteit van Amsterdam, Universiteit Utrecht
	Prof. dr. L. Baudis	University of Zurich
	dr. I. Tamborra	University of Copenhagen
	dr. F. Calore	Laboratoire d'Annecy-le-Vieux de Physique Theorique

Faculteit der Natuurwetenschappen, Wiskunde en Informatica

Publications

This thesis is based on the following publications:

[1] N. Klop, F. Zandanel, K. Hayashi and S. Ando, *Impact of axisymmetric mass models for dwarf spheroidal galaxies on indirect dark matter searches*, *Phys. Rev. D* **95** 123012 (2017), `arXiv:1609.03509`.

Presented in Chapter **2**.

KH provided the data for the axisymmetric halo models. NK performed all calculations and the analysis, under supervision of FZ and SA. The paper is written primarily by NK, with input from FZ and SA. KH contributed to the section on the axisymmetric mass models.

[2] N. Klop and S. Ando, *Effects of a neutrino–dark energy coupling on oscillations of high-energy neutrinos*, *Phys. Rev. D* **97** 063006 (2018), `arXiv:1712.05413`.

Presented in Chapter **4**.

NK performed all calculations and the analysis, under supervision of SA. The paper is primarily written by NK, with input from SA.

[3] N. Klop and S. Ando, *Constraints on MeV dark matter using neutrino detectors and their implication for the 21-cm results*, *Phys. Rev. D* **98** 103004 (2018), `arXiv:1809.00671`.

Presented in Chapter **3**.

NK performed all calculations and the analysis, under supervision of SA. The paper is primarily written by NK, with input from SA.

Contents

Preface

In this thesis, I discuss the research that I performed during my PhD position at the Gravitational Astroparticle Physics Amsterdam (GRAPPA) institute at the University of Amsterdam. The work involves the two most interesting particles in the Universe: neutrinos and dark matter (DM). The physics of neutrinos is one of the most exciting topics in contemporary physics. The Standard Model picture changed drastically when flavor oscillations were observed and confirmed by various experiments over the last decades, and neutrinos turned out to have mass. The latter is the most interesting particle outside the SM, if it is a particle at all, keeping physicists all over the world occupied already for several decades, trying to reveal their nature and solve the problem of the missing mass in the Universe. Rather than studying the properties of the neutrino itself, we employed its properties as a method to detect dark matter and dark energy.

In this thesis we explore several aspects of the dark sector. In chapter 1, I briefly introduce the standard model, and give an introduction of dark matter and neutrinos. For both I provide a brief historic overview and discuss the topics relevant to the work performed for this thesis. In chapter 2, I discuss the work we performed on dark matter searches in dwarf spheroidal galaxies. Usually, a spherical NFW profile is assumed for the mass distribution in DM analyses of the dwarf galaxies. We investigated the impact of observational motivated axisymmetric mass models on indirect dark matter searches using gamma-rays, compared to the general NFW profile.
Chapter 3 covers our work on indirect detection of light DM using neutrino detectors, in the context of the recent 21-cm results.
Chapter 4 describes our work related to another subject in the dark sector: dark energy. If dark energy is a scalar field rather than a cosmological constant, it could undergo interactions with neutrinos. We explore the effect of a dark energy-neutrino coupling on neutrino oscillations, and the impact on the flavor ratio of astrophysical neutrinos measured at Earth.

In chapter 5, I discuss my conclusions and outlook. I also provide a popular summary of my thesis in both English and Dutch.

1 Introduction

In the work performed for this thesis, we explored multiple topics in the dark sector, using gamma-rays and neutrinos. In this chapter we briefly introduce the topics necessary to understand the thesis. To get familiar with the building blocks of the Universe, we briefly discuss the Standard Model of particle physics and cosmology in section 1. In section 2 we give a historic overview of the neutrino and discuss the theory behind neutrino oscillation. We introduce the field of neutrino astronomy and review several experiments. Finally, we explain how the study of high-energy astrophysical neutrinos can tell us about physics beyond the standard model. In section 3 we briefly review the history of DM, discuss the possible candidates and how we attempt to detect it. Furthermore, we discuss the DM density distribution and some recent observations in favor of DM.

1 The Standard Model

The elementary particles and their interactions, except for the gravitational, are described in the Standard Model (SM) of particle physics [4, 5]. The particles in the standard model consist of fermions, which have half-integer spin, and bosons, which have integer spin. Fermions are what make up the matter, while bosons mediate the interactions. The strong interactions, described by the gauge group $SU(3)_C$, are mediated by eight massless gluons. Weak interactions are mediated through the W^+, W^- and Z bosons, and the electromagnetic interaction is mediated by γ, the photon. These two interactions are described together by the symmetry group $SU(2)_L \times U(1)_Y$ as the electroweak interaction. The Higgs boson is associated with the symmetry break-

ing of $SU(2)_L \times U(1)_Y$, generating the mass of the massive SM particles through the *Brout-Englert-Higgs mechanism* [6, 7], or *Higgs mechanism* in short. There are two families of fermions, the quarks and the leptons. Quarks participate in all interactions, while fermions do not interact in strong interactions. Because neutrinos are neutral, they only participate in the weak interactions. The fermions can be divided into three generations that show, except for their mass, identical properties. In table 1.1, a schematic overview is given of the particles in the SM.

	Fermions			**Bosons**	
	I	**II**	**III**		
Quarks	u (up)	c (charm)	t (top)	g (gluon)	H (Higgs)
	d (down)	s (strange)	b (bottom)	γ (photon)	
Leptons	e (electron)	μ (muon)	τ (tau)	Z (Z boson)	
	ν_e (electron neutrino)	ν_μ (muon neutrino)	ν_τ (tau neutrino)	$W^\pm$ (W boson)	

Table 1.1: The Standard Model of particle physics.

However, the SM turns out not to be complete. For instance, the Higgs mechanism giving mass to the SM particles involves both their left- and right-handed fields. Since we only observe left-handed neutrinos, neutrinos can not have mass in the SM. We explain more about the physics of neutrinos in section 2 of this chapter. Furthermore, one of the main topics of this thesis is dark matter, which can not be explained by the SM as well. In section 3 we will go deeper into the details of DM. Besides these, many other problems suggest the need of SM extensions.

Besides the standard model of particle physics, physicists sometimes also refer to the standard model of cosmology, which is the ΛCDM model (*Lambda cold dark matter*). ΛCDM describes the cosmological Big Bang model, including cold dark matter (see section 3) and a cosmological constant, Λ, which is a constant energy density associated with Dark Energy (DE), inducing the (accelerating) expansion of the Universe [8]. Dark energy could also be dynamical, in the form of a scalar field rather than a cosmological constant, such as quintessence [9]. In chapter 4 we explore the effects of a possible coupling between scalar-field DE and neutrinos on neutrino oscillations. Observations of the Planck satellite tell us that the current energy density of the Universe consists for 4.9% of normal matter, for 26.8% of dark matter, and for 68.3% of dark energy [10].

2 Neutrinos

2.1 Historic Overview

Many people will agree that neutrinos are the most interesting particles in the Standard Model. Almost 90 years after their prediction, their nature and behaviour are still not fully understood. They are the only particles that have properties beyond the SM: they have masses and they mix. Besides this, they play a role in many theories beyond the SM. Because of this, neutrino physics is nowadays still a very interesting and active field of research.

Neutrinos were first proposed by Pauli in 1930, to solve the problem of the seemingly violation of energy conservation observed in beta decay [11]. In beta decay, an electron is emitted as a nucleus with atomic number Z decays into a less massive nucleus with atomic number $Z + 1$. Due to energy and momentum conservation, it was expected that the kinetic energy transferred by the electron would have a fixed, well defined value, given by the mass difference of the two nuclei. Instead of the expected monochromatic electron energy spectrum, a continuous spectrum was observed. To solve this, Pauli proposed a light, neutral spin–$\frac{1}{2}$ particle that is released together with the electron, sharing the released energy. This way the new particle, a neutrino, was able to explain the missing energy and the continuous spectrum [12, 13].

Neutrinos are neutral, approximately massless leptons that take part in weak interactions. Since they interact with matter very weakly, most neutrinos pass through without interactions. This makes it hard to detect them. To increase the probability to detect one of them, one needs a source that produces a large flux of neutrinos, and the detector needs to be very sensitive and shielded from backgrounds such as cosmic rays.

The neutrino was only detected for the first time in the 1950s, by Frederick Reines and Clyde Cowan [14]. At that time, two of the three charged leptons, the electron and the muon and their opposite charged antiparticles, were already known and could be distinguished in experiments due to their difference in mass. Some time later, Ray Davis performed an experiment in which he tried to observe a process involving neutrinos, using a source that emitted anti-neutrinos [15]. A positive result would have implied that neutrinos and anti-neutrinos are identical, which turned out not to be the case. Thereafter, the Brookhaven experiment in 1962 proved that electron and muon neutrinos are distinguishable particles [16]. This was done by investigating if the neutrinos produced in pion decays could be converted into electrons. Pions

decay through the reaction $\pi \rightarrow \mu + \nu$, always resulting in a muon, never in an electron. This proved that the neutrinos involved in electron and muon interactions are not identical and that the lepton number in interactions is conserved separately for the individual flavor families. In the 1950s, the Wu experiment discovered parity violation of the weak interactions [17], which led to the development of the $V - A$ theory. As a response on the results of this experiment, Lee and Yang postulated that all neutrinos are left-handed and all anti-neutrinos are right-handed [18]. The measurement of the neutrino helicity one year later confirmed this picture [13]. The Standard Model of particle physics that was developed in the 1970s incorporated this view, describing a framework of three massless left-handed neutrinos, associated with the three charged leptons, e, μ and τ. They only participate in weak interactions, in which lepton number is conserved separately for the distinct families. The left-handed neutrinos and the right-handed antineutrinos are distinguishable particles.

However, already in the 1950s, Bruno Pontecorvo brought up the idea that $\nu \rightarrow \bar{\nu}$ transitions could take place as an analogy to the neutral kaon mixing of K^0 and $\bar{K}^0$ [19, 20, 21]. In the 1960s, this idea of neutrino transitions was developed further by, among others, Maki, Nakagawa, Sakata and Pontecorvo into a model more similar to the mixing in the quark sector. In this model, neutrinos are massive and the flavor neutrinos can be expressed as a linear combination of the massive neutrino states [21, 22]. And indeed, over the past decades, neutrino oscillation has been observed and confirmed by many experiments in neutrinos from different sources [23, 24]. As a consequence, the picture of the neutrino as we knew it had to change drastically; For example, a neutrino that starts as an electron neutrino can transform through mixing into a muon neutrino, which could have interactions resulting into a muon. This violates the conservation of lepton number for the separate flavor families. Furthermore, neutrinos are not massless as assumed in the SM. These masses in their turn could have a Majorana origin, which would imply that neutrinos and anti-neutrinos are identical and that lepton number is violated. Hence the discovery of neutrino oscillation opened a window to a whole new area in particle physics.
Nowadays, a coherent picture has been formed of the standard framework, in which three flavor neutrino states mix with three massive neutrino states, while the actual values of the neutrino masses and the nature of the neutrino (Majorana or Dirac) still have to be determined.

2.2 Neutrino masses and mixing

In this section we discuss the theory of neutrino mixing, largely following [5].
In the minimal version of the SM, neutrinos are described in the leptonic part of the SM Lagrangian:

$$\mathcal{L}_{\text{leptonic}} = i \sum_{\alpha=e,\mu,\tau} \overline{L}_{\alpha L} \not{\partial} L_{\alpha L} + i \sum_{\alpha=e,\mu,\tau} \overline{\ell}_{\alpha R} \not{\partial} \ell_{\alpha R} - \sum_{\alpha,\beta=e,\mu,\tau} Y^{\ell}_{\alpha\beta} \overline{L}_{\alpha L} \Phi \ell_{\beta R} + \text{H.c.}, \tag{1.1}$$

where Φ is the Higgs doublet, $Y^{\ell}_{\alpha\beta}$ are the Yukawa couplings, and

$$L_{\alpha L} = \begin{pmatrix} \nu_{\alpha L} \\ \ell_{\alpha L} \end{pmatrix}, \qquad \alpha = e, \mu, \tau, \tag{1.2}$$

are the lepton fields.
Since there are no right-handed neutrinos in the SM, the neutrino part of the Lagrangian only has the form

$$\mathcal{L}_{\nu} = i \overline{\nu}_L \not{\partial} \nu_L, \qquad \nu_L = \begin{pmatrix} \nu_{eL} \\ \nu_{\mu L} \\ \nu_{\tau L} \end{pmatrix}, \tag{1.3}$$

where D_μ is the covariant derivative and $\not{\partial} = \gamma^\mu D_\mu$.

According to the SM, neutrinos are neutral particles that only participate in weak interactions. Because fermions get their masses through the Higgs mechanism, their mass term should include couplings to both left- and right-handed fields. Since there are only left-handed neutrinos, according to the SM they are massless particles. Now that we know that neutrinos can oscillate into different flavors and therefore should be massive, the SM Lagrangian must be extended with new physics to include neutrino mass terms.

The oscillation probability

The neutrino flavor eigenstates can be written as a superposition of the neutrino mass eigenstates [5],

$$|\nu_\alpha\rangle = \sum_k U^*_{\alpha k} |\nu_k\rangle \qquad (\alpha = e, \mu, \tau), \tag{1.4}$$

where the weight factors $U_{\alpha k}$ are elements of the *Pontecorvo-Maki-Nakagawa-Sakata matrix* (PMNS matrix), the unitary mixing matrix for neutrinos analogous to the *Cabibbo-Kobayashi-Maskawa matrix* (CKM matrix) for quarks. It is schematically given by

$$U = \begin{bmatrix} U_{e1} & U_{e2} & U_{e3} \\ U_{\mu 1} & U_{\mu 2} & U_{\mu 3} \\ U_{\tau 1} & U_{\tau 2} & U_{\tau 3} \end{bmatrix}. \tag{1.5}$$

Because of the unitarity of the mixing matrix, eq. 1.4 can be inverted to write the mass eigenstates as a superposition of the flavor eigenstates:

$$|\nu_k\rangle = \sum_\alpha U_{\alpha k} |\nu_\alpha\rangle \,. \tag{1.6}$$

In the case of antineutrinos, the terms $U_{\alpha i}$ in equations 1.4 and 1.6 are replaced by $U^*_{\alpha i}$. The neutrino mass eigenstates are eigenstates of the Hamiltonian

$$H |\nu_k\rangle = E_k |\nu_k\rangle \,, \tag{1.7}$$

with eigenvalues $E_k = \sqrt{\vec{p}^{\,2} + m_k^2}$.
Solving the Schrödinger equation

$$i \frac{\mathrm{d}}{\mathrm{d}t} |\nu_k(t)\rangle = H |\nu_k(t)\rangle \tag{1.8}$$

yields the plane-wave solution

$$|\nu_k(t)\rangle = e^{-iE_k t} |\nu_k\rangle \,. \tag{1.9}$$

Substituting equation 1.9 in equation 1.4 results in the time dependent solution for a neutrino in the flavor state,

$$|\nu_\alpha(t)\rangle = \sum_k U^*_{\alpha k} e^{-iE_k t} |\nu_k\rangle \,, \tag{1.10}$$

such that at $t = 0$, the neutrino has a well defined flavor α.

Substituting equation 1.6 in equation 1.10 yields

$$\begin{aligned} |\nu_\alpha(t)\rangle &= \sum_k U^*_{\alpha k} e^{-iE_k t} \sum_\beta U_{\beta k} |\nu_\beta\rangle \\ &= \sum_\beta \left(\sum_k U^*_{\alpha k} e^{-iE_k t} U_{\beta k} \right) |\nu_\beta\rangle \qquad (\beta = e, \mu, \tau, ...). \end{aligned} \tag{1.11}$$

At $t = 0$, the state $|\nu_\alpha(t)\rangle$, which is a certain composition of the different neutrino mass eigenstates, is a pure flavor state of flavor α. However, when $t > 0$, the factor $e^{-iE_k t}$ in front of the mass eigenstates develops over time, which differs for different k, since the eigenvalues E_k of the mass-eigenstates differ for different k. Therefore, the coefficients change differently for the distinct mass-eigenstates and the composition of the flavor state $|\nu_\alpha(t)\rangle$ changes. This flavor state is now a superposition of all three flavor states, and at a certain moment, the ratio of the distinct mass-eigenstates will be equal to the composition of one of the other flavor states. After some period, the values of the coefficients of the mass-eigenstates will return at their original value, and the state is again a neutrino with original flavor α. This periodic mixing process is called *neutrino oscillation*. Oscillation only takes place if the mixing matrix U is non-diagonal, otherwise the distinct flavor states would be equal to the distinct mass-eigenstates and the composition would not change over time.

The amplitude of the transition from ν_α to ν_β as a function of time is defined by the coefficient of $|\nu_\beta\rangle$, in the third line of equation 1.11:

$$A_{\nu_\alpha \to \nu_\beta}(t) = \sum_k U^*_{\alpha k} U_{\beta k} e^{-iE_k t}. \tag{1.12}$$

The oscillation probability, the probability to measure the flavor state ν_β after the traveltime t, is given by:

$$P_{\nu_\alpha \to \nu_\beta} = |\langle \nu_\beta \,|\, \nu_\alpha(t) \rangle|^2 \equiv |A_{\nu_\alpha \to \nu_\beta}(t)|^2 = \sum_{k,j} U^*_{\alpha k} U_{\beta k} U_{\alpha j} U^*_{\beta j} e^{-i(E_k - E_j)t}. \tag{1.13}$$

Neutrinos are relativistic particles. In the relativistic limit, $p \gg m$ and $|\vec{p}| = E$. Therefore, the energy eigenvalues $E_k = \sqrt{\vec{p}^2 + m_k^2}$ can be approximated by

$$E_k \simeq E + \frac{m_k^2}{2E}. \tag{1.14}$$

Such that the energies in the exponent of equation 1.13 now can be written as

$$E_k - E_j \simeq \frac{\Delta m_{kj}^2}{2E}, \quad \text{with} \quad \Delta m_{kj}^2 \equiv m_k^2 - m_j^2. \tag{1.15}$$

Substituting (1.15) in equation 1.13 yields

$$P_{\nu_\alpha \to \nu_\beta}(L, E) = \sum_{k,j} U_{\alpha k}^* U_{\beta k} U_{\alpha j} U_{\beta j}^* \exp\left(-i \frac{\Delta m_{kj}^2 L}{2E}\right), \tag{1.16}$$

where we substituted the neutrino travel time t for the travel length L.

It is useful to separate the probability in components of the real and imaginary parts of the product of the matrix elements:

$$\begin{aligned} P_{\substack{(-)\\ \nu_\alpha \to \nu_\beta}}^{(-)}(L, E) = \delta_{\alpha\beta} &- 4 \sum_{k>j} \Re[U_{\alpha k}^* U_{\beta k} U_{\alpha j} U_{\beta j}^*] \sin^2\left(\frac{\Delta m_{kj}^2 L}{4E}\right) \\ &\pm 2 \sum_{k>j} \Im[U_{\alpha k}^* U_{\beta k} U_{\alpha j} U_{\beta j}^*] \sin\left(\frac{\Delta m_{kj}^2 L}{2E}\right). \end{aligned} \tag{1.17}$$

In this equation, the plus sign corresponds to neutrinos and the minus sign to anti-neutrinos. When neutrino oscillations are considered for the channel in which $\alpha \neq \beta$, the probability is called the *transition probability*. If we consider the probability to measure a neutrino that started with flavor α, to still have flavor α at distance L, we call the probability the *survival probability*.

The oscillation probability depends on the propagation distance L, the neutrino energy E and the squared-mass differences. Neutrino oscillation experiments therefore can only give us information on the values of the squared-mass differences, not on the absolute masses. The phase of the oscillation is determined by

$$\Phi_{kj} = -\frac{\Delta m_{kj}^2 L}{2E}. \tag{1.18}$$

The *oscillation length* is the distance after which the neutrino completed one oscillation period and returned to its original flavor state, i.e. the length L for which the phase is equal to 2π:

$$L_{kj}^{osc} = \frac{4\pi E}{|\Delta m_{kj}^2|} \tag{1.19}$$

The probability is maximal for $L = L_{kj}^{osc}/2$, since this corresponds to a value of $\frac{\pi}{2}$ for the argument of the sine.

The PMNS matrix

A unitary $n \times n$ matrix depends on n^2 independent parameters: $\frac{n(n-1)}{2}$ mixing angles and $\frac{n(n+1)}{2}$ phases. In the case of Dirac neutrinos, the Lagrangian is invariant under the following global phase transformations:

$$\nu_{kL} \to e^{i\phi k}\nu_{kL}, \qquad \nu_{kR} \to e^{i\phi k}\nu_{kR} \qquad (k = 1, 2, 3) \tag{1.20}$$

$$\ell_{\alpha L} \to e^{i\phi\alpha}\ell_{\alpha L}, \qquad \ell_{\alpha R} \to e^{i\phi\alpha}\ell_{\alpha R} \qquad (\alpha = e, \mu, \tau) \tag{1.21}$$

as we can see from the following:

$$\mathcal{L}_{\text{mass}}^{D} = -m\bar{\nu}_R\nu_L + \text{H.C.} \to -me^{-i\phi}\bar{\nu}_R e^{i\phi}\nu_L + \text{H.C.} = -m\bar{\nu}_R\nu_L + \text{H.C.} \tag{1.22}$$

Because of this, $2n - 1$ of these phases can be eliminated, such that a 3×3 Dirac mixing matrix depends on three mixing angles and one CP-violating phase. In the Majorana case, the mass term is not invariant under the phase transformation in equation 1.20:

$$\begin{aligned} \mathcal{L}_{\text{mass}}^{M} = -\frac{1}{2}m\bar{\nu}_L^C\nu_L + \text{H.C.} &\to -\frac{1}{2}me^{i\phi}\bar{\nu}_L^C e^{i\phi}\nu_L + \text{H.C.} \\ &= -\frac{1}{2}e^{2i\phi}m\bar{\nu}_L^C\nu_L + \text{H.C.} \end{aligned} \tag{1.23}$$

Hence in the Majorana case, the mixing matrix depends on two extra Majorana phases, which makes three mixing angles and three CP-violating phases. In this case, the mixing matrix can be written as

$$U = U^D D^M, \tag{1.24}$$

where U^D is the mixing matrix of the Dirac case and D^M is a diagonal unitary matrix with the two independent Majorana phases, $D^M = \text{diag}(e^{i\lambda_1}, e^{i\lambda_2}, e^{i\lambda_3})$, with $\lambda_1 = 0$.

The oscillation probability however is independent of the Majorana phases, since they cancel out in the product of the mixing matrix appearing in the oscillation probability:

$$U^*_{\alpha k}U_{\beta k}U_{\alpha j}U^*_{\beta j} = U^{D*}_{\alpha k}e^{-i\lambda_k}U^D_{\beta k}e^{i\lambda_k}U^D_{\alpha j}e^{i\lambda_j}U^{D*}_{\beta j}e^{-i\lambda_j} = U^{D*}_{\alpha k}U^D_{\beta k}U^D_{\alpha j}U^{D*}_{\beta j}. \quad (1.25)$$

Hence, Majorana phases cannot be measured by neutrino oscillation experiments and the oscillation probability for Dirac and Majorana neutrinos is identical.

The mixing matrix U can be parameterized by the multiplication of the real orthogonal matrices R^{jk}. These matrices perform a rotation of an angle θ_{jk} in the j–k plane. For a 2×2 matrix, they are simply given by:

$$R_{ij} = \begin{bmatrix} c_{ij} & s_{ij} \\ -s_{ij} & c_{ij} \end{bmatrix} \quad , \quad \tilde{R}_{ij} = \begin{bmatrix} c_{ij} & \tilde{s}_{ij} \\ -\tilde{s}^*_{ij} & c_{ij} \end{bmatrix} \quad (1.26)$$
$$s_{ij} = \sin\theta_{ij} \qquad \tilde{s}_{ij} = s_{ij}e^{-i\delta_{ij}}$$
$$c_{ij} = \cos\theta_{ij}$$

For mixing matrices with higher dimensions, the matrices R^{jk} can be constructed from:

$$[R^{jk}]_{rs} = [R^{jk}(\theta_{jk})]_{rs} = \delta_{rs} + (\cos\theta_{jk} - 1)(\delta_{rj}\delta_{sj} + \delta_{rk}\delta_{sk}) + \sin\theta_{jk}(\delta_{rj}\delta_{sk} - \delta_{rk}\delta_{sj}). \quad (1.27)$$

We use the following parameterization, adopted by the Particle Data Group (PDG) [25], for the 3×3 PMNS matrix:

$$U = R_{23}\tilde{R}_{13}R_{12}, \quad (1.28)$$

such that

$$U = \begin{bmatrix} 1 & 0 & 0 \\ 0 & c_{23} & s_{23} \\ 0 & -s_{23} & c_{23} \end{bmatrix} \begin{bmatrix} c_{13} & 0 & s_{13}e^{-i\delta_{CP}} \\ 0 & 1 & 0 \\ -s_{13}e^{i\delta_{CP}} & 0 & c_{13} \end{bmatrix} \begin{bmatrix} c_{12} & s_{12} & 0 \\ -s_{12} & c_{12} & 0 \\ 0 & 0 & 1 \end{bmatrix}, \quad (1.29)$$

yielding the matrix

$$U = \begin{bmatrix} c_{12}c_{13} & c_{13}s_{12} & s_{13}e^{-i\delta_{CP}} \\ -c_{23}s_{12} - c_{12}s_{13}s_{23}e^{i\delta_{CP}} & c_{12}c_{23} - s_{12}s_{13}s_{23}e^{i\delta_{CP}} & c_{13}s_{23} \\ s_{12}s_{23} - c_{12}c_{23}s_{13}e^{i\delta_{CP}} & -c_{12}s_{23} - c_{23}s_{12}s_{13}e^{i\delta_{CP}} & c_{13}c_{23} \end{bmatrix}. \quad (1.30)$$

Neutrino oscillations in matter

When neutrinos travel through matter, they could undergo interactions with the particles in the matter. This was discovered in 1978 by Wolfenstein [26], and some extra resonant effect was discovered by Mikheyev and Smirnov in 1985 [27, 28]. This affects the mixing of the neutrinos, and is called the *Mikheyev-Smirnov-Wolfenstein effect* (MSW effect). In the work performed for this thesis, we considered astrophysical neutrinos traveling mainly through interstellar space, what we could consider as a vacuum with respect to matter effects, which we therefore do not have to take into account. We nevertheless discuss the phenomenon, because we study a similar effect induced by new physics rather than matter in chapter 4.

Propagating through matter, the neutrinos could undergo two types of interactions, namely *coherent forward elastic scattering* and *incoherent scattering*. The effect of incoherent scattering only has to be taken into account for energies above 1 TeV, or in regions with very high nucleon regions, such as neutron stars and supernovae [5]. In most cases, the mean free path of the neutrino is much bigger than the involved travel distances. When the neutrino propagates through matter, the coherent forward elastic scattering induces an effective potential, which modifies the evolution equation of the flavour neutrinos. This potential arises from the coherent forward elastic scattering mediated by the weak charged current (CC) and neutral current (NC). The charged current potential is given by $V_{CC} = \sqrt{2}G_F N_e$, where N_e is the electron number density of the medium and G_F is the Fermi coupling constant ($G_F = 8.98 \times 10^{-44}$ eV m^3). The neutral current potential is given by $V_{NC} = -\frac{1}{2}\sqrt{2}G_F N_n$, where N_n is the neutron number density of the medium.

The vacuum Hamiltonian for the evolution of a neutrino with flavour α gets perturbed by the effective potential

$$V_\alpha = V_{CC}\delta_{\alpha e} + V_{NC} \quad (1.31)$$

such that the total Hamiltonian in matter becomes

$$H = H_0 + H_1, \qquad \text{with} \qquad H_1 |\nu_\alpha\rangle = V_\alpha |\nu_\alpha\rangle, \quad \text{and} \qquad H_0 |\nu_k\rangle = E_k |\nu_k\rangle. \quad (1.32)$$

The oscillation probability for transitions of ν_α to ν_β equals the square of the transition amplitude:

$$P_{\nu_\alpha \to \nu_\beta} = \left|\psi_{\alpha\beta}(t)\right|^2, \tag{1.33}$$

where $\psi_{\alpha\beta}(t) \equiv A_{\nu_\alpha \to \nu_\beta}(t) = \langle \nu_\beta | \nu_\alpha(t) \rangle$.

The Schrödinger equation for the transition amplitude yields

$$\begin{aligned} i\frac{\mathrm{d}}{\mathrm{d}t}\psi_{\alpha\beta}(t) &= i\frac{\mathrm{d}}{\mathrm{d}t}\langle \nu_\beta | \nu_\alpha(t) \rangle = \langle \nu_\beta | \left(H_0 + H_1\right) | \nu_\alpha(t) \rangle \\ &= \left(\langle \nu_\beta | H_0 + \langle \nu_\beta | V_\alpha \right) | \nu_\alpha(t) \rangle \\ &= \sum_\eta \left(\sum_k U_{\beta k} E_k U^*_{\eta k} + \delta_{\beta\eta} V_\beta \right) \psi_{\alpha\eta}(t). \end{aligned} \tag{1.34}$$

Again we substitute $E_k \simeq E + \frac{m_k^2}{2E}$ and $t \simeq L = x$. Equation 1.34 therefore becomes:

$$\begin{aligned} i\frac{\mathrm{d}}{\mathrm{d}x}\psi_{\alpha\beta}(x) = &\left(E + \frac{m_1^2}{2E} + V_{NC} \right) \psi_{\alpha\beta}(x) \\ &+ \sum_\eta \left(\sum_k U_{\beta k} \frac{\Delta m^2_{k1}}{2E} U^*_{\eta k} + \delta_{\beta\eta}\delta_{\beta e} V_{CC} \right) \psi_{\alpha\eta}(x). \end{aligned} \tag{1.35}$$

The first term in the equation, $\left(E + \frac{m_1^2}{2E} + V_{NC} \right) \psi_{\alpha\beta}(x)$, is equal for all possible transitions $\nu_\alpha \to \nu_\beta$, and can be removed by an appropriate phase transformation. Therefore, it does not contribute to the neutrino flavour transitions. Hence, only the charged current potential V_{CC} plays a role in the matter effects. The expression of the evolution equation for neutrino transformations in matter now is given by

$$i\frac{\mathrm{d}}{\mathrm{d}x}\psi_{\alpha\beta}(x) = \sum_\eta \left(\sum_k U_{\beta k} \frac{\Delta m^2_{k1}}{2E} U^*_{\eta k} + \delta_{\beta\eta}\delta_{\beta e} V_{CC} \right) \psi_{\alpha\eta}(x). \tag{1.36}$$

This formula can be expressed in matrix form as well:

$$i\frac{\mathrm{d}}{\mathrm{d}x}\Psi_\alpha = H_F \Psi_\alpha, \tag{1.37}$$

where H_F is the Hamiltonian in matrix form in the flavour basis:

$$H_F = \frac{1}{2E}\left(U\mathbb{M}^2U^\dagger + \mathbb{A}\right). \tag{1.38}$$

Considering mixing of three neutrino flavors, the relevant matrices are of the form

$$\Psi_\alpha = \begin{pmatrix}\psi_{\alpha e}\\ \psi_{\alpha\mu}\\ \psi_{\alpha\tau}\end{pmatrix}, \qquad \mathbb{M}^2 = \begin{bmatrix}0 & 0 & 0\\ 0 & \Delta m^2_{21} & 0\\ 0 & 0 & \Delta m^2_{31}\end{bmatrix}, \qquad \mathbb{A} = \begin{bmatrix}A & 0 & 0\\ 0 & 0 & 0\\ 0 & 0 & 0\end{bmatrix}, \tag{1.39}$$

where the matter potential A is given by $A = \pm 2\sqrt{2}G_F N_e E$, where E is the neutrino energy, and the plus (minus) sign corresponds to neutrinos (anti-neutrinos).

Neutrino mixing parameters

As discussed earlier in this chapter, in the standard framework of three neutrinos, there are three mixing angles and one CP-violating phase. Furthermore, the existence of three different mass eigenstates implies that there are two independent squared-mass differences. Because only the absolute values of the squared-mass differences are measured, and we do not yet know the exact value of the neutrino masses, there are two possible hierarchies for the neutrino masses. The case where $\nu_3 > \nu_2 > \nu_1$ is called *normal hierarchy* (NH) and the case where $\nu_2 > \nu_1 > \nu_3$ is called *inverted hierarchy* (IH). This is schematically illustrated in figure 1.1.

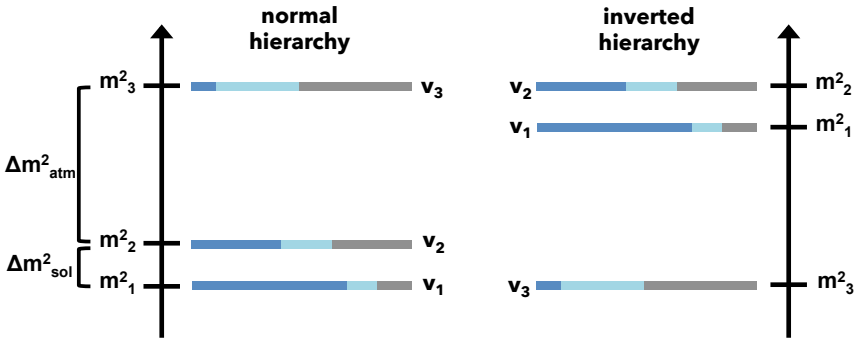

Figure 1.1: The neutrino mass hierarchy in the standard three-neutrino framework.

The mixing parameters have been measured over the years by several solar, atmospheric and reactor neutrino experiments [25]. The smallest of the two mass-squared differences, Δm^2_{21} has the best-fit value $7.37\times10^{-5}\text{eV}^2$, while the large one, Δm^2_{32}, has

a best-fit value of $2.54 \times 10^{-3}\text{eV}^2$, both as adapted by the particle data group, based on the latest global analyses of several experiments [25, 29, 30]. The three mixing angles, θ_{12}, θ_{23} and θ_{13}, are all measured by now as well. Adapting the values appearing in the latest PDG listing [25], the solar neutrino mixing angle θ_{12} has a best-fit value of $\sin^2\theta_{12} = 0.307$, the mixing angle θ_{23} has a best-fit value of $\sin^2\theta_{23} = 0.421$, and the mixing angle θ_{13} has a best-fit value of $\sin^2\theta_{13} = 0.021$. The best fit value for the CP-violating phase is $\delta_{cp} = 1.38\pi$ [30].

The values of the individual massive neutrinos are not yet known, but are subject to the efforts of many experiments. The relic neutrinos caused fluctuations in the CMB. Using cosmological data, an upper limit can be set on the sum of the mass of the three neutrinos. The most robust constraint [25] on this comes from Planck data, and gives $\Sigma m_\nu < 0.59$ eV at 95% CL [31]. The second method is through the detection of *neutrinoless double beta-decay*. In ordinary beta decay, two neutrons (protons) in an atomic nucleus both decay into a proton (neutron), submitting an electron (positron) and an anti-neutrino (neutrino). If the neutrino is a Majorana particle, and therefore its own antiparticle, double beta decay could theoretically take place in such a way that the neutrino going out at one vertex, is the same neutrino going in at the other vertex. In this case, no neutrinos would be emitted. The decay rate of the process depends on the neutrino mass. Experiments that are looking for this neutrinoless double beta-decay are EXO [32], KamLAND-Zen [33], GERDA [34] and MAJORANA [35]. The third method is the direct detection of the neutrino mass through the kinematics of weak decays, based on the conservation of energy and momentum, in tritium-beta decays. The most recent limit from this type of experiment is $m_{\nu_e} < 2$ eV, at 95% CL [25], based on the analysis of Ref [36] and [37].

Neutrinos are not only interesting for investigating their properties, they can also be used to explore astrophysical sources and (new) physics. We will discuss this in the next two sections.

2.3 Neutrino astrophysics

Neutrinos are produced in astrophysical sources as a product of nuclear reactions and decays. Although most of our knowledge on astrophysical objects and phenomena has been obtained through the observation of photons, neutrinos can teach us about regions from where photons cannot reach us. Photons from the sky reach us in abundant amounts and are easy to detect over a wide energy range. They can travel over long distances since they are stable and neutral, so they are not affected by

magnetic fields. However, hot dense regions in astrophysical energy sources, like the core of our sun or other stars, supernovae and active galactic nuclei, are opaque to photons, such that they cannot reach our detectors. Neutrinos on the other hand are stable and neutral as well, and because they are weakly interacting with matter, they are able to travel from these hot dense astrophysical sources towards the Earth. Unfortunately, this property also causes them to be very hard to detect.

Furthermore, photons with very high energies (in the order of $\gtrsim$ 10 TeV) can undergo interactions with photons in the Extragalactic Background Light (EBL) and the Cosmic Microwave Background (CMB), creating electron-positron pairs, which results in a suppression on gamma-rays with energies above $\sim$ 10 TeV coming from cosmological distances. Again, neutrinos are not limited by such effects.

The first detector that observed neutrinos beyond our solar system was actually built to search for proton decay, to verify the *Grand Unification Theories* (GUT). The Kamioka Nucleon Decay Experiment (KamiokaNDE), a 4.5 kton water Cherenkov detector, was finished in 1983, with an upgrade in 1985 that made it sensible to neutrinos as well [38]. In February 1987, KamiokaNDE still had not detected any decaying proton, when a supernova explosion occurred in the Magellanic cloud. KamiokaNDE observed 11 neutrino events in a timespan of only 13 seconds [39]. This event marked the beginning of neutrino astronomy. In 1995, the construction of the 50 kton water Cherenkov detector Super-Kamiokande (Super-Kamioka Neutrino Detection Experiment) was finished [40]. Super-Kamiokande started to take data in 1996 and was especially designed to study solar neutrinos and atmospheric neutrinos (or neutrinos from other astrophysical sources).
KamiokaNDE and Super-Kamionde were sensitive to neutrinos in the lower energy range ($\sim$ 3.5 MeV - 10 GeV). The detection of highly energetic cosmic ray protons with energies in the range of $10^8 - 10^{20}$ eV [41] indicated that highly energetic neutrinos should also exist. Since protons are charged and their trajectory therefore influenced by magnetic fields, we cannot locate their source. However, in the process of accelerating protons to such large energies, a lot of high energy gamma-rays and neutrinos should also have been produced.

The first detectors designed to look for such high-energy neutrinos were AMANDA (*Antarctic Muon And Neutrino Detector Array*, 1997 - now) on the south pole [42] and the ANTARES telescope (*Astronomy with a Neutrino Telescope and Abyss environmental RESearch*, finished in 2008) in the Mediterranean Sea [43]. Since 2005, AMANDA has been part of the IceCube neutrino observatory [44]. IceCube is a cubic kilometer covering ice Cherenkov detector embedded in the south pole's ice, reaching a depth of 2500 meters [45]. When a neutrino propagates through the ice, they might

interact with it, producing electrically charged particles that induce the emission of Cherenkov light. This light is observed by the over 5000 optical modules that lie embedded in the ice, tracking the direction and energy of the neutrinos. IceCube can measure neutrinos in the range of 50 GeV up to ~ 1 EeV [46]. By now, IceCube found 82 events of neutrinos reaching the detector with energies above 20 TeV in their analysis of 6 years of data [47, 48, 49]. The origin of the high-energy neutrino events is still an open question. Several extragalactic source candidates have been proposed, such as star-forming galaxies [50, 51, 52, 53, 54, 55, 56, 57, 58, 59], active galactic nuclei (AGN) [60, 61, 62], gamma-ray bursts (GRBs) [63, 64, 65, 66, 67] and blazars [68, 69, 70, 71]. Recently however, a high energy neutrino event with an energy of 290 TeV at IceCube coincided with the observation of a flaring blazar detected by multiple gamma-ray telescopes [72]. An analysis in the direction of this blazar of data prior to this event, also indicated an excess in this direction between September 2014 and March 2015 [73]. This indicates that blazars, as expected, indeed are one of the sources of high-energy neutrinos.

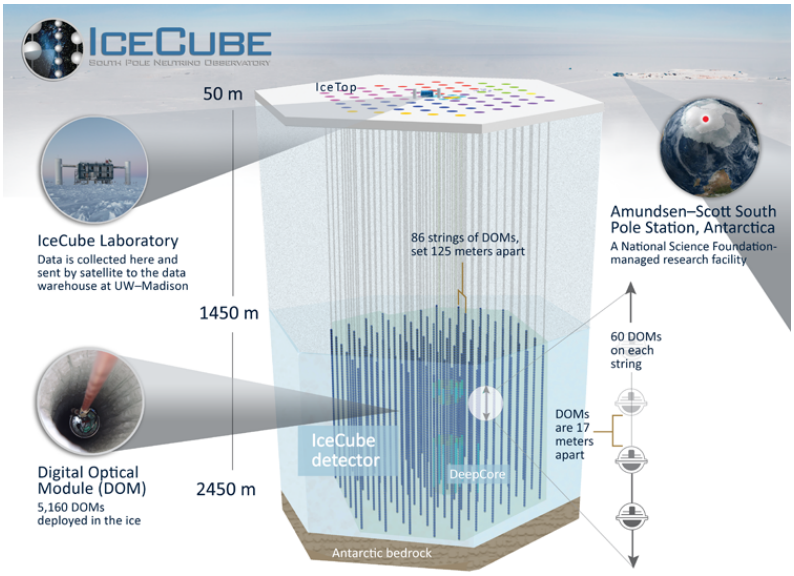

Figure 1.2: Schematic setup of the IceCube detector. The figure is taken from [74].

The successor of the ANTARES telescope, located at the northern hemisphere, is KM3NeT [75]. KM3NeT is located in the Mediterranean Sea and consists of 2 components: the ARCA (*Astroparticle Research with Cosmics in the Abyss*) neutrino tele-

scope 100 km off shore near Sicily in Italy, with the objective to study the sources, energy spectrum and flavor composition of cosmic high-energy neutrinos, and the ORCA (*Oscillation Research with Cosmics in the Abyss*) detector located south of France, with the purpose of studying neutrino properties using atmospheric neutrinos. Like IceCube, the telescope consists of a three-dimensional array of light sensor modules, but embedded in water rather than ice. The telescope consists of over 4000 bulbs, covering a cubic kilometer of sea water. Since the Cherenkov light scatters less in sea water than in ice, KM3NeT has a much better angular resolution than IceCube, resulting in a smaller uncertainty on the direction of origin. KM3NeT also covers a wider field of view, covering 87% of the sky, including most part of the galactic plane, including the galactic center. The telescope will be sensitive to cosmic neutrinos with energies in the range of $\sim$ tens of GeV to PeV. The start of operation of ARCA will be approximately in 2020 [76].

Besides the Cherenkov detectors described above, an other attempt to detect even higher energetic neutrinos, in the ultra-high-energy range, is made by ANITA (*Antarctic Impulsive Transient Antenna*) [77]. This is a balloon experiment, detecting radio pulses coming from ultra-high-energy neutrinos interacting with Antarctica's ice. ANITA is sensitive to neutrinos with energies in the EeV range. These ultra-high-energy neutrinos are thought to be produced in interactions of ultra-high-energy cosmic rays ($\sim 10^{20}$ eV) with the CMB photons. Although the experiment is sensitive to extremely high energies, ANITA is not able to distinguish the neutrino flavors.

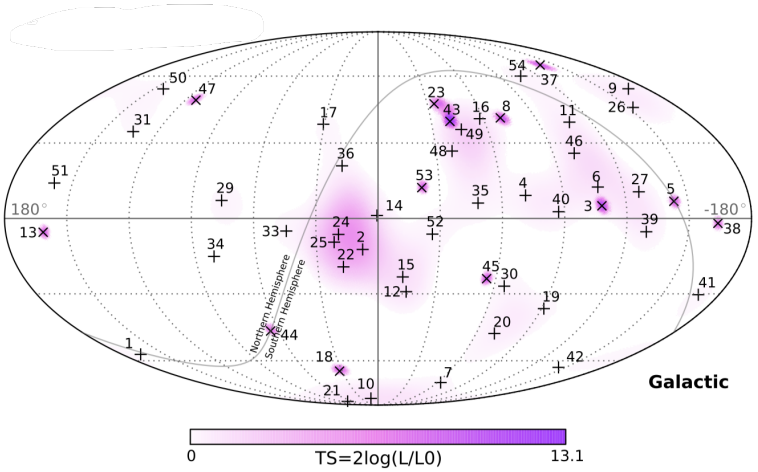

(a) The IceCube neutrino events and their arrival directions in galactic coordinates. Shower-like events are depicted with +, tracks events with ×. The coloring depicts the test statistics of the point-source clustering test. The figure is taken from Ref. [48]

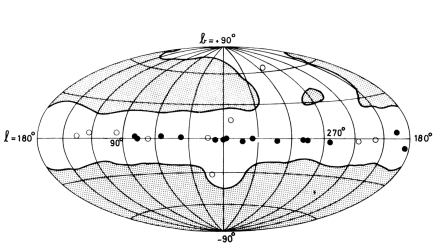

(b) The gamma-ray sky in 1980, detected by the COS-B satellite [78], containing 25 sources. The figure is taken from [79].

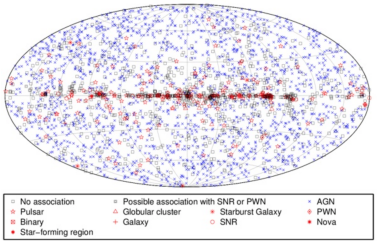

(c) The gamma-ray sky in 2015, detected by the Fermi-LAT satellite [80], containing 3033 sources. The figure is taken from [81].

Figure 1.3: The upper figure shows the current neutrino source catalog detected by IceCube. The lower figures show the gamma-ray source catalog in 1980 on the left, and 2015 on the right respectively. It is an astroparticle physicist's dream that neutrino astronomy will undergo the same incredible improvement as gamma-ray astronomy did over the last few decades.

2.4 Exploring new physics with neutrinos

As explained in chapter 2.2, neutrino oscillation behaves differently when neutrinos propagate through matter than when propagating through vacuum. In the same way,

other processes, that we do not yet know of, could influence the behaviour of the oscillation probability as well. This would affect the flavor composition at Earth. Therefore, investigating the flavor composition of astrophysical neutrinos at Earth could tell us something about possible new physics.
The Hamiltonian of the standard neutrino evolution is inversely proportional to the neutrino energy. This means that for higher neutrino energies, the effect of this standard component on flavor change becomes smaller. When the effective Hamiltonian induced by new physics does not depend on the neutrino energy, or is even proportionally related to it, these effects will grow for higher neutrino energies. New physics effects that would be unobservable for lower energies, could become dominant at higher energies, and result in a visible effect on the flavor composition at Earth. Furthermore, since astrophysical neutrinos propagate over such large distances, small effects induced by physics beyond the SM get the chance to accumulate into a larger, observable effect. A Hamiltonian for oscillations induced by new physics would be of the shape

$$H = \frac{1}{2E} U \mathbb{M}^2 U^\dagger + V_{\text{new physics}}. \tag{1.40}$$

To know the expected final flavor ratio at Earth, we need to know the flavor ratio at the source. In astrophysical sources, high energy neutrinos are mainly produced in pion decay [5]:

$$\pi^+ \rightarrow \mu^+ + \nu_\mu \tag{1.41}$$

$$\mu^+ \rightarrow e^+ + \nu_\mu + \bar{\nu}_e, \tag{1.42}$$

which results in a flavor ratio of $1:2:0$ for electron-, muon- and tau neutrinos. The other possible production channels are muon-damped pion decay, which could happen due to energy losses affecting the muon in strong magnetic fields [82, 83],

$$\pi^+ \rightarrow \cancel{\mu^+} + \nu_\mu, \tag{1.43}$$

resulting in a ratio of $0:1:0$, and neutron decay [84]:

$$n \rightarrow p + e^- + \bar{\nu}_e, \tag{1.44}$$

resulting in a ratio of $1:0:0$. There are no known astrophysical processes that produce tau neutrinos. Starting from a flavor ratio of $1:2:0$ at the source, oscillation over long astrophysical distances will result in an expected final flavor ratio of $1:1:1$ on Earth. If deviations from this expected ratio are measured, this would be an indication for new physics and could have several origins, such as new interactions

and the violation of Lorentz invariance. Signs of effects from the latter have been searched for in IceCube data [85]. The effect of new physics on the final flavor ratio is explored by Ref. [86], and Ref [87] gives a review on the effects of several new physics theories at the source, during propagation, and during detection of the neutrino. The impact of new physics on the neutrino flavor ratio was also part of the work performed for this thesis. In chapter 4 we explore how a coupling between neutrinos and scalar-dark energy, which induces an extra term in the oscillation Hamiltonian, would affect the flavor ratio on Earth.

The latest best fit for the final flavor ratio at Earth measured by IceCube is shown in Fig. 1.4 [48]. While still compatible with the expected ratio of $1:1:1$, the best fit value currently actually deviates from the expectation.

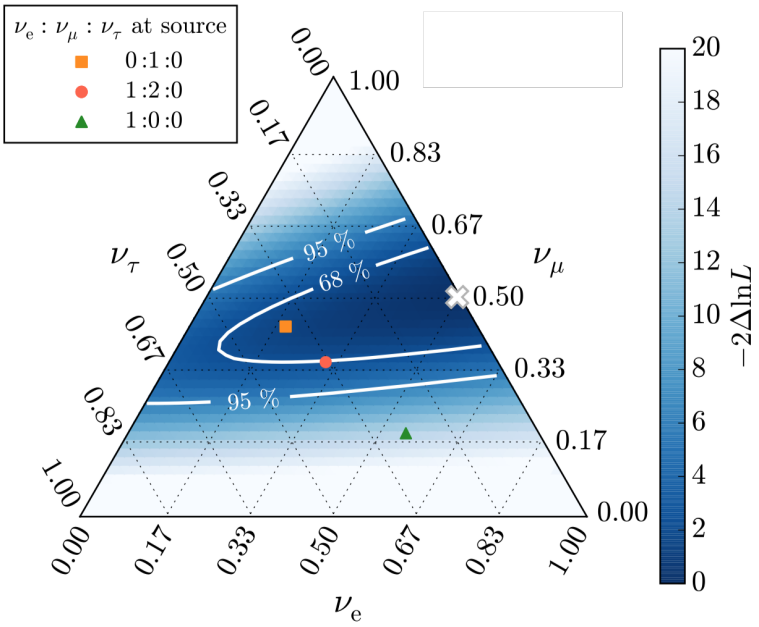

Figure 1.4: The latest best fit of the final flavor ratio of astrophysical neutrinos at Earth, detected by IceCube. The orange, green and red marks mark the expected flavor ratio for different starting ratios at the source. The best fit is marked with a white cross. The figure is taken from Ref. [48].

3 Dark Matter

3.1 A brief history

Everything that can be seen around us, with the naked eye or through microscopes and telescopes, is build up from matter. This ordinary matter however, makes up for only 18% of the total matter in the Universe [88]. The remaining part is thought to consist of so-called *dark matter* (DM). We cannot see this DM directly, because it only interacts very weakly with the ordinary matter in our Universe. The evidence for DM so far has only been gravitational of nature. The first hint for missing matter comes from Fritz Zwicky's work on the Coma cluster [89, 90], a group of thousands of galaxies. He investigated the variation of the velocity among the galaxies in the cluster, the velocity dispersion, which is a measure for the total mass of the cluster. He found that the velocity dispersion was much higher than one would expect, based on the observed amount of matter in the cluster. His conclusion was that the cluster had to contain much more 'dark' than 'light' - ordinary - matter, to compensate for the missing mass. With this, he introduced the term that we nowadays still use to describe this unsolved problem of the missing mass in the Universe. However, Zwicky himself used the term to refer to matter that was unseen to us, in the form of cool and cold stars and gases, rather than a new type of matter than we knew before. At that time, the SM of particle physics was not even yet established.

Besides the mass discrepancy in galaxy clusters, the second hint for missing mass came from research on galactic rotation curves. These are measurements on the circular velocity of the individual stars in the galaxy, as a function of the distance to her center. Because of Newton's laws of gravity, we expect the velocity of the stars in the outer regions of the galaxy to fall as a function of radius, $v(r) \propto 1/\sqrt{r}$. Instead, the work that Vera Rubin and Kent Ford performed in the seventies of the previous century using optical spectroscopy, showed that the curve remained flat in the outer regions [91, 92, 93]. Their conclusion was that non-luminous matter should exist beyond the optical galaxy. Similar results were found in radio observations of rotation curves [94, 95, 96, 97, 98, 99, 100].

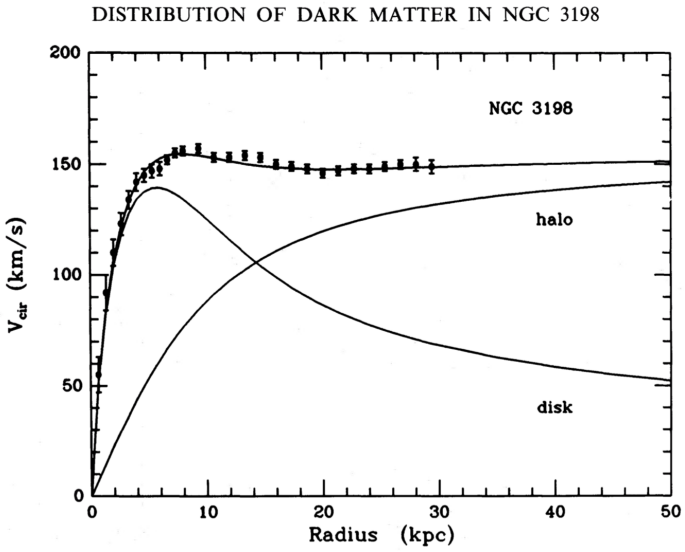

Figure 1.5: The observed rotation curve of the galaxy NGC 3198, together with the curve based on the visible disk, and the predicted curve from the DM halo that could correct for the missing mass. The figure is taken from Ref. [101].

Simultaneously, the field of cosmology was in need for some extra matter as well. In their study to determine the curvature and composition of the Universe, they preferred a closed Universe, with $\Omega = \rho/\rho_c \geq 1$, such that gravity was able to overcome the expansion induced by the Big Bang. For the Universe to be closed, the mass density should be equal or larger than the critical density $\rho_c \simeq 10^{-5} h^2\,\mathrm{GeV\,cm^{-3}}$, where h is the Hubble constant in units of 100 km $\mathrm{s^{-1}}$ $\mathrm{Mpc^{-1}}$. Cosmologists noted that this could be established when the visible mass of galaxies was actually only accounting for 10% of the total mass [102], an idea already supported by the observations discussed above. This boosted the interest in the origin of the mass anomalies in galaxies and galaxy clusters, and the nature of dark matter. For a more detailed discussion on the history of how DM came to an interest, see Ref. [103].

The *cosmic microwave background* (CMB) can tell us about the composition and shape of the Universe. The CMB is the relic radiation remnant from the epoch of recombination. After inflation, when the Universe was expanding and getting cooler, the protons and electrons in the plasma combined into neutral hydrogen atoms, transforming the Universe from opaque into transparent for radiation. The photons that were since then free to travel, rather than scattering on free electrons and protons in the plasma, are now still arriving at us, and being observed as the CMB. The size

of the density perturbations in the CMB tell us something about the shape of the Universe, and observations indicate a nearly flat Universe at the time, with $\Omega \sim 1$. Observations on the power spectrum of the temperature fluctuations of the CMB can tell us more on the energy density of baryonic and non-baryonic matter. These observations are done by the Wilkinson Microwave Anisotropy Probe (WMAP) [104] and later on the Planck Observatory [105], which found the following values for the dark matter density and the baryonic matter density respectively [106]:

$$\Omega_{\mathrm{CDM}} h^2 = 0.1186(20) \tag{1.45}$$

$$\Omega_{\mathrm{b}} h^2 = 0.02226(23). \tag{1.46}$$

3.2 The nature of Dark Matter

Now that we have discussed the several evidence for extra mass in the Universe, the question arises what the nature of this mass could be. The obvious answer would be that this mass comes from normal baryonic matter, that is just too dim for us to observe, such as planets, dwarf stars, neutron stars and black holes. These objects have been named Massive Compact Halo Objects (MACHOs). These objects could be gravitationally observed through microlensing effects. The searches for such events, however, did not result in enough events to be able to explain all the DM mass [107, 108, 109]. The number of events they found suggested that MACHOs could explain not more than 8% of the halo mass in our galaxy [109]. Recently, the first detection of gravitational waves by the LIGO collaboration in 2015 [110], re-introduced the idea that DM could consist of (solely) primordial black holes. The gravitational waves came from the merger of 2 black holes with masses of $\sim 30 M_{\odot}$, leading to the suggestion that these black holes were primordial black holes [111, 112]. This idea has been studied before [113, 114, 115, 116, 117, 118], resulting in several constraints on the properties of primordial black holes over a wide mass range [119]. However, in this light, Ref. [120] compared the predicted radio and X-ray emission from accretion of interstellar gas onto primordial black holes in our Milky Way (MW) with observational data, in case they constitute all of the DM. They show that this scenario is excluded at 5σ and 40σ using radio and X-ray observations respectively.

Another attempt to explain DM with standard model particles, was the neutrino, since they are electrically neutral, long living, extremely difficult to detect and turned out to have masses. However, in the early eighties of the last century, N-body simulations have shown that if neutrinos constitute all the DM, the large scale structure of the Universe would look different than we know from observations [121]. The structures formed through the clustering of relativistic, *hot* dark matter, like neutrinos, would

be too large. From these observations, we know that dark matter should be *cold*, i.e. non-relativistic. Since no other SM particle could explain DM either, the solution was looked for beyond the SM.

Another indication for non-baryonic DM, is the *Bullet Cluster* [122], which is pictured in Fig. 1.6. It shows two colliding galaxy clusters, observable in the optical spectrum. Because the galaxy clusters do mainly consist of space between the galaxies, rather than galaxies itself, the chance of the individual galaxies of the two clusters hitting each other when passing through is small. The pink regions constitute the baryonic gas of the two galaxies, that clumped together when the two galaxies collided, heated up, and started to emit X-rays, which is now used to observe them. In blue, the mass distribution of the galaxies is depicted, using weak gravitational lensing. As can be seen, the blue regions coincide with the distribution of the galaxies, rather than with the pink interacting gas. This implies that DM should be non-baryonic, otherwise it would have interacted with each other, like the baryonic gas did.

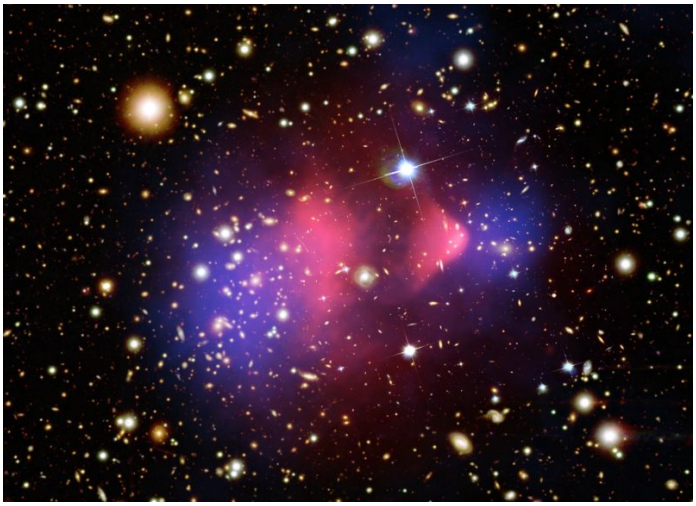

Figure 1.6: The bullet cluster as an indication of non-baryonic dark matter. X-ray is visualised in pink, the blue is the mass distribution visualised through gravitational lensing. The figure is taken from Ref. [123].

To qualify as a DM candidate, several conditions need to be fulfilled. The particle must be stable on cosmological time scales, they must interact only very weakly with electromagnetic radiation and they must have the right relic density implied by cosmology [25].

Axions are exotic particles originally proposed to solve the strong-CP problem [124, 125, 126, 127], but additionally turned out to be an excellent DM candidate [128, 129]. Although the first proposed axion model has been ruled out [130], several other models for axion and axion-like particle are still being considered as DM candidates [131], and several experiments are trying to detect them [132, 133, 134, 135, 136].

As discussed above, SM neutrinos are too light and their interaction with other particles is actually not weak enough to constitute all the DM. The *sterile neutrino* is a hypothetical neutrino type that does not take part in weak interactions, in contrast to the *active* SM neutrinos. The SM neutrinos are all left-handed, while all the other SM particles can be both right- and left-handed. The sterile neutrinos are proposed as the right-handed neutrinos, and could therefore also be part of the solution to the problem of how neutrinos got their masses. Because they are sterile, they undergo almost no interactions with ordinary matter. Sterile neutrinos with masses in the keV range are considered as possible DM candidates. For a review on sterile neutrinos as DM, see Ref. [137].

The most popular DM candidates are the *weakly interacting massive particles* (WIMPs). Like axions, they emanate from a possible solution to another problem, namely the *hierarchy problem* and the *unification of the gauge couplings*. The hierarchy problem describes the issue of the electroweak scale being so much lower than the Planck scale, and therefore the mass of the Higgs boson being so much smaller than the Planck mass [138]. The Grand Unification Theory (GUT) describes the model desired by theoretical physicists where at high energies, the weak, electromagnetic and strong forces unify into one force, and the three gauge couplings all have the same value [139]. This would imply that at some time during the early Universe, the fundamental forces were unified in one force. However, in the SM these forces fail to unify.
Supersymmetry (SUSY) is the SM extension that could solve both these problems [140]. SUSY introduces a supersymmetric partner for every particle in the SM. Bosons get a fermion-partner, and fermions get a boson-partner. One of the supersymmetric particles that arises this way, is the neutralino [141], a Majorana fermion, which is a weakly interacting massive particle. WIMPs have masses in the order of ~ 1 GeV $- 1$ TeV. After inflation, WIMPs were in thermal and chemical equilibrium with the hot dense SM soup. When the Universe cooled, and the temperature dropped below the WIMP mass, the SM particle to WIMP production rate lowered and the WIMP number density became exponentially suppressed. When the reaction rate of WIMPs annihilating into SM particles became smaller than the Hubble expansion rate, the WIMPs fell out of thermal equilibrium with the SM plasma, and the comoving number density of WIMPs (i.e. number of WIMPs per expanding volume)

became constant. This is called the *freeze out* of WIMPs [142]. This freeze out determined the amount of DM in the present Universe. The DM relic density can be approximated by [143], regardless of the DM model:

$$\Omega_\chi h^2 = \frac{m_\chi n_\chi}{\rho_c} \simeq \frac{3 \times 10^{-27} \mathrm{cm}^3 \mathrm{s}^{-1}}{\langle \sigma v \rangle}, \tag{1.47}$$

where m_χ is the DM mass, n_χ is the DM number density, ρ_c is the critical density, which is $\rho_c \simeq 10^{-5} h^2 \,\mathrm{GeV\,cm}^{-3}$, and $\langle \sigma v \rangle$ is the DM annihilation cross section multiplied by the relative velocity of the annihilating particles, averaged over their velocity distribution. Since the relic density is inversely proportional to the DM annihilation cross section, a larger cross section keeps the DM particles in equilibrium with the SM plasma for a longer amount of time, resulting in a lower relic density. Considering a dark matter density of $\Omega_{\mathrm{CDM}} h^2 \approx 0.1186$ [106], we approximately find the canonical cross section for DM annihilation which is given by $\langle \sigma v \rangle \approx 3 \times 10^{-26} \mathrm{cm}^3 \mathrm{s}^{-1}$. A more precise determination of the relic density is performed by Ref. [144], resulting in an estimate of the annihilation cross section that, for DM masses below 10 GeV, depends on the mass, with a maximum of $\langle \sigma v \rangle \approx 5.2 \times 10^{-26} \mathrm{cm}^3 \mathrm{s}^{-1}$ at $m \approx 0.3$ GeV, and has the value $\langle \sigma v \rangle \approx 2.2 \times 10^{-26} \mathrm{cm}^3 \mathrm{s}^{-1}$ for DM masses above 10 GeV. The order of magnitude of the cross section that follows naturally from the relic density implies weak scaled interactions [144]. A strong or electromagnetic interacting particle would not result in the right relic abundance, which can be seen visualised in Fig. 1.7. The relic density implies a weakly interacting particle, naturally suggesting the WIMP. This is what one refers to as the *WIMP miracle*. WIMPs, which fulfil the requirements for particle DM, are naturally arising from super symmetry models and naturally predict the right relic abundance for DM. Well motivated as WIMPs are, they play the lead role as the DM candidate in this thesis as well.

Another popular explanation for the missing mass in the Universe, is that there is no need for extra mass at all. Scientists in favour of this idea think that we do not understand the theory of gravity well enough at these scales, and that some modification to the theory is necessary to explain the anomalous measurements on rotation curves and galaxy clusters. The idea of *modified newtonian dynamics* (MOND) was proposed for the first time in 1983 by Mordehai Milgrom [145]. Up to today, it has been a popular alternative to the theory of dark matter. For a review on MOND, see e.g. Ref. [146]. Another theory of modified gravity that is proposed as an alternative to DM, is Erik Verlinde's theory of emergent gravity [147]. In his theory, the displacement of dark energy by baryonic matter causes a modification of the gravitational laws on galactic scales, from which dark matter emerges naturally as an additional gravitational force. However, at this moment, the emergent gravity theory is only applicable on (approx-

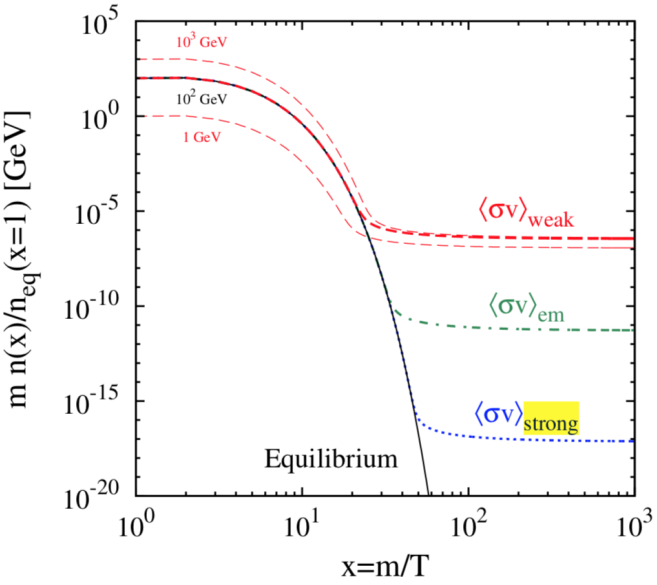

Figure 1.7: The cosmological WIMP abundance as a function of $x = m/T$. The thick curves show the WIMP mass density, normalized to the initial equilibrium number density, for several choices of the annihilation cross section $\langle\sigma v\rangle$ and mass m. Results for $m = 100$ GeV, are shown for weak interactions, $\langle\sigma v\rangle = 2 \times 10^{-26}\text{cm}^3\text{s}^{-1}$, (dashed red), electromagnetic interactions, $\langle\sigma v\rangle = 2 \times 10^{-21}\text{cm}^3\text{s}^{-1}$ (dot-dashed green), and strong interactions, $\langle\sigma v\rangle = 2 \times 10^{-15}\text{cm}^3\text{s}^{-1}$ (dotted blue). For the weak cross section the thin dashed curves show the WIMP mass dependence for $m = 103$ GeV (upper dashed curve) and $m = 1$ GeV (lower dashed curve). The solid black curve shows the evolution of the equilibrium abundance for $m = 100$ GeV. A larger cross section implies a smaller relic abundance. The figure and description are taken from Ref. [144].

imately) spherically symmetric and isolated astronomical systems in non-dynamical situations. Therefore it can only explain DM in limited situations and does not yet provide a solution for most of the arguments for DM.

In 2018, results of a study on the radial velocities of multiple luminous globular-cluster-like objects in the galaxy NGC1052-DF2 suggested that this galaxy does not contain any dark matter [148]. The radial velocities predict a mass that is consistent with the baryonic component of the galaxy. This atypical result has consequences for the theory of DM, since it implies that dark matter does not always have to coincide with galaxies. However, it is certainly an argument against modified gravity theories such as MOND and emergent gravity, since their modification should apply for all

galaxies.

3.3 Methods of detection

There are three methods to detect DM. The first is called *direct detection*, in which we look for scattering interactions of DM particles on SM particles. To look for these interactions, large detectors are build on highly shielded locations, such as the XENON1T experiment in the mountain of Gran Sasso [149], such that only WIMPs (and neutrinos) could pass through. With these detectors, one looks for interactions of WIMPs scattering on the detector's material when they pass by.

The second method is *indirect detection*. WIMPs are assumed to be Majorana particles, which implies that they are their own anti-particles. If one DM particle meets another one, they could annihilate. As their annihilation products, neutrinos and gamma-rays are produced. In indirect detection we look for these annihilation products coming from astrophysical sources with a large DM density. Similarly, one could also look for the SM products of DM decay.

The third method is to try to produce them ourselves from SM particles in collider experiments like the Large Hadron Collider (LHC) [150].

The detection channel that is important for this thesis, is indirect detection, which will be more elaborated on in section 3.5 of this chapter.

3.4 The dark matter density distribution

In order to be able to detect dark matter, it is necessary to know how it is distributed. Structure formation is initially driven by perturbations of the DM density, generated due to inflation, growing bigger over time. DM clumped together to form small clumps, which merged under gravity into larger clumps, resulting in a large web of matter. On galactic scales, DM is distributed into halos and subhalos surrounding clusters and galaxies. One of the first models that has been considered to describe the DM distribution in the halo, was the *Navarro, Frenk, and White* (NFW) profile [151, 152]. This profile came forth from N-body simulations of structure formation driven by CDM, and is a universal profile, describing all halos from the size of small dwarf galaxies to large galaxy clusters. The formula that describes the NFW profile is given by

$$\rho(r) = \frac{\rho_s}{\left(\frac{r}{r_s}\right)^{\gamma}\left(1+\frac{r}{r_s}\right)^{3-\gamma}}, \tag{1.48}$$

where r_s is the scale radius and ρ_s the characteristic density, the density at r_s. The parameter γ can be changed to vary the inner slope of the profile, where $\gamma = 1$ yields the original NFW profile. This profile is a *cusped* profile, which entails that the inner slope is very steep. In the case of the NFW profile, $\rho(r) \to \infty$ for $r \to 0$, so the density is not defined at the center.

Later simulations indicated a density profile with a slightly shallower inner slope [153], while the outer regions were still similar to the NFW profile. The profile that suited these simulations well, was the Einasto profile [154, 155, 156], earlier proposed to describe the density of spherical stellar systems. The Einasto profile is described by

$$\rho(r) = \rho_s \exp\left(-\frac{2}{\alpha}\left[\left(\frac{r}{r_s}\right)^{\alpha} - 1\right]\right). \tag{1.49}$$

The Einasto profile does not diverge at the center, but is nonetheless a cusped profile.

The best known density profile describing a *cored* central density, is the Burkert profile [157]. This profile was proposed when observations of the rotation curves of dwarf galaxies indicated that their density profile was not compatible with a NFW profile [158, 157], but instead needed to be much flatter at the center. The Burkert profile is described by

$$\rho(r) = \frac{\rho_s r_s^3}{(r_s + r)(r_s^2 + r^2)}. \tag{1.50}$$

In the case of subhalos, the halos are bounded at the tidal radius, r_t, which is the radius where the external gravitational attraction, i.e. the attraction of the host halo, becomes larger than the gravitational attraction of the system itself.
Figure 1.8 shows the DM density for the several density profiles as a function of radius from the center.

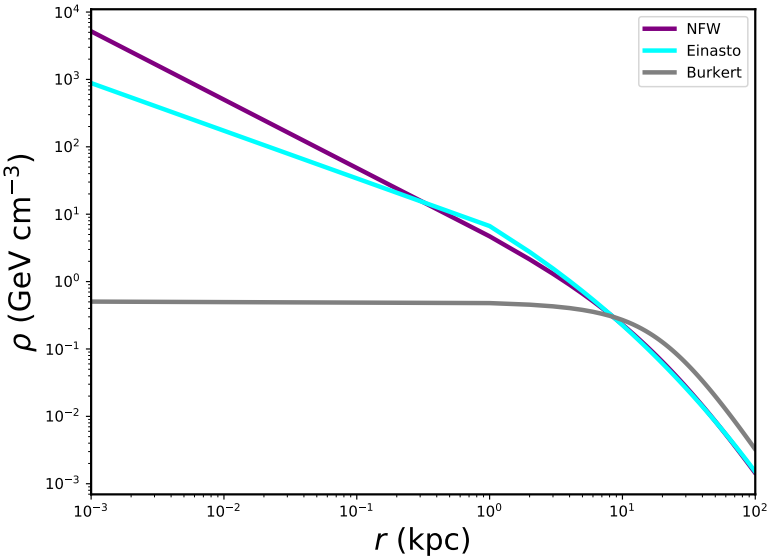

Figure 1.8: The NFW, Einasto and Burkert density profiles as a function of distance from the center of the halo. We take $\rho_s = 0.3$ GeV cm^{-3}, $r_s = 20$ kpc and the profiles are normalised such that the local density at $r = 8.5$ kpc equals $\rho = 0.3$ GeV cm^{-3}.

The NFW profile is the most widely adapted profile for DM analyses. Although it is a good fit for all DM halos in general, it might not always be the best fit to describe individual galaxy halos. As mentioned above, profiles predicted by ΛCDM-dominated N-body simulations, like the NFW profile, are strongly cusped [151, 152, 159, 160, 161], while observations of dwarf spheroidal galaxies and low surface brightness galaxies suggest a shallower cusped or even cored density profile [158, 157, 162, 163, 164]. Furthermore, the halos might not always have a spherical shape. Subhalos, like the halos of satellite galaxies, are affected in their shape by the tidal effects of their host galaxy [165]. Recent N-body simulations have predicted that these subhalos are not spherical, but are rather oblate, i.e. flattened at the poles, and axisymmetric of shape [165, 166, 167]. Observations of the Milky Way's dwarf spheroidal galaxies (dSphs) and the Andromeda galaxy have shown that their light distributions are not spherical as well [168, 169]. Therefore, the DM halos of these systems might be more accurately described by non-spherical axisymmetric mass models as well. Such models were constructed by Ref. [170, 171]. They assume axisymmetry in both the stellar and dark halo mass models for several dwarf spheroidal galaxies, derived the corresponding axisymmetric Jeans equations, and applied them to the line-of-sight velocity dispersion profiles of the dSphs. Since these models are fitted to the individual dSphs,

they are a better approximation of the dark halo than the universal NFW profile. In chapter 2, we analyse about seven years of data from the Fermi-LAT telescope [172] for seven classical dwarf galaxies, adopting both the widely used NFW profile and the observationally-motivated axisymmetric density profiles provided by Ref. [171], and determine upper limits on the DM annihilation cross section.

3.5 Indirect detection

In this thesis, we explore DM properties through indirect detection of DM annihilating into gamma-rays (chapter 2) and neutrinos (chapter 3). The flux of the SM particle of interest coming from DM annihilation, as a function of the direction ψ relative to the center of the area of interest, is often written in terms of the astrophysical contribution and the particle contribution:

$$\phi_{\rm WIMP}(E,\psi) = J(\psi) \times \mathbf{\Phi}^{\rm PP}(E), \tag{1.51}$$

where the astrophysical contribution $J(\psi)$ is called the *J-factor*. This term describes the DM distribution in our region of interest, as a function of the direction ψ relative to the center of the area of interest. It is defined by the line-of-sight integral of the DM density squared, since two DM particles are involved in the annihilation:

$$J(\psi) = \int_{\rm l.o.s} {\rm d}l(\psi)\rho^2(l(\psi)), \tag{1.52}$$

where l is the line-of-sight parameter and $\rho(l,\psi)$ is the DM density distribution as discussed in the previous section. Integrated along the line of sight, the J-factor describes the projection of the three-dimensional DM distribution on the two-dimensional sky. The particle physics factor is described by

$$\mathbf{\Phi}^{\rm PP}(E) = \frac{1}{2}\frac{\langle\sigma v\rangle}{4\pi\, m^2_{\rm WIMP}} \sum_f \frac{{\rm d}N_f}{{\rm d}E} B_f, \tag{1.53}$$

where $\langle\sigma v\rangle$ is the DM annihilation cross section multiplied by the relative velocity of the annihilating particles, averaged over their velocity distribution, $m^2_{\rm WIMP}$ is the mass of the DM particle, ${\rm d}N_f/{\rm d}E$ is the average number of SM target particles (gamma-rays or neutrinos) produced in one annihilation with corresponding branching ratio B_f and, in the case of Majorana DM, the factor $1/2$ accounts for the need of two DM particles to annihilate. Dark matter particles could annihilate into gamma-rays and neutrinos through a cascade of other (unstable) SM particles, but also directly. The latter results in a monochromatic signal which would be, when detected, the smoking gun for DM detection.

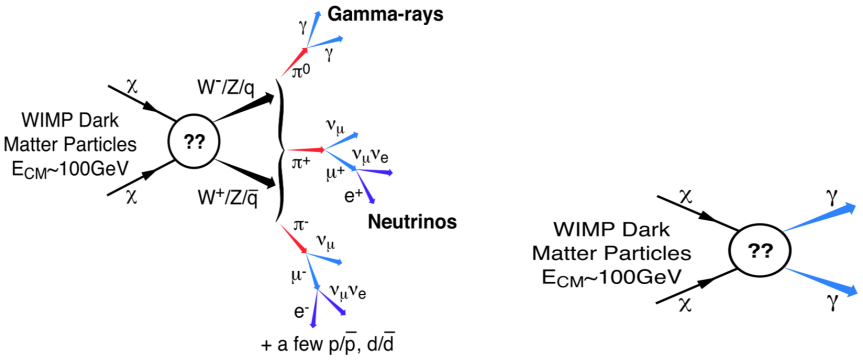

Figure 1.9: Schematic overview of the DM annihilation channels eventually resulting in gamma-rays and neutrinos. The figure is taken from Ref. [173].

The *Fermi Large Area Telescope* (Fermi-LAT) gamma-ray telescope is a space-based detector that scans the gamma-ray sky in the range of $\sim$ 20 MeV - 300 GeV[172]. It was launched in 2008, and their objectives include the search and study of astrophysical gamma-ray sources, the understanding of gamma-ray bursts and the search for new physics and dark matter. In the detector, the incoming gamma-rays first pass by a so called anticoincidence detector, distinguishing the gamma rays from cosmic rays. The latter would produce a light flash while gamma-rays pass through it unaffected. In the second part of the detector, the gamma-ray interacts with an atom in the detection material, producing an electron and a positron. The electron and positron create ions in the third part of the detector, consisting of several strips, tracking the progress of the electron and positron. In the fourth and final part of the detector, the electron and positron are stopped and the total energy that was deposited is measured. These four steps are combined to determine the energy and the direction of the gamma-ray. A schematic picture of the telescope and the detector is shown in Fig. 1.10.

Besides the space-based Fermi-LAT, there are also several ground-based gamma-ray detectors. The HAWC (*High-Altitude Water Cherenkov*) gamma-ray observatory consists of an array of water Cherenkov detectors, tanks filled of water, detecting the air showers induced by gamma-rays entering the atmosphere [174]. It is sensitive to gamma-rays in the energy range of 100 GeV - 100 TeV.
The charged particles in the air showers induced by the gamma-rays produce Cherenkov light directly in the atmosphere as well. This can be detected by atmospheric Cherenkov telescopes. These consist of mirrors facing to the atmosphere, focussing the Cherenkov

light on UV-sensitive photomultipliers. MAGIC (*Major Atmospheric Gamma Imaging Cherenkov*, sensitive to 30 GeV - 100 TeV) [175], VERITAS (*Very Energetic Radiation Imaging Telescope Array System*, sensitive to 50 GeV - 50 TeV) [176], HESS (*High Energy Stereoscopic System*, sensitive to tens of GeV up to tens of TeV) [177] and CTA (*Cherenkov Telescope Array*, sensitive up to 300 TeV) [178] use this technique to detect gamma-rays.

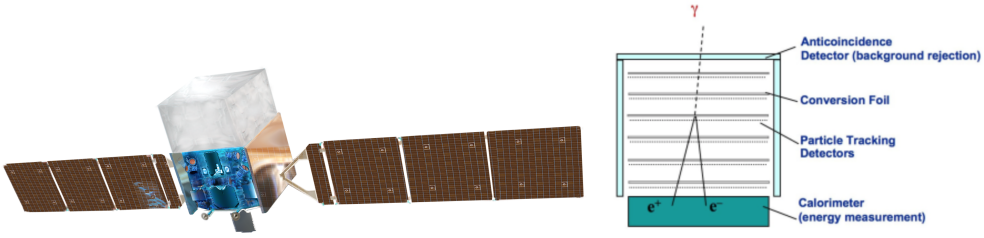

(a) (b)

Figure 1.10: The left figure shows an impression of the Fermi-LAT gamma-ray telescope. On the right, a schematic picture of the detector is shown. *Credit: NASA E/PO, Sonoma State University, Aurore Simonnet (left) and NASA/Fermi (right).*

The best regions to look for DM annihilation, are the regions where the DM density is the highest. The two main targets for this detection method are therefore the center of our Milky Way, and dwarf spheroidal galaxies.

The center of our galaxy has the highest concentration of DM nearby, but also has a complicated large background from other astrophysical sources. In 2009, the Fermi collaboration found a gamma-ray excess in the order of a few GeV in the direction of the galactic center [179]. Several studies show that this excess is compatible with DM annihilation [180, 181, 182, 183, 184, 185, 186, 187, 188, 189, 190, 191, 192]. However, like mentioned above, the galactic center region is home to a great amount of other gamma-ray sources, which are difficult to distinguish from a DM signal [193]. Currently, the most likely explanation considered for the excess besides DM annihilation, are millisecond pulsars [185, 194, 195, 196, 197].

Dwarf spheroidal galaxies are low-luminosity satellite galaxies of the Milky Way and Andromeda [198]. They are the largest substructures predicted by ΛCDM. Their mass-to-light ratio is extremely large, in the order of 100-1000, which implies that they should be largely dominated by DM. They show no recent star formation and the absence of interstellar gas and dust results in a very low gamma-ray background from other astrophysical sources [199]. This makes them attractive sources to look

for a DM annihilation signal. A few tens of dwarf galaxies has been analysed in the search for DM annihilation [200, 201, 202, 203, 204, 205]. In all but one cases, no signal of DM annihilation has been detected, and upper limits on the annihilation cross section have been set. In one dwarf galaxy, Reticulum II, a gamma-ray excess has been detected [206, 204, 205], compatible with the galactic center GeV excess. As discussed in the previous section, in chapter 2 we discuss our analysis of seven classical dwarf spheroidal galaxies.

Similar indirect detection studies can be performed with the high energy neutrino telescopes IceCube [45] and KM3NeT [75]. Compared to gamma-rays, neutrinos are much harder to detect. Because the number of neutrino events detected by those telescopes is much smaller than the number of gamma-rays we can detect, the limit on the dark matter annihilation cross section set with neutrino experiments will be much weaker. However, if a gamma-ray excess is found, claimed to be coming from dark matter, neutrinos can help us to confirm or reject this explanation. It is therefore very important to search for dark matter annihilations through neutrinos complementary to gamma-rays. Furthermore, dark matter particles could be gravitationally captured in dense astrophysical objects, like the sun. When these captured DM particles self-annihilate, only the neutrinos produced in this process can escape the sun - of which the core is opaque to photons- and detected at Earth. In chapter 3, we perform an indirect detection analysis on light DM using neutrino experiments.

3.6 The EDGES 21-cm result

The *Experiment to Detect the Global Epoch of Reionization Signature* (EDGES) is a ground-based radio telescope looking for hydrogen signatures from the *Epoch of Reionization* [207]. In the history of the Universe, this is the period right after the first star and galaxy formations. The ultraviolet light of these early stars hit the primordial hydrogen gas, causing an emission at the 21-cm line. Due to the absorption from CMB photons by the primordial gas, this resulted in a spectral signal in the cosmic microwave background (CMB) [208]. EDGES looks for these spectral imprints at $z \sim 17$. They recently published their results [209], in which they claim a signal in the absorption profile of the sky-averaged radio spectrum, centred at a frequency of 78 MHz, with an amplitude of 0.5 K. However, the amplitude of this signal is over a factor of two times as big as the largest predictions [210], with a certainty of 3.8σ. The discrepancy in the results imply that either the primordial gas during this era was much colder than expected, or that the temperature of the background radiation was much hotter. It has been argued that astrophysical phenomena are unlikely

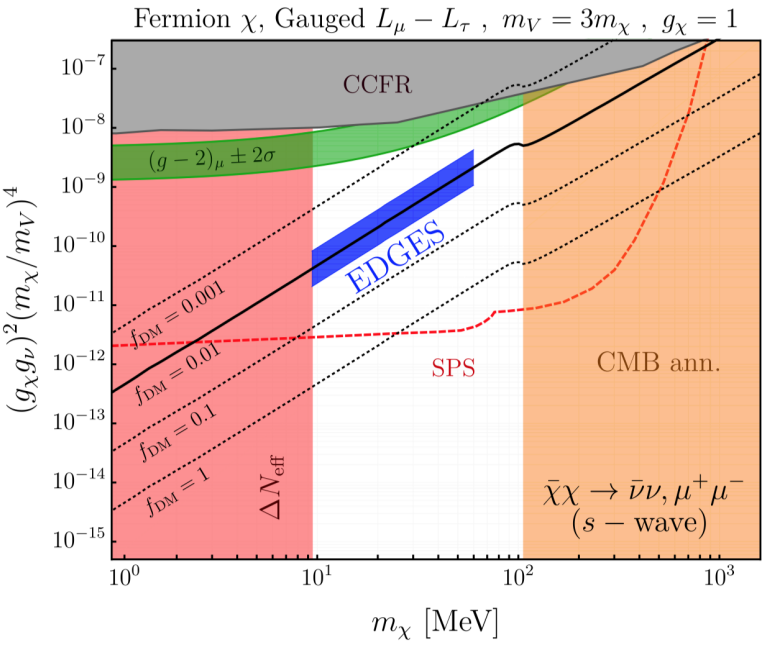

Figure 1.11: The current limits on the milli-charged DM specifications, generated by [216]. The vertical axis is the cross section in terms of the coupling constants, the mass of the DM particle, and the mass of the new mediator, where the cross section is specified as $\langle \sigma v \rangle = \frac{g_\nu^2 g_\chi^2 m_\chi^2 \kappa}{2\pi(4m_\chi^2 - m_V^2)^2}$.

to be responsible for this radiation, and the most plausible explanation has been the cooling of the primordial gas through scattering interactions with dark matter. During this epoch, SM particles were too energetic to be able to cool the gas through scattering. Therefore, only DM in the right energy range could explain the results [211, 209, 212, 213, 214]. Such a possible interaction is explored in Refs. [215, 216, 217]. Constraints from cosmology and particle experiments indicate that this DM should be light (∼10–80 MeV), carry a small charge ($\epsilon \sim 10^{-6}$–10^{-4}), and only make up a small fraction of the total amount of DM [216]. Several constraints on the DM parameter space under these conditions have already been made. In Fig. 1.11, taken from Ref. [216], these constraints are shown.

In chapter 3 , we explore the yet unconstrained region in the case that the milli-charged DM makes up for ∼2% of the total dark matter, through the scenario in which this DM annihilates only into muon and tau neutrinos. We set upper limits on the annihilation cross section using Super-Kamiokande data, and predict the limits that

could be obtained through Hyper-Kamiokande, JUNO and DUNE. We furthermore explore light DM annihilation into solely neutrinos in general, giving an update of the current limits, and predict the limits that could be placed with future experiments.

2 Impact of axisymmetric mass models for dwarf spheroidal galaxies on indirect dark matter searches

Dwarf spheroidal galaxies are low-luminosity satellite galaxies of the Milky Way highly dominated by DM. Therefore, they are prime targets to search for signals from dark matter annihilation using gamma-ray observations. While the typical assumption is that the dark matter density profile of these satellite galaxies can be described by a spherical symmetric NFW profile, recent observational data of stellar kinematics suggest that the DM halos around these galaxies are better described by axisymmetric profiles. Motivated by such evidence, in this chapter we discuss our analysis of about seven years of `PASS8` *Fermi*-LAT data for seven classical dwarf galaxies, including Draco, adopting both the widely used NFW profile and observationally-motivated axisymmetric density profiles.

The work in this chapter previously appeared in [1].

1 Introduction

Most of the matter in the Universe consists of an unknown component that is commonly considered to be made of non-baryonic cold dark matter [218, 106]. Finding the particle nature of dark matter is one of the most pressing goals in modern physics. While many particle physics models have been proposed to solve this puzzle, the most favored and extensively studied candidates fall into the category of weakly interacting massive particles [219]. These are characterised by a relic density matching the observed DM density, and naturally arise in many theories beyond the standard model of particle physics such as supersymmetry or universal extra-dimension models. The self-annihilation of WIMPs can result in the production of standard model particles.

The goal of so-called indirect DM searches is to look for these particles in regions of the Universe where we know DM is abundant [220].

High-energy gamma rays are one example of those particles expected as a result of WIMP annihilation. The search for these gamma rays is a very active field of research fueled in the last decade by many gamma-ray observations of Milky Way satellite galaxies [221, 222, 223, 224, 225, 226, 227, 228, 229, 230, 200, 206, 231, 232, 233] and other promising sites such as the Galactic center [234, 235, 236, 237, 238, 239, 240, 188] or clusters of galaxies [241, 242, 243, 244, 245, 246, 247, 248], both from the ground with imaging Cherenkov telescopes and from space with the *Fermi* Large Area Telescope. More recently, novel and competitive constraints have been obtained also from the *Fermi* measurements of the extragalactic gamma-ray background [249, 250, 251, 252, 253, 254, 255, 256, 257, 258, 259, 260].

In this chapter, we focus on dwarf spheroidal galaxies that are low-luminosity satellite galaxies which are known to be highly DM dominated [261, 262, 263, 264, 265]. Their high mass-to-light ratio, proximity, and very low expected gamma-ray background from other astrophysical sources make them ideal candidates to search for gamma rays from DM annihilation. The main astrophysical uncertainty when dealing with indirect DM searches in dSphs is their DM density profile, which is the most crucial ingredient needed to estimate the rate of DM annihilation we expect from a given object. The common assumption often adopted in the literature is that dSphs are characterised by a spherically symmetric, so-called Navarro-Frenk-White profile [152]. This cusped profile originally predicted by N-body simulations of cold dark matter might not be the best choice for all cases, and other profiles have been extensively discussed in the literature, including the Einasto profile [266].

Additional complications come from going beyond simple spherical symmetric mass models. We know, in fact, that the observed stellar components of all MW dSphs have an axisymmetric shape on the sky-plane with typical axial ratios of 0.6–0.8 [267]. Additionally, recent high-resolution N-body simulations showed that DM subhalos tend to have axisymmetric shapes rather than triaxial [268]. These considerations prove the need to relax the assumption of spherical symmetry in the mass modeling of dSphs, which is also one of the major systematic uncertainties for the J-factor (i.e., the line-of-sight integral of DM density squared) estimations that most of previous studies have not considered.

In this chapter we investigate the impact of observationally motivated axisymmetric mass models on indirect DM searches with dSphs using gamma-ray observations by *Fermi*. Uncertainties on the J-factor estimates were addressed in Ref. [269], where

they explore the impact of the observationally unknown star orbital anisotropy. Triaxial density profiles have been investigated in detail in Ref. [270], where they determine the bias on the J-factor that arises when using a spherical Jeans analysis for halos that are likely to be triaxial in shape. In our work, we go beyond the J-factor estimates and study the impact on the upper limits obtained for the DM cross section when adopting the axisymmetric models of Ref. [171] with respect to those obtained using the commonly adopted NFW profile. We analyse about seven years of `PASS8` *Fermi*-LAT data for seven classical dSphs, namely Draco, Leo I and II, Sextans, Carina, Sculptor, and Fornax. These dSphs are selected as the overlapping part of the samples considered by Ref. [171] and Ref. [200]. We fit each dSph both with NFW and axisymmetric profiles, and compare their cross section upper limits. We underline, in particular, that Sextans, Carina, Sculptor and Fornax are characterised by cored axisymmetric profiles rather than cusped, and their results can differ significantly from those of the NFW profiles.

This chapter is organised as follows. In Sec. 2, we discuss the expected flux from DM annihilation from dSphs in the case of a NFW profile. The axisymmetric mass model is introduced in Sec. 3, where we also discuss a qualitative comparison with the NFW profile. In Sec. 4, we discuss the *Fermi*-LAT data analysis for the seven selected dSphs and present our results in Sec. 5. We discuss our conclusions in Section 4.

2 Gamma rays from dark matter annihilation

The gamma-ray intensity (i.e., the number of photons received per unit area, time, energy, and solid angle) from a direction ψ relative to the center of the halo, expected from DM annihilation can be written as

$$\phi_{\rm WIMP}(E,\psi) = J(\psi)\Phi^{\rm PP}(E), \tag{2.1}$$

where $J(\psi)$ is the astrophysical factor, also called J-factor, which describes the DM density distribution in the region of interest, and $\Phi^{\rm PP}(E)$ is the particle physics factor, which encloses the properties of the DM particle.

The particle physics factor can be written as

$$\Phi^{\rm PP}(E) = \frac{1}{2}\frac{\langle\sigma v\rangle}{4\pi\, m^2_{\rm WIMP}}\sum_f \frac{dN_f}{dE}B_f, \tag{2.2}$$

where $m_{\rm WIMP}$ is the WIMP mass, $\langle\sigma v\rangle$ is the the annihilation cross section multiplied by the relative velocity of the annihilating particles averaged over their velocity dis-

tribution, and dN_f/dE is the photon spectrum of the final state f with its branching ratio B_f.

The astrophysical J-factor is

$$J(\psi) = \int_{\text{l.o.s.}} \rho^2(l, \psi)\, dl, \tag{2.3}$$

where l is the line-of-sight parameter, and $\rho(l, \psi)$ is the DM density profile. As mentioned in Sec. 1, in our analysis of the *Fermi*-LAT data we compare the observationally-motivated axisymmetric DM density profile with the widely used spherically-symmetric NFW profile. The current section concerns the latter.

The NFW profile is given by [152]

$$\rho(r) = \begin{cases} \frac{\rho_s r_s^3}{r(r_s+r)^2} & \text{for } r < r_t \\ 0 & \text{for } r \geq r_t \end{cases}, \tag{2.4}$$

where ρ_s is the characteristic density, r_s is the scale radius, and r_t is the tidal radius beyond which all the DM particles are stripped away due to a strong tidal force from the host halo. We calculate the values for ρ_s and r_s from the parameters $v_{\max}$ and $r_{\max}$ provided by [271] using the following relations:

$$r_s = \frac{r_{\max}}{2.163}, \tag{2.5}$$

$$\rho_s = \frac{4.625}{4\pi G} \left(\frac{v_{\max}}{r_s} \right)^2, \tag{2.6}$$

where G is the gravitational constant. We then derive r_t from the Jacobi limit [272],

$$r_t = D \left(\frac{M_{\text{dSph}}}{3M_{\text{MW}}} \right)^{\frac{1}{3}}, \tag{2.7}$$

where M_{dSph} is the mass of the dSph and D is the distance of the dSph from the MW center. M_{MW} is the MW mass enclosed within the distance D, calculated assuming an NFW profile from Ref. [273]. M_{dSph} is calculated integrating the dSph NFW profile up to r_t, and we eventually solve equation (2.7) to obtain r_t. Note that the tidal radius calculated in this way is subject to various uncertainties connected to the mass estimate of the Milky Way and to several assumptions made for simplicity, such as a perfect circular orbit of the dSph around the stable MW potential. However, typically about 90% of the annihilation flux comes from within r_s for an NFW profile (see, e.g., [264]) and, therefore, variations on the tidal radius will only have little effects on the resulting J-factor. The main characteristics of each considered dSph are reported in Table 2.1.

Name	Distance	ρ_s	r_s	r_t	NFW J-factor		axisymmetric J-factor	
					total	$< 0.5^\circ$	total	$< 0.5^\circ$
	[kpc]	$[M_\odot \mathrm{kpc}^{-3}]$	[kpc]	[kpc]	[GeV^2 cm^{-5} sr]	[GeV^2 cm^{-5} sr]	[GeV^2 cm^{-5} sr]	[GeV^2 cm^{-5} sr]
Draco	76	2.30×10^8	0.3507	0.96	8.33×10^{18}	8.24×10^{18}	9.43×10^{18}	8.71×10^{18}
Leo I	254	1.59×10^8	0.4027	6.26	5.06×10^{17}	5.05×10^{17}	3.95×10^{17}	3.94×10^{17}
Leo II	233	1.83×10^8	0.3055	4.73	3.32×10^{17}	3.32×10^{17}	3.18×10^{17}	3.17×10^{17}
Carina	105	3.04×10^8	0.2065	3.39	1.50×10^{18}	1.49×10^{18}	2.61×10^{18}	2.36×10^{18}
Fornax	147	1.33×10^8	0.4731	5.30	1.83×10^{18}	1.81×10^{18}	1.67×10^{18}	1.52×10^{18}
Sculptor	86	1.67×10^8	0.3935	3.25	4.91×10^{18}	4.79×10^{18}	6.75×10^{18}	5.76×10^{18}
Sextans	86	3.82×10^8	0.2018	1.55	3.37×10^{18}	3.37×10^{18}	2.03×10^{18}	1.24×10^{18}

Table 2.1: Characteristics of the analysed dwarf spheroidal galaxies. The top ones are cusped while bottom ones are cored in the axisymmetric mass modeling. The distances are taken from Ref. [200].

Equation (2.3) yields the J-factor as a function of the angle between the line of sight and the center of the dSph. We project this onto a spatial map of 100×100 pixels of 0.1° centered on each dSph. These will be the template input for the *Fermi*-LAT data analysis of each dSph that is described in Sec. 4. We show the obtained NFW template maps in Figs. 2.1 and 2.2, where the total flux is normalized to unity.

Our reference works for the gamma-ray limits on dSph are those of Refs. [228, 200]. However, while Refs. [228, 200] limit their analysis within 0.5° of each dSph, we do not limit the emission region in our analysis. Our choice is motivated by the fact that we want to compare the upper limits on the DM cross section obtained when adopting the NFW profiles against those obtained when adopting axisymmetric ones. As we will discuss in detail in the next section, the axisymmetric profiles are typically more extended compared to the NFW profiles. In Table 2.1, we show the total J-factor together with the one calculated within a radius of 0.5° both for the NFW and the axisymmetric profiles. While for the NFW profiles the differences are insignificant, with maxima of about 1 and 2.5% for Draco and Sculptor, respectively, the differences in the case of the axisymmetric mass models are much more severe in most cases, except for Leo I and II. In particular, in the case of Sextans, about 40% of the total axisymmetric J-factor would be ignored by considering only a region within 0.5°. Therefore, in order to have a consistent comparison between the NFW and the axisymmetric profiles, we do not limit the emission region of our dSphs in the data analysis and use r_t as outermost radius in the generation of the template input maps for the NFW case.

Finally, note that our NFW J-factors do not necessary have to coincide with those of Refs. [228, 200] as they use the method of Ref. [271] applied to stellar kinematics data to obtain their J-factors, while we use directly the $v_{\max}$ and $r_{\max}$ provided by

Ref. [271]. Nevertheless, our total J-factors integrated up to r_t are always within the quoted errors of the J-factors from Refs. [228, 200], with the notable exception of Leo II where ours is almost a factor of 2 smaller. With this exception in mind, we expect the limits that we calculate for NFW profiles to be comparable to those of Refs. [228, 200], except for the fact that here we consider events from a larger energy range.

3 Axisymmetric Mass Models

Our aim is to compare the constraints obtained using an NFW density profile to those obtained by using the observationally-motivated axisymmetric density profile. For the axisymmetric model, we use the non-spherical DM halo structure estimated by Ref. [171] to compute the J-factor maps. In this section, we briefly introduce the mass models based on the axisymmetric Jeans equations, the method of exploring the best-fit DM halo parameters, and the fitting results (for more details, we refer the reader to the original papers [171, 274]).

Assuming that the stellar tracers in the dSphs are in dynamical equilibrium with a gravitational smooth potential dominated by DM, the distribution function obeys the steady-state collisionless Boltzmann equation [275]. Given that both the stellar and DM components are axisymmetric, the axisymmetric Jeans equations can be derived from this equation by computing its velocity moments. When the distribution functions are of the form $f(E, L_z)$, where E and L_z are the energy and the angular momentum along the symmetry axis z respectively, the mixed moments vanish and the velocity dispersion of stars in cylindrical coordinates, $\overline{v_R^2}$ and $\overline{v_z^2}$, are identical; i.e., the velocity anisotropy parameter $\beta_z = 1 - \overline{v_z^2}/\overline{v_R^2}$ is exactly zero. However, since in general these velocity second moments are not identical, Ref. [171] adopted Cappellari's formalism that relaxed $\overline{v_R^2} = \overline{v_z^2}$ and assumed $\beta_z =$ constant [276]. In addition, they assumed that the dSph stars did not rotate, and therefore the velocity second moment was equivalent to the velocity dispersion.

Under these assumptions, the axisymmetric Jeans equations are written as

$$\overline{v_z^2} = \frac{1}{\nu(R,z)} \int_z^\infty \nu \frac{\partial \Phi}{\partial z} dz, \tag{2.8}$$

$$\overline{v_\phi^2} = \frac{1}{1-\beta_z} \left[\overline{v_z^2} + \frac{R}{\nu} \frac{\partial (\nu \overline{v_z^2})}{\partial R} \right] + R \frac{\partial \Phi}{\partial R}, \tag{2.9}$$

where ν is the three-dimensional stellar density profile and Φ is the gravitational potential. In order to compare them with the observed velocity second moments, the

above equations should be integrated along the line of sight. Following the method given in Ref. [277], we computed the projected velocity second moments from $\overline{v_R^2}$, $\overline{v_\phi^2}$, and $\overline{v_z^2}$, taking into account the inclination of each dSph with respect to the observer. For the stellar and DM halo density models, which are related to ν and Φ, we adopted an axisymmetric Plummer profile [278] (see Eq. 3 in [171]) and an axisymmetric double power-law form (see Eq. 4 in [171]), respectively.

Comparing the line-of-sight velocity moment profiles from theory and observations, Ref. [171] estimated the best-fit free parameters by using a Markov Chain Monte Carlo fitting method. There is a total of six free parameters in this model: the axial ratio, characteristic density and scale radius of the DM halo, the inner slope of the DM profile, the velocity anisotropy parameter and the inclination angle of the dSph. Applying their models to the available data of the seven MW dSphs (Carina, Fornax, Sculptor, Sextans, Draco, Leo I and Leo II), two important outcomes were found. First, while Leo I and Leo II have almost spherical dark halos, the other dSphs (Carina, Fornax, Sculptor, Sextans and Draco) are likely to have very flattened and oblate DM halos, with axial ratios of $\sim$0.4, even though there is a degeneracy between the axial ratio of the dark halo and the constant velocity anisotropy parameter. For example, the axisymmetric model for Sextans is preferred over a spherical symmetric one at around 2σ confidence level. Second, not all the DM halos in the dSphs have a cusped central density profile. Most of the dSphs indicate cored density profiles or shallow cusps. Exceptions are Draco and Leo I, which show a cusped profile with inner density slopes of -0.86 ± 0.11 and $-1.40^{+0.06}_{-0.08}$ respectively. The best-fit parameters of each dSph are summarized in Table 2 of Ref. [171]. We use these parameters to compute the sky distribution of the J-factors for Draco, Leo I, Leo II, Sextans, Carina, Sculptor and Fornax.

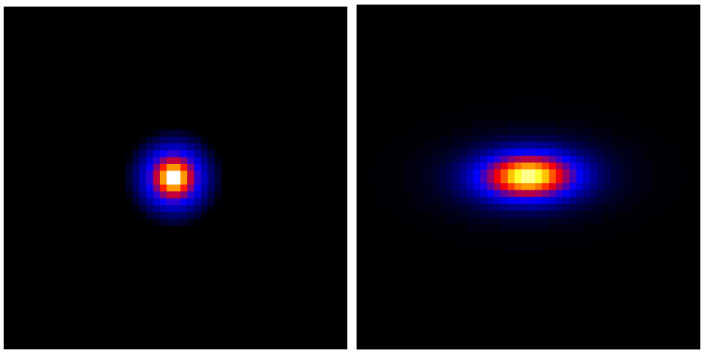

(a) Draco NFW (b) Draco axisymmetric

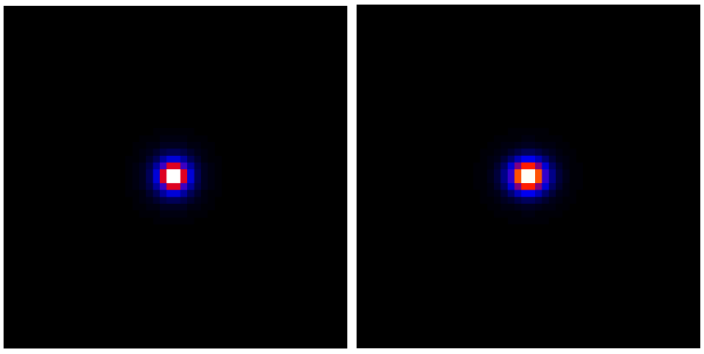

(c) Leo I NFW (d) Leo I axisymmetric

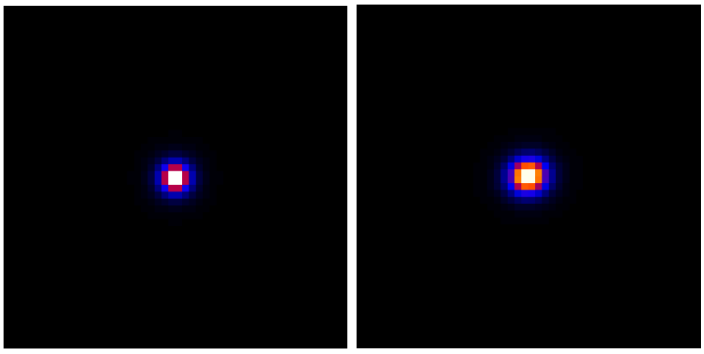

(e) Leo II NFW (f) Leo II axisymmetric

Figure 2.1: DM density profiles projected onto the sky for the dSphs that have a cusped halo profile in log scale. From top to bottom, Draco, Leo I and Leo II, where the NFW profiles are shown on the left, and the axisymmetric profiles are shown on the right. The total flux of all images is normalised to unity, and the colour scale is the same in each pair of figures for every dSph. The maps are cropped to correspond to a $5^\circ \times 5^\circ$ region in the sky.

Figures 2.1 and 2.2 show both the NFW and axisymmetric density profiles projected onto the sky for the seven adopted dSphs.These are the spatial templates that are used in the *Fermi*-LAT data analysis of Sec. 4.The total flux in these maps is normalised to unity, and the colour scale of each pair NFW-axisymmetric is set to be the same, thus showing the relative size and brightness of the two models for a given dSph. As explained in the previous sections, when generating these template maps, the outermost radius is taken to be r_t for the case of the NFW profiles. In the case of the axisymmetric profiles, for which r_t values are not estimated within the framework of Ref. [171], there is no formal limit to the radial extent of the profiles in the template maps. We stress, however, that as in both cases most of the annihilation flux comes from the inner parts, even though with the due differences (see Table 2.1), the choice of the outermost radial extent has no impact on our results.

Figure 2.1 shows the dSphs with a cusped density profile. For Leo I and Leo II, there is almost no visible difference between the NFW and the axisymmetric profiles projected onto the sky. For Draco, the shape of the axisymmetric model is oblate instead of spherical and clearly differs from the classical NFW, but still shows a cuspy. The differences between the two profiles are larger for the cored dSphs as can be seen in Fig. 2.2. In this case, the axisymmetric profiles are much more extended than the NFW profiles, with the total integrated J-factor being of the same order of magnitude, but distributed over a larger area (see also Table 2.1). Note also that these axisymmetric profiles are all oblate and characterised by different directions of the major axis following the stellar kinematics data for a given dSph. We will show that the case of the cored dSphs is the most affected by the simplification of adopting the NFW profile when obtaining DM constraints.

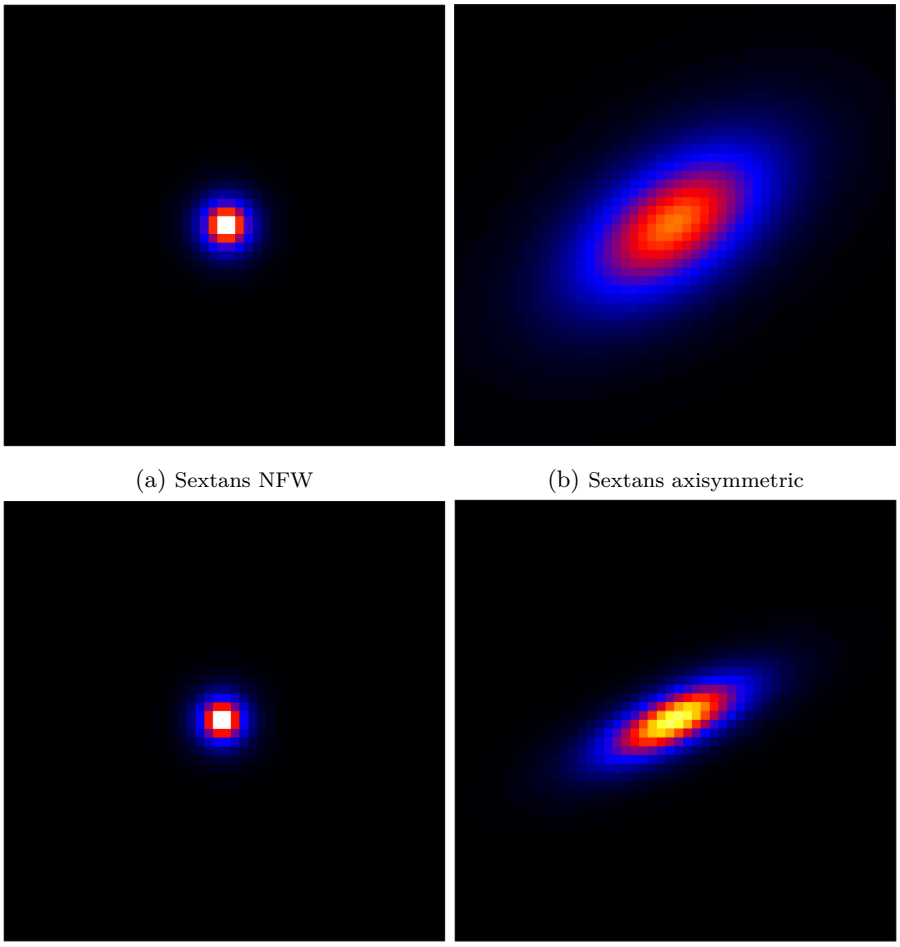

(a) Sextans NFW

(b) Sextans axisymmetric

(c) Carina NFW

(d) Carina axisymmetric

Figure 2.2

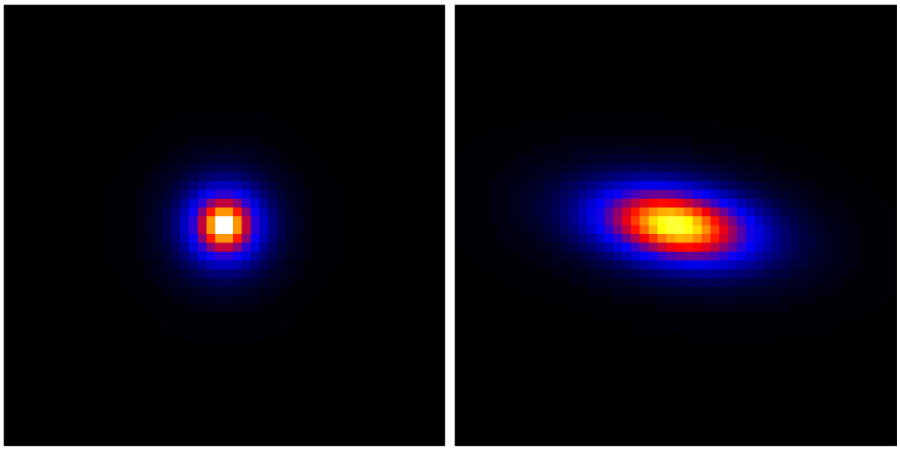

(e) Sculptor NFW (f) Sculptor axisymmetric

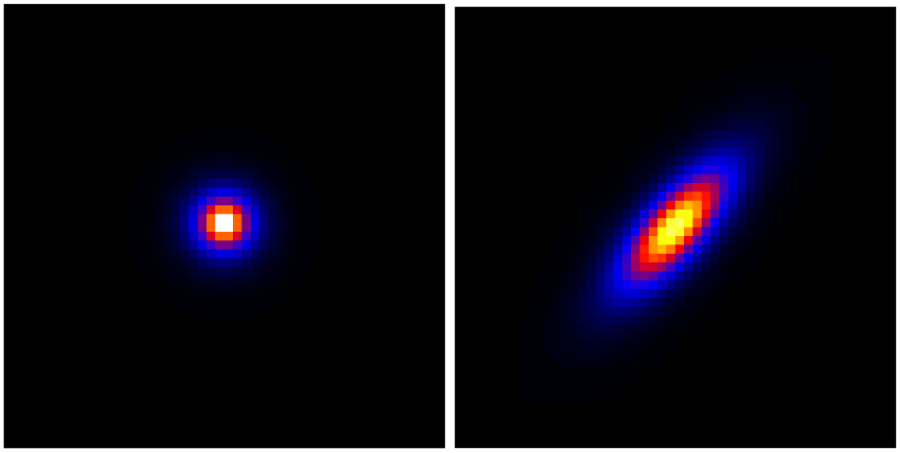

(g) Fornax NFW (h) Fornax axisymmetric

Figure 2.2: DM density profiles projected onto the sky for the dSphs that have a cored halo profile in log scale. From top to bottom, Sextans, Carina, Sculptor and Fornax, where the NFW profiles are shown on the left, and the axisymmetric profiles are shown on the right. The total flux of all images is normalised to unity, and the colour scale is the same in each pair of figures for every dSph. The maps are cropped to correspond to a $5^\circ \times 5^\circ$ region in the sky.

4 Data Selection and Analysis

We analyse 86 months (August 4th 2008 15:43:36 till October 15th 2015 02:34:52) of *Fermi*-LAT `PASS8` data in the direction of the selected dSphs using the `v10r0p5` version of the *Fermi Science Tools*. We follow Ref. [200] for the selection of event class and type (`evclass`=128, `evtype`=3) and for the data cuts, which are standard, and use the corresponding instrumental response functions. We analyse a region of interest (ROI) of $10^\circ \times 10^\circ$ around each dSph, with 0.1° pixels, and perform a binned likelihood analysis in 24 logarithmically-spaced energy bins from 100 MeV to 50 GeV.

We perform the analysis including all the sources included in the third *Fermi* catalog (3FGL; [81]) within a region with a radius of 25° around the center of our ROI for each dSph. For the diffuse background, we adopt the latest Galactic diffuse model (`gll_iem_v06`) and the extragalactic isotropic diffuse model (`iso_P8R2_SOURCE_V6_v06`) as provided by the *Fermi* collaboration. We allowed the spectral parameters of the sources to vary within a circle of radius 7.07°—the radius of our ROI—together with the normalisation of the diffuse background components, while the remaining sources are kept fixed to the 3FGL values.

The so-obtained model is complemented in each case with the spatial models of Figs. 2.1 and 2.2 for the dSphs' DM-induced emission. For each dSph, we run two separate analyses with the corresponding NFW and axisymmetric profiles. The spectral part of our dSphs' models is constructed using Eq. (2.2) adopting the corresponding J-factor for the NFW or axisymmetric model from Table 2.1, and making a guess for the value of $\langle\sigma v\rangle$—the parameter that we will constrain. As for the photon spectrum dN_f/dE, we adopt `PYTHIA` [279] for the $b\bar{b}$ final state. The normalisation of our dSphs' models is left free. In each case, we repeat the analysis for 18 values of the DM masses from 10 to 5000 GeV.

We run the binned likelihood analysis following the above prescriptions for each dSph, for both a NFW and an axisymmetric profile, and for each DM mass. When convergence is not achieved, we iterate by filtering out the faintest sources in our model with test statistic (TS) values ≤ 1, and subsequently ≤ 2, while making sure that the model is still a good description for the data. We eventually calculate 95% confidence-level integrated flux upper limits between 100 MeV and 50 GeV for all cases and derive limits on the DM annihilation cross section that we discuss in detail in the next section.

Before we move on to the results, we comment on the model used for the analysis of Sextans. The residual map for Sextans showed the presence of an unmodeled

excess at about 3.5° from the center of the ROI, as shown in Fig. 2.3, for which we did not find any correspondence in the 3FGL catalog or in the literature. The position of this excess is roughly $(155.93, 0.65)$ in celestial coordinates. We fit this excess with a point source described by a simple power law spectrum. We found that this source had a TS value around 1460 and its spectrum was well described by $dN/dE = 12.14 \times 10^{-9} \, (E/28.04 \text{ MeV})^{-2.39} \, \text{cm}^{-2} \, \text{s}^{-1} \, \text{MeV}^{-1}$, with normalisation and spectral index having variations below 1% among the various analyses we ran for the NFW and axisymmetric profiles and different DM masses. In Fig. 2.3 we show the residual map before and after including this source for one of the analyses. We do not attempt any further modeling or interpretation for this excess, considering our fit just an effective model for it. We are confident that this is a good description of the data for the purposes of our work, also because the derived upper limits on the annihilation cross section from Sextans differ very little if we do or do not model this excess out from the data. Nevertheless, the results that we will discuss in the following section refer to the case where we model this source out.

Note that the *Fermi* Collaboration published results using energies from 500 MeV to 500 GeV [228, 200] while we use the 100 MeV to 50 GeV energy range. In particular, Ref. [200] excluded events below 500 MeV to mitigate the impact of leakage from the bright limb of the Earth. As the same analysis chain is applied to both profile types, the choice of the energy range do not impact the conclusions of our work, i.e., the comparison of the exclusion limits on the DM cross section between NFW and axisymmetric profiles. To confirm this, we perform the analysis of Sextans, which, as will be discussed in the next section, shows the largest difference between the two models, also in the energy range between 500 MeV to 50 GeV. The results are shown in the top right panel of Figure 2.5. As expected, the limits improve when excluding lower energy events from our analysis, particularly for low DM masses. The limits are consistently better for all tested DM masses in the case of a NFW profile, while in the case of the axisymmetric profile, the limits obtained in the 500 MeV$-$50 GeV range slightly worsen for DM masses above about 100 GeV. At any rate, the relative comparison between the constraints obtained with NFW and axisymmetric profiles is not affected by the choice of the energy range.

5 Results

We find no gamma-ray excess in any of the dSphs using both the NFW profile and the axisymmetric models. For most of the dSphs and DM masses, we find test statistic (TS) values around zero, and no TS values were larger than 6.06, which was the case

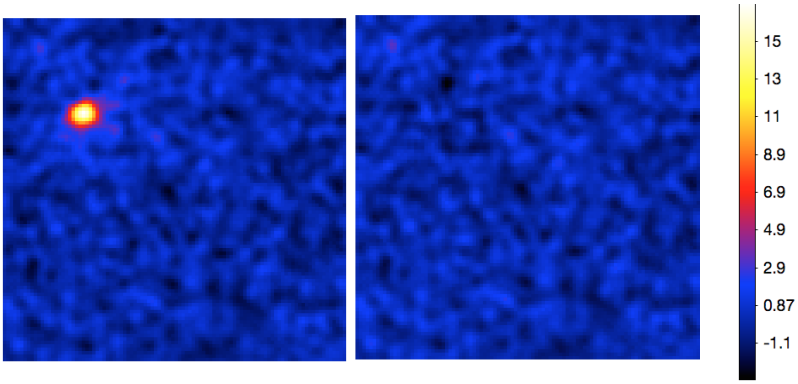

Figure 2.3: Maps for Sextans, covering $10^\circ \times 10^\circ$ of the sky. On the left is the residual map before modeling the source, on the right the residual map after modeling the source. The residual maps represent subtractions of the model map from the counts map, therefore the color code refers to residual photon counts.

for Fornax using the axisymmetric profile (5.6 using the NFW profile) and a DM mass of $m_{\rm WIMP} = 10$ GeV. Therefore we calculate flux upper limits that we then convert to limits on the annihilation cross section.

We find differences between the cross section upper limits achieved through the two different models of the halo profile. In Figs. 2.4 and 2.5, we show the cross section upper limits for the seven analysed dSphs. Figure 2.4 shows that the dSphs that are expected to have a cusped profile show small differences in the upper limits for the two analysed halo models. Despite the difference in the shape of the two halos (spherical vs oblate), we find that the NFW profile provides a good approximation of the actual halo of these dwarfs.

The impact of the different profiles is more significant for the four dSphs that have a cored profile as suggested by the observationally motivated profile we adopted and shown in Fig. 2.5. In particular, we find the largest difference of about a factor of 2.5–7, depending on the DM-particle mass, in the case of Sextans, where we see that the axisymmetric model is most extended compared with the corresponding NFW profile as shown in Fig. 2.2. The upper right panel in Fig. 2.5 shows the resulting cross section upper limits of Sextans derived both in the energy range 100 MeV−50 GeV and 500 MeV−50 GeV. As anticipated in the previous section, the difference between the NFW and axisymmetric profiles is unaffected by this choice. It is, in fact, even slightly larger – a factor of 3–11 depending on the DM-particle mass – for the 500 MeV−50 GeV energy range. Therefore, given that Sextans was one of the most

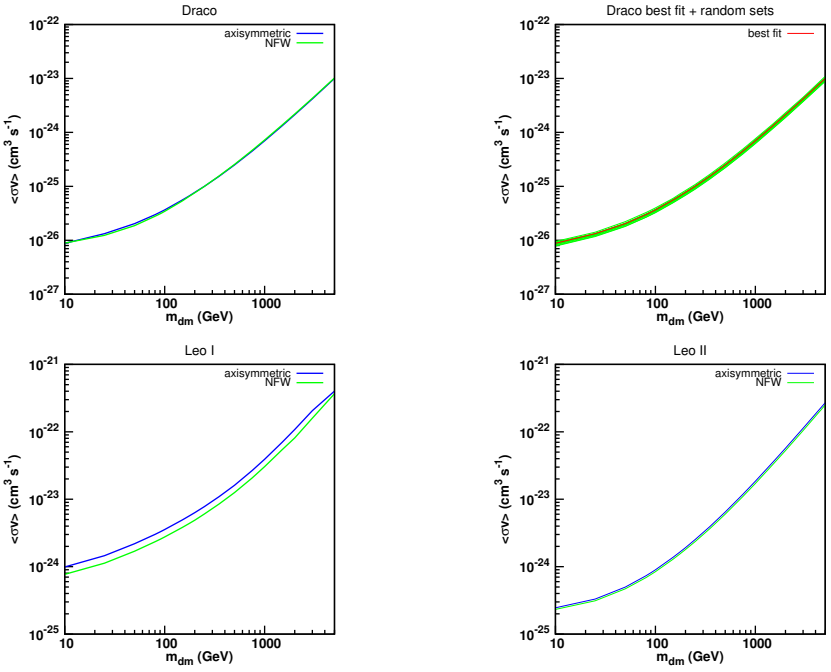

Figure 2.4: Dark matter annihilation cross section upper limits in the $b\bar{b}$-channel for the dSphs with a cusped profile. The upper right frame shows the cross section upper limits obtained through the analysis of 10 axisymmetric profiles for Draco, corresponding to 10 random sets of the profile parameters from the Monte Carlo sample of Ref. [171], along with the best-fit case.

important dSphs with the spherically symmetric model, i.e., cross section upper limits reached the canonical value 3×10^{-26} cm^3 s^{-1} for low-mass WIMPs, we show that it is indeed relevant to use a more accurate model for its density profile.

The most stringent constraints on $\langle \sigma v \rangle$ are obtained for Draco, whose J-factor is the largest among the seven dSphs analyzed here. In this case, the canonical annihilation cross section $\langle \sigma v \rangle = 3 \times 10^{-26}$ cm^3 s^{-1} can be tested for WIMPs lighter than $\sim$80 GeV, and since the DM density is described by the cusped profile, there is only little difference between the spherical and axisymmetric models. Although the results of the combined likelihood analysis (e.g., Ref. [200]) will be dominated by the most promising dSphs such as Draco, others, such as Sextans discussed above, will also give a substantial contribution. Therefore, the inclusion of observationally-motivated axisymmetric profiles would make the joint likelihood analysis of the dSphs slightly weaker compared to the previous analysis in the literature.

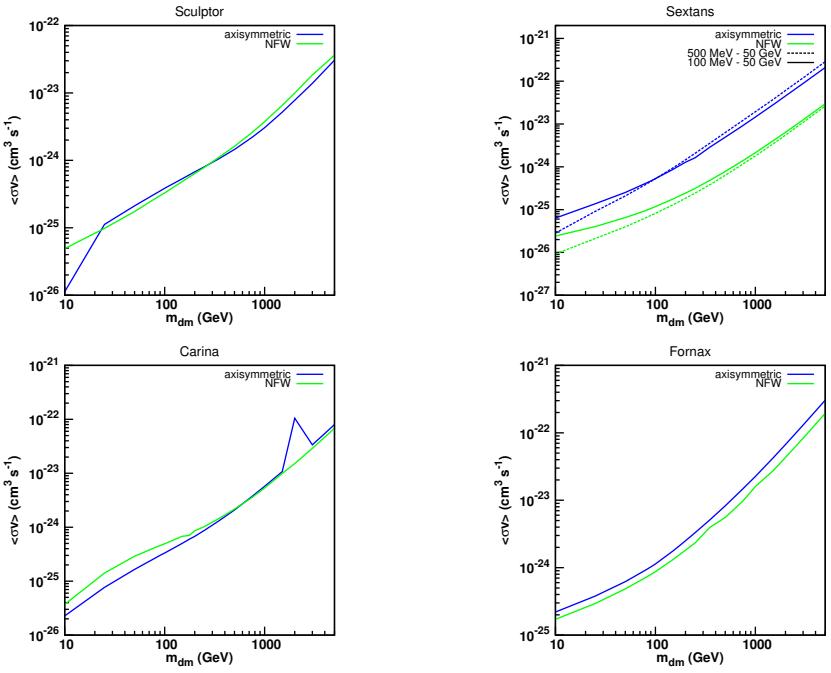

Figure 2.5: Dark matter annihilation cross section upper limits in the $b\bar{b}$-channel for the dSphs with a cored profile.

To test the impact of measurement uncertainties of stellar kinematics data on these gamma-ray constraints, we randomly choose ten sets of the parameters from the Monte Carlo sample of Ref. [171] for the Draco axisymmetric profile, and obtain the cross section upper limits for each, whose results are shown in the upper right panel of Fig. 2.4 along with the best-fit case. This shows that the current stellar kinematics data are well determined, giving only uncertainties on the cross section upper limits of about 10%, which makes dSphs a robust, and hence, attractive object to test DM annihilation.[1] This also shows that our comparison between NFW and axisymmetric profiles is not significantly affected by the uncertainties on the latter and that our conclusions are robust.

We note that a kink around ∼2 TeV for the axisymmetric model of Carina as well as

[1] We generated 100 random sets from the Monte Carlo sample of Ref. [171] for the Draco axisymmetric profile. We then randomly select only 10 of these on which to run our *Fermi* analysis for each DM mass, as this can be a quite lengthy process. We note, however, that the difference in the total J-factors of the original 100 sets is within few percent at most. Therefore, we believe that our choice of running only 10 sets provided robust results.

a drop toward ∼10 GeV of Sculptor is likely caused by some complicated interplay between the adopted profile, energy spectrum, and photon count distribution that we interpret as a statistical fluctuation, also considering that the models for these particular cases of $m_{\rm dm}$ show no substantial difference, i.e., in TS significance, with respect to the others.

Finally, we note that although evaluating the integrated J-factor will capture the overall importance of each dSph, it is not until one performs the likelihood analysis that we know how the cross section upper limits behave as a function of the WIMP mass. In fact, the difference in the cross section upper limits comes from an interplay of the normalisation and shape of the J-factor. For example, the difference between the J-factors is larger for Leo I than for Fornax, with a value of 0.78 against 0.91 for the ratio $J_{\rm axisymmetric}/J_{\rm NFW}$. The difference between the upper limits however is larger for Fornax, where the upper limit for the axisymmetric case is up to 1.57 times larger than the NFW case, while up to 1.33 times larger in the case of Leo I. So the difference between the shapes of the halo models has a larger contribution to the difference in the cross section upper limits than the difference between the total J-factors. While Ref. [270] studied J-factors for a comprehensive list of dSphs, our focus is on the classical seven dSphs that have the best measurements of stellar kinematics, and we performed the likelihood analysis for all of them. Therefore, these two approaches are complementary to each other.

Before moving to the conclusions, we want to underline that the cross section upper limits shown here, differently from Refs. [228, 200], are obtained without taking in consideration any uncertainty, i.e., without marginalising over the uncertainty on, e.g., the J-factor determination. However, this has no impact on the relative comparison that we set out to make between the NFW and axisymmetric profiles.

6 Conclusion

Dwarf spheroidal galaxies are important and well established targets for indirect DM searches. The most common choice for the DM density profile in the analysis of these dSphs is an NFW profile. Recent observational data of stellar kinematics, however, imply that DM halos around these galaxies are better described by an axisymmetric profile, with an axis ratio of 0.6–0.8, either cored or cusped. For this reason, we investigated the impact of adopting observationally-motivated axisymmetric models instead of the commonly adopted NFW profile on the limits obtained for the DM annihilation cross section for seven classical dSphs with *Fermi* gamma-ray data.

Draco is the most promising dwarf galaxy among the seven analysed. Although its DM distribution is well described by a cusped oblate profile in the axisymmetric modeling, the total amount of gamma rays yielding from the overall region will be similar to that of an NFW profile (i.e., similar J-factors). As a result, we obtained very similar upper limits on the annihilation cross section for Draco using an NFW and axisymmetric model. The same is true for Leo II, while Leo I shows some mild differences, even if both feature an inner cusp. By testing ten axisymmetric profiles randomly chosen from a Monte Carlo sample of the analyses of stellar kinematics data of Draco, we find that the current uncertainty on the density profile of Draco will give a systematic uncertainty on the cross section upper limits of about 10%. This proves that our conclusions are robust.

The analyses of the dSphs best described by a cored profile (Sextans, Sculptor, Carina and Fornax) result in a more substantial difference between the two adopted profiles. In particular, for Sextans, the best-fit model of its stellar kinematics data yields a much more extended J-factor map. We found that the cross section upper limits were weaker by a factor of a few to several compared with those obtained with an NFW profile. This demonstrates the importance of properly assessing DM density profiles from observational data, and also that upper limits in the literature obtained assuming a cusped spherical model (such as an NFW) might be overestimated.

3 Constraints on MeV dark matter using neutrino detectors and their implication for the 21-cm results

The recent results of the EDGES collaboration indicate that during the era of reionization, the primordial gas was much colder than expected. The cooling of the gas could be explained by interactions between dark matter and particles in the primordial gas. Constraints from cosmology and particle experiments indicate that this DM should be light ($\sim$10–80 MeV), carry a small charge ($\epsilon \sim 10^{-6}$–10^{-4}), and only make up a small fraction of the total amount of DM. Several constraints on the DM parameter space have already been made. In this chapter, we explore the yet unconstrained region in the case that the milli-charged DM makes up for $\sim$2% of the total dark matter, through the scenario in which this DM annihilates only into muon and tau neutrinos. We set upper limits on the annihilation cross section using the Super-Kamiokande data, and predict the limits that could be obtained through Hyper-Kamiokande, JUNO and DUNE. We furthermore explore DM annihilation into solely neutrinos in general, giving an update of the current limits, and predict the limits that could be placed with future experiments.

The work in this chapter previously appeared in [3].

1 Introduction

Early stars are expected to have imprinted their evidence in the cosmic microwave background. Their ultraviolet light hit the primordial hydrogen gas, resulting in emission at the 21 cm line. As a response to this, the absorption from CMB photons by the primordial gas caused a spectral signal in the CMB that we should be able to observe today. The recent 21-cm results of the EDGES collaboration [209] show

an absorption profile that is consistent with the expected effect induced by the early stars, although showing an amplitude twice as large as predicted. This result implies that the temperature of the primordial gas was much lower than expected, or that the temperature of the background radiation was higher than expected.

A possible explanation consistent with the observed results is the cooling of the gas due to interactions with dark matter [209, 211, 212, 213, 214], which is causing a lot of excitement in the field. The possibility of such a DM interaction is studied in Refs. [215, 216, 217], in which multiple constraints are put on the nature of the responsible DM. Using data from a variety of experiments, it is found that most of the parameter space that is consistent with the 21-cm observations is ruled out [216]. The DM responsible for the cooling could only make up for a small fraction of the total DM, ∼0.3–2%, and their mass lies in the range of ∼10–80 MeV. Furthermore, the DM should carry a small electric charge in the order of $\epsilon \sim 10^{-6}$–10^{-4}.

However, assuming that DM interacts with baryons mediated by only photons produces too much DM through thermal freeze-out mechanism. In order to circumvent this issue, DM must have at least one more interaction channel with the standard model particles. The simplest possilibity that has not been ruled out yet is that the DM interacts with lepton number $L_\mu - L_\tau$ via either a scalar or vector mediator [216]. This model is hard to constrain with lab experiments because DM does not interact with electrons, and especially for DM lighter than muons (as it is of main interest here), DM can annihilate only into muon and tau neutrinos.

We investigate this scenario, exploring the yet unconstrained parameter space in the energy range of ∼10–100 MeV. Through flavor mixing, ν_e and $\bar{\nu}_e$ have been generated when the neutrinos reach the Earth, which makes it possible for detectors such as Super-Kamiokande (SK) [280] to detect them through charged-current interations. These neutrinos will show a very specific spectral feature; for example, in the simplest model investigated in Ref. [216], DM annihilation will produce a neutrino line at its mass ($\chi\chi \to \nu\bar{\nu}$). The energy range of ∼10–100 MeV, where there are solar, reactor, and atmospheric neutrino backgrounds as well as cosmic ray muons, has been studied well especially for detecting the diffuse supernova neutrino background [281, 282, 283].

We obtain upper limits on the annihilation cross section of this DM in the case that it makes up ∼2% of the total DM, the model that could explain the EDGES result, using the several years of SK data. We also predict the upper limits that could be obtained by future experiments, Hyper-Kamiokande (HK) [284], Deep Underground Neutrino Experiment (DUNE) [285] and Jiangmen Underground Neutrino Observatory (JUNO) [286]. A DM model like this, in which DM only annihilates into neutri-

nos, but making up for the entire amount of DM, has been studied before [287, 288], obtaining upper limits on the cross section using the SK data. We also obtain updated upper limits for this scenario.

This chapter is organised as follows. In Sec. 2, we discuss milli-charged DM and the DM scenario we investigate. In Sec. 3, we determine the neutrino flux coming from the annihilation of this milli-charged DM, while in Sec. 3, we explain the analysis we perform. In Secs. 5 and 5.1, we discuss our results and conclusions respectively.

2 Theory

2.1 Milli-charged DM

There are some requirements for the DM properties that need to hold in order to be responsible for the extensive cooling of the primordial hydrogen gas [216]: Due to the equipartition theorem, the DM particles should be relatively light. Furthermore, models in which the cross section for dark matter scatterings with gas is independent of the velocity can already be ruled out by constraints from observations of the CMB.

To fulfil these requirements, the mediator of the dark matter-baryon interactions should be lighter than the temperature of the gas at $z \sim 17$. New light mediators in the mass range required to explain the EDGES result are ruled out [289, 290], and their contribution to the radiation part of the energy density would exceed the current constraints [106]. When the DM carries a small electric charge, it could couple to the photon. Reference [215] finds that, in order to cool the gas sufficiently, the following condition for the electric charge should be fulfilled:

$$\epsilon \approx 1.7 \times 10^{-4} \left(\frac{m_\chi}{300\,\mathrm{MeV}}\right) \left(\frac{10^{-2}}{f_\chi}\right)^{3/4}, \tag{3.1}$$

where $\epsilon \equiv e_\chi/e$ is the electric charge of the milli-charged DM particle, m_χ is its mass and f_χ is its mass fraction of the total DM. The existence of milli-charged DM is already constrained by multiple experiments and astrophysical data, leaving only a small open window in its possible parameter space, with a mass m_χ of ∼10–80 MeV, and a total DM fraction of $f_\chi \sim 0.003$–0.02 [216].

However, the annihilation of milli-charged DM particles through the exchange of a photon is not sufficient to yield the desired energy density for the particle, $f_{\mathrm{DM}}\Omega_{\mathrm{CDM}}$. Therefore, some additional annihilation needs to take place through a new mediator.

Here we specifically study the case of vector mediator V, while the results for the scalar mediator are essentially the same. Refeference [216] finds that annihilation through the new vector mediator V into standard model fermions is excluded if it couples to all flavors. This leads to the consideration of annihilation into mainly neutrinos. When the new vector V is related to the gauge group $U(1)_{L_\mu - L_\tau}$, only coupling to muons, taus, muon-neutrinos and tau-neutrinos is possible. Since V does not couple to electrons, there are not yet many constraints from experiments. The annihilation cross section to any neutrino flavor for such a model is given by

$$\langle \sigma v \rangle = \frac{g_\nu^2 g_\chi^2 m_\chi^2 \kappa}{2\pi (4m_\chi^2 - m_V^2)^2}, \tag{3.2}$$

where g_ν and g_χ are the gauge coupling constants of the neutrino and DM particle, respectively, and $\kappa = 1$ ($v^2/6$) for fermion (scalar) DM. We put constraints on this model by evaluating the SK data, and make predictions for some future experiments.

Beside this, we also consider DM annihilation into neutrinos in a broader sense. If dark matter only annihilates into neutrinos, this would be harder to detect than the cases where gamma rays are produced. The limits on the annihilation cross section in this case will therefore be the most conservative ones, and therefore interesting to investigate. We update the limits obtained by Ref. [287], calculating the limits both in the case that DM annihilates to all three neutrino flavors, as in the case that it only annihilates into muon and tau neutrinos as discussed above.

3 Neutrino flux from dark matter annihilation

The final flavor ratio on Earth for pure ν_μ and ν_τ channels is 1 : 2 : 2. When Galactic DM annihilates into ν_μ and ν_τ, the expected monochromatic flux of electron (anti-)neutrinos at Earth will therefore be given by

$$\frac{\mathrm{d}\phi}{\mathrm{d}E_\nu} = \frac{\langle \sigma v \rangle}{2} \mathcal{J}_{avg} \frac{R_{sc} \rho_0^2 f_\chi^2}{m_\chi^2} \frac{1}{5} \delta(E_\nu - m_\chi), \tag{3.3}$$

in the case of Majorana DM, where σ is the annihilation cross section, m_χ is the mass of the DM particle, E_ν is the neutrino energy, $\mathcal{J}_{avg}$ is the angular-averaged "J-factor" of the Milky Way, for which we use the canonical value $\mathcal{J}_{avg} = 5$ [291], $R_{sc} = 8.5$ kpc is the scale radius of the Milky Way, and $\rho_0 = 0.3$ GeV cm^{-3} is the DM density at the scale radius. To retrieve the electron (anti-)neutrino flux for Dirac DM, Eq. (3.3) has to be divided by 2.

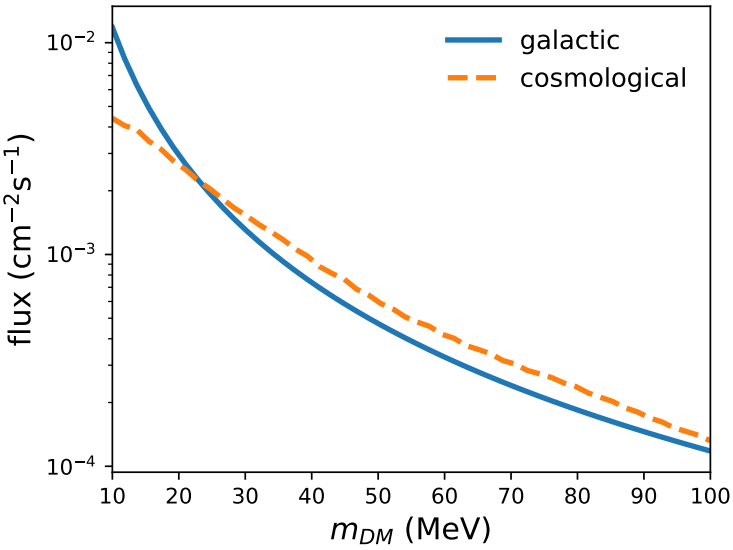

Figure 3.1: The total integrated electron neutrino flux at Earth of both the cosmological and the Galactic contribution as a function of the DM mass, in the case of 2% Dirac DM annihilating into only muon and tau neutrinos.

In the thermal freeze-out scenario, the annihilation cross section at freeze-out required to leave the correct relic abundance of MeV DM is given by

$$\langle \sigma v \rangle = \frac{5 \times 10^{-27} \text{ cm}^3 \text{ s}^{-1}}{\Omega_\chi h^2}, \tag{3.4}$$

for Majorana fermion DM, and is twice as large for Dirac fermion DM for masses below GeV [144]. Since $\Omega_\chi h^2 \approx 0.1 f_\chi$, the targeted annihilation cross section is $\langle \sigma v \rangle \approx 2.5 \times 10^{-24} (f_\chi/0.02)^{-1}$ cm^3 s^{-1} and $5 \times 10^{-24} (f_\chi/0.02)^{-1}$ cm^3 s^{-1} for Majorana and Dirac DM respectively.

Besides the Galactic neutrino flux, we also take into account the contribution to the flux coming from DM annihilations outside our galaxy. We adopt the calculation of Ref. [292] with the most recent model of substructure boost [293]. This cosmological neutrino flux is of the same order of magnitude as the Galactic contribution, but non-monochromatic due to its redshift. In Fig. 3.1, the total integrated flux of both the cosmological and the Galactic contribution are shown as a function of the DM mass.

4 The analysis

We set upper limits on the DM annihilation cross section using the latest SK data [280], and predict the upper limits that could be obtained by the future experiments, Hyper-Kamiokande [284], DUNE [285] and JUNO [286]. We use the SK data from the first three data periods [280], which contains 2853 days of data taking in total, in the energy range of 16–88 MeV, considering 18 bins with a width of 4 MeV. The expected number of events at the detector coming from DM annihilation is calculated through

$$N_{\rm events} = \sigma_{\rm det} \phi N_{\rm target} \epsilon_{\rm det} t, \tag{3.5}$$

where $\sigma_{\rm det}$ is the detection cross section, ϕ is the neutrino flux, $N_{\rm target}$ is the number of target particles in the detector, $\epsilon_{\rm det}$ is the efficiency of the detector which we get from [280], and t is the exposure time. SK is a 22.5 kton water Cherenkov detector [280], detecting neutrinos through the measurement of Cherenkov radiation from relativistic electrons and positrons. The relevant detection channels in our energy range are inverse beta decay ($\bar{\nu}_e + p \to e^+ + n$), and the absorption of ν_e and $\bar{\nu}_e$ by Oxygen in charged current interactions ($\overset{(-)}{\nu}_e + {}^{16}\mathrm{O} \to e^{\pm} + \mathrm{X}$). The energies of electrons and positrons produced by these interactions are $E_e = E_\nu - 1.3$ MeV ($\bar{\nu}_e p$), $E_\nu - 15.4$ MeV ($\nu_e O$), and $E_\nu - 11.4$ MeV ($\bar{\nu}_e O$). The cross sections for these detection channels are taken from Refs. [294, 295]. To correct for the energy resolution of the experiment, we smear the expected electron (positron) spectrum with a Gaussian function, using an energy resolution of width

$$\sigma = 0.40 \text{ MeV} \sqrt{E/\text{MeV}} + 0.03E, \tag{3.6}$$

that we take from Ref. [287]. We perform a χ^2 analysis of the expected number of events compared to the data, and calculate the upper limit at the 90% confidence level. We consider four different backgrounds coming from atmospheric neutrinos, that we also take from Ref. [280]. This background data is taken from the first running phase of SK, SK-I. We rescale it to the entire exposure time that we consider of 2853 days.

The future experiments that we consider show a lot of improvement in several ways. The invisible muon background originating from $\nu_\mu/\bar{\nu}_\mu$ charged current events, which is the biggest background in SK below $\sim$40 MeV, might be significantly decreased in measurements of future water Cherenkov detectors by adding Gadolinium [296]. In our analysis for Hyper-Kamiokande, we assume a reduction of this background by 80%. In the case of JUNO, this background is removed in total through the implementation of an extra system for cosmic muon detection and background reduction [297]. In the case of DUNE, this background is removed (e.g., see [298]). For our

prediction, we consider an exposure time of 3000 days for each detector. We use the same background data as in SK, rescaling it to the right exposure time and the size of the specific experiment. In the case of Hyper-Kamiokande, a 520 kton upgrade of SK [284] with a fiduciul volume of 374 kton, the same energy resolution is used [Eq. (3.6)].

DUNE is a 46.4-kton liquid argon detector [299]. The relevant detection channels are the detection of electron (anti-)neutrinos through charged current interactions ($\nu_e/\bar{\nu}_e + {}^{40}\mathrm{Ar} \to e^-/e^+ + \mathrm{A}' + nN$) [295], where nN are the emitted nuclei and A' is the remaining nucleus. JUNO is a 20-kton lab based liquid scintillator [286]. The detection channels relevant for JUNO are again inverse beta decay ($\bar{\nu}_e + p \to e^+ + n$), and the capture of electron (anti-)neutrinos on ${}^{12}\mathrm{C}$ in charged current interactions ($\bar{\nu}_e + {}^{12}\mathrm{C} \to {}^{12}\mathrm{B} + e^+ /\ \nu_e + {}^{12}\mathrm{C} \to {}^{12}\mathrm{N} + e^-$) [295]. The energy resolutions for both JUNO and DUNE are significant better than the water Cherenkov detectors. For DUNE, the energy resolution is given by [300]

$$\sigma = 0.025\ \mathrm{MeV}\sqrt{E/\mathrm{MeV}} + 0.060E. \tag{3.7}$$

For JUNO, the energy resolution we use is given by [301]

$$\sigma = 0.03\ \mathrm{MeV}\sqrt{E/\mathrm{MeV}}. \tag{3.8}$$

To predict the upper limit at the 90% confidence level, we use the python tool `swordfish` [302, 303] that can, among others, predict upper limits based on Poisson statistics, resulting in approximately the mean value of the results that one would get performing a Monte Carlo simulation. Besides this, in the case of Hyper-Kamiokande, we explicitly perform a Monte Carlo simulation to obtain the full scope of possible values. We furthermore consider the reach of a hypothetical experiment with the size of Hyper-Kamiokande and the specifications of JUNO, which would result in a very strong experiment.

We obtain the upper limits for several cases. Besides the case of a milli-charged Dirac DM particle responsible for 2% of the total DM, annihilating into only muon and tau neutrinos, we also consider the situation where the 100% of DM only annihilates into neutrinos. In this situation we consider two subcases. In the first case, the DM has the same properties as in the 2%-situation. In the second case, we consider Majorana DM, annihilating into all three neutrino flavors. Since in this case the expected flavor ratio at Earth is $1:1:1$, the expected neutrino flux is given by

$$\frac{\mathrm{d}\phi}{\mathrm{d}E_\nu} = \frac{\langle\sigma v\rangle}{2}\mathcal{J}_{avg}\frac{R_{sc}\rho_0^2}{m_\chi^2}\frac{1}{3}\delta(E_\nu - m_\chi). \tag{3.9}$$

The latter case is similar to ordinary WIMP DM, except that the neutrino-only restriction makes it harder to detect. Therefore, the upper limits obtained in this situation will be the most conservative constraints for MeV WIMP DM annihilation.

5 Results

In the top panel of Fig. 3.2, the upper limits are plotted for the case of the 2% milli-charged DM. The black dashed line is the cross section corresponding to the DM model that could explain the EDGES results. The SK limit is not strong enough to rule out the milli-charged DM model. Based on 3000 running days, the predictions show that Hyper-Kamiokande, JUNO and DUNE cannot reach the desired limit as well. However, the actual data will probably induce some fluctuations, possibly resulting in a stronger limit, as can be seen from the behavior of the Monte Carlo region of Hyper-Kamiokande, compared to its predicted line. The strongest limit comes from DUNE. Running the detector long enough might result in strong enough limits to constrain the milli-charged DM model. A combined analysis of the data of the several experiments could result in a stronger limit by up to a factor of 2. In the bottom panel of Fig. 3.2, we show the limits in terms of the coupling constants and the masses of the dark matter particle and the new mediator, $(g_\chi g_f)^2 (m_\chi m_V)^4$, specific to our DM model.

Figure 3.3 shows the SK limits both with and without taking the extragalactic DM annihilation flux into account. We note that the Galactic flux has a substantial contribution to the limit.

We note that the most recent CMB (re)analysis find that the fraction of milli-charged DM might be contrained even more tightly, $f_\chi \lesssim 0.4\%$ [304] (and references therein). In the case of $f_\chi = 0.4\%$, our limits get weaker by a factor of $(2/0.4)^2 = 25$ [Eq. (3.3)]. However, the annihilation cross section required to explain the relic abundance becomes larger by a factor of $2/0.4 = 5$ [see Eq. (3.4) and subsequent sentences]. Hence our limits on the annihilation cross section relative to its canonical value will be weakened by a factor of 5.

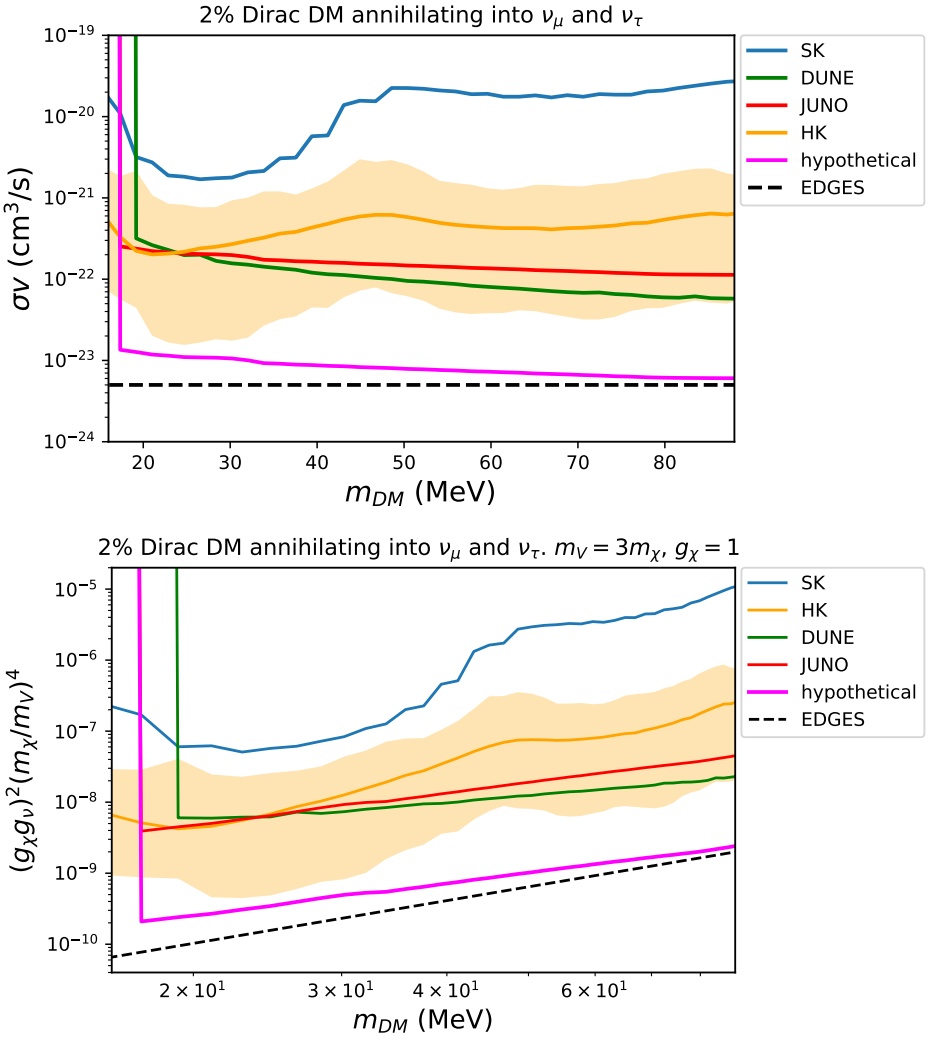

Figure 3.2: Upper limits on the annihilation cross section $\langle \sigma v \rangle$ of milli-charged Dirac DM into only muon and tau neutrinos, making up 2% of the total DM, as a function of the DM mass (upper panel). The lower panel shows the annihilation cross section in terms of the coupling constants, the DM mass, and the mass of the new mediator V. The black dashed line is the cross section induced by the EDGES results, in case of Dirac DM. The blue line comes from the analysis of 2853 days of SK data. The other lines are predictions using Swordfish [302, 303]. The orange band shows the region between the minimum and maximum upper limit values predicted for the Hyper-Kamiokande through a Monte Carlo simulation.

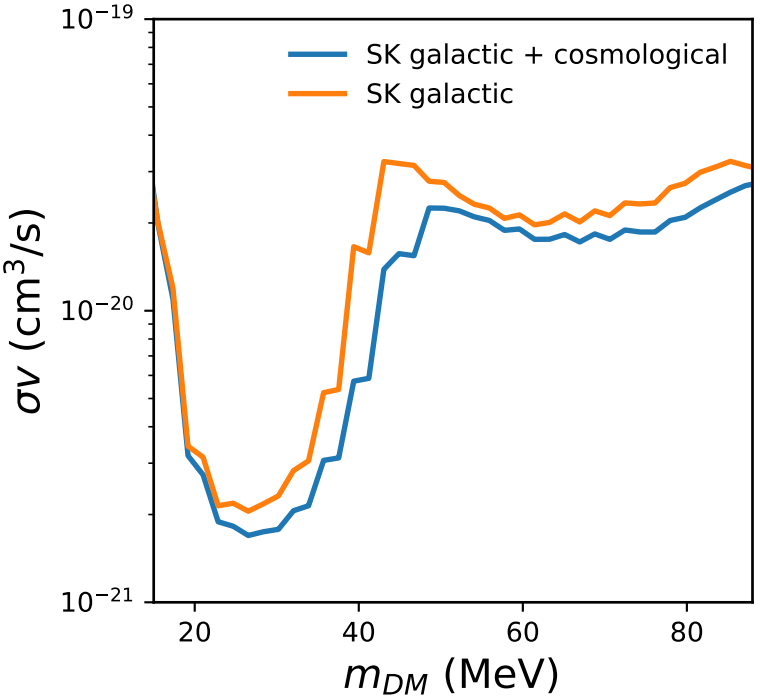

Figure 3.3: Upper limits on the annihilation cross section of milli-charged Dirac DM, making up 2% of the total DM, as a function of the DM mass, computed from the analysis of 2853 days of SK data. The orange line only contains the Galactic contribution to the neutrino flux coming from DM annihilations, while the blue line also includes the extragalactic contribution.

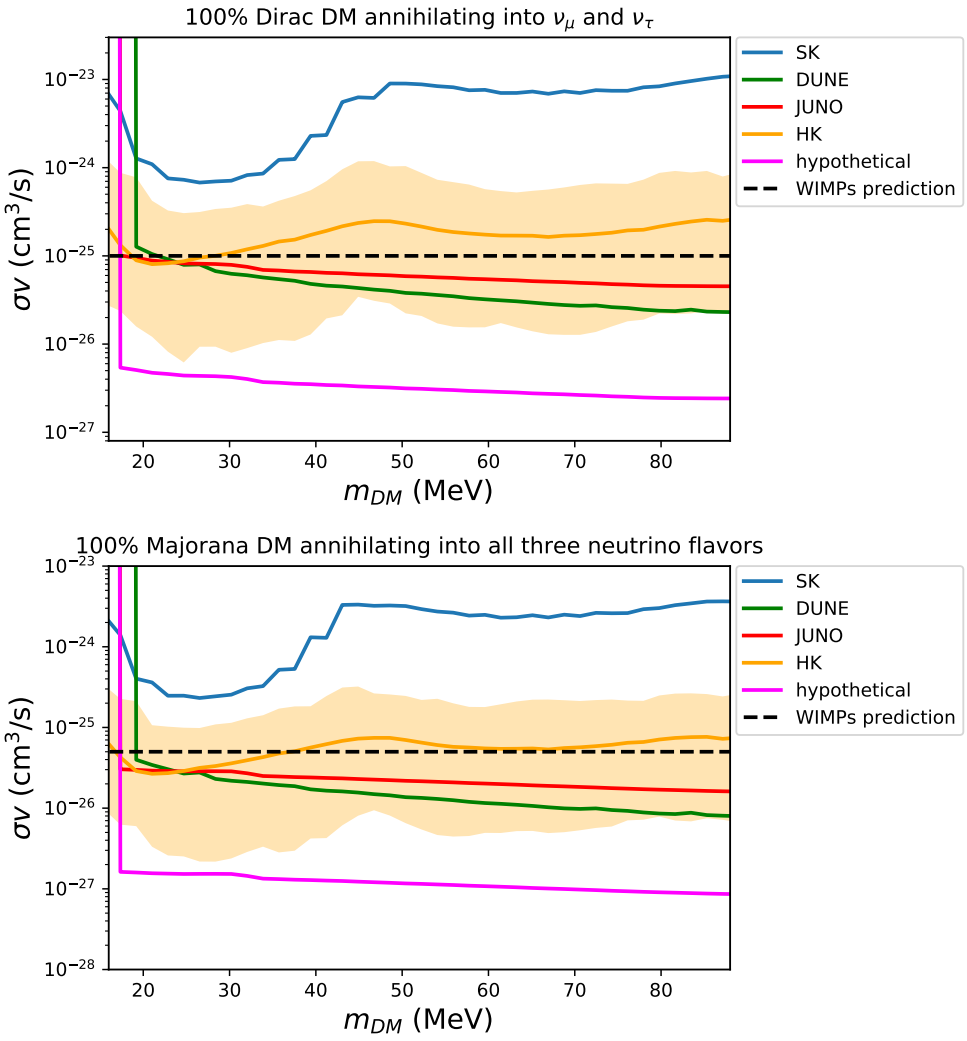

Figure 3.4: Upper limits on the annihilation cross section of milli-charged Majorana DM, being the total 100% of DM, as a function of the DM mass. The upper panel shows the case of Dirac DM annihilating into only muon and tau neutrinos. The lower panel shows the case of Majorana DM annihilating into all three neutrino flavors with equal fraction. The black dashed line is the preferred cross section for WIMPs, in case of Dirac (Majorana) DM in the upper (lower) panel. The blue line comes from the analysis of 2853 days of SK data. The other lines are predictions using Swordfish [302, 303]. The orange band shows the region between the minimum and maximum upper limit values for Hyper-Kamiokande predicted through a Monte Carlo simulation.

Finally, besides exploring the milli-charged DM model, we explore two more generic cases, where 100% of DM annihilates into neutrinos. First, we study the same Dirac DM annihilating into only muon and tau neutrinos, whose results are shown in the top panel of Fig. 3.4. The second case is Majorana DM annihilating into 3 neutrino flavors with equal fraction, shown in the bottom panel of Fig. 3.4. Since neutrinos are harder to detect than gamma rays, this results in a more conservative, and hence most general constraints on the DM annihilation [291]. While the current limit of SK could not yet constrain the WIMP prediction, in both of these cases, Hyper-Kamiokande, JUNO and DUNE will certainly be able to do so. We note that our updated limit is weaker than the limit found in Ref. [287] based on the previous data set of SK [305] by a factor of several.

5.1 Conclusions

The recent results of EDGES suggest that the primordial gas underwent extensive cooling from some additional DM kind. Several constraints on the DM parameter space have already been made. We explore the yet unconstrained region in the case that milli-charged DM makes up for $\sim$2% of the total dark matter, through the scenario in which this DM interacts with the standard model through the $\mu - \tau$ lepton number. This additional interaction is motivated by the thermal freeze-out scenario to explain the correct relic density, and also by the fact that it is largely unconstrained. If this DM has masses of 10–100 MeV as suggested by the EDGES measurement, it annihilates only into muon and tau neutrinos.

By calculating the neutrino flux from the Galactic and extragalactic halos and comparing with existing data, we find that data from Super-Kamiokande are not yet able to constrain this model. We however find that future experiments might be able to detect neutrinos from this particular DM species. The hypothetical experiment that we study with the size comparable to Hyper-Kamiokande and energy resolution comparable to JUNO or DUNE would be able to reach the desired limits. Although such an experiment is not scheduled to be build in the near future, there has been a European-wide initiative to study the possibility of an experiment with a size of the right order of magnitude [306]. We furthermore provide updated limits on the annihilation cross section for more general WIMP DM model in the mass range of 16–88 MeV, using (expected) data from the current and future neutrino experiments. We find that the current data of SK can not yet put constraints on the WIMPs prediction, but the future experiments Hyper-Kamiokande, DUNE and JUNO will be capable of this.

4 Effects of a neutrino–dark energy coupling on oscillations of high-energy neutrinos

The previous two chapters discussed the indirect detection of dark matter, respectively using gamma-rays and neutrinos as our messenger. In this chapter we change to another subject in the dark sector: dark energy. If dark energy is a dynamical field rather than a cosmological constant, an interaction between DE and the neutrino sector could exist, modifying the neutrino oscillation phenomenology, and causing CP and apparent Lorentz violating effects. The terms in the effective Hamiltonian induced by the DE-neutrino coupling do not depend on the neutrino energy, while the ordinary components decrease with $1/E_\nu$. Therefore, the DE-induced effects are absent at lower neutrino energies, but become significant at higher energies, allowing to be searched for by neutrino observatories. In this chapter, we explore the impact of the DE-neutrino coupling on the oscillation probability and the flavor transition in the three-neutrino framework, and investigate the CP-violating and apparent Lorentz violating effects.

The work in this chapter previously appeared in [2].

1 Introduction

Dark Energy is a well established hypothesis in cosmology, being the driving force behind the accelerated expansion of the Universe. It makes up for ∼68% of the total energy density in the current Universe [106]. However, the nature of this presumed DE is still unknown, and several possible explanations are being considered. It could be a cosmological constant, which is a constant-valued energy density through time and space [307, 308]. The other possibility is that it is composed of a scalar field, like

quintessence [309, 310]. In the latter case, DE might be able to undergo interactions with standard model particles, which we can search for in experiments.

For instance, there could exist a coupling between neutrinos and dynamical field DE. Such a coupling gives rise to an effective potential, which engenders an effect on neutrino oscillations that influences the evolution equation in a way that one could compare with the Mikheyev-Smirnov-Wolfenstein effect that occurs when neutrinos propagate through matter [26, 27, 28, 311]. This interaction will change the oscillation probability, and therefore has an impact on the flavor ratios of the neutrinos detected at Earth. The DE-induced part in the Hamiltonian for flavor propagation is independent of the neutrino energy, while the normal vacuum part falls off as $1/E_\nu$. Therefore, the effect becomes more significant for higher neutrino energies, and might be detectable in experiments sensitive to high-energy extraterrestrial neutrinos such as IceCube [312] and KM3NeT [76] and ultrahigh energy neutrinos such as ANITA [313] and Auger [314]. Furthermore, since the expansion of the Universe is going outward in all directions, the preferred frame of this cosmic expansion is orthogonal to surfaces of constant DE density. Therefore, since we as observers are not in the cosmic-microwave-background rest frame, the effect of the DE-neutrino interaction does depend on the propagation direction of the neutrinos. This CPT and Lorentz violating coupling has been studied before in Ref. [315], and in this chapter, we extend this idea to the case of thee-neutrino mixing.

With the IceCube detector fully operating and KM3NeT to follow in the near future, a new window has opened for searches of new physics. A general study of new physics through high-energy neutrinos and their effect on the flavor ratio at Earth is performed in Ref. [316], by introducing effective operators. (See also Refs. [317, 318, 319, 320, 321, 322, 323, 324, 325] for earlier theoretical work.) The DE-neutrino coupling that we study is a model that predicts specific types of terms in the interaction Lagrangian, which engenders such new physics. Other neutrino interactions are investigated in Ref. [326] and Ref. [327], which explore couplings between neutrinos and dark matter, and between neutrinos and the cosmic neutrino background respectively. In Refs. [86, 87] the parameter space for the flavor ratio at Earth is explored, considering several beyond-the-standard-model theories that have an impact at the production, propagation, and detection of astrophysical neutrinos. Recently, the IceCube collaboration performed a search for signals of Lorentz violation in their data of high-energy atmospheric neutrinos [85], and obtained stringent constraints particularly for higher dimensional operators than the ones that we specifically study for DE-neutrino couplings. (See Refs. [328, 329, 330, 331, 332] for earlier constraints.) In addition, since, as we show later, the oscillation length of the DE-induced mix-

ing is much larger than the travel distance of atmospheric neutrinos, the constraints obtained in [85] are not applicable on the DE-neutrino coupling that we study.

In this chapter we study the impact of the possible DE-neutrino coupling on the flavor composition of high-energy extraterrestrial neutrinos and the consequences of this interaction for current and future experiments. We explore the behavior of the probability and the CP violating effects, as well as the effects of the directional dependence. We also determine the sensitivity for experiments to be able to measure those effects.

The chapter is organised as follows. In Sec. 2, we introduce the theory behind the DE-neutrino coupling and derive the DE induced oscillation probability in the framework of three-neutrino mixing. Extra details can be found in the Appendix. In Sec. 3.1, we explore the effects of the coupling on the behavior of the oscillations of high-energy neutrinos and discuss the impact on the flavor composition. We also investigate the CP-violating effects. In Sec. 3.2, we determine the sensitivity to those effects for current and future experiments, and explore the directional effects in Sec. 3.3, followed by conclusions in Sec. 4.

2 Theory

2.1 Dark energy–neutrino interaction

We consider the DE-Neutrino coupling, following the discussion in Ref. [315]. Considering three neutrino flavors, the neutrino fields are described by the Dirac spinor set $\{\nu_e, \nu_\mu, \nu_\tau\}$, and their charge conjugates by the set $\{\nu_{e^c}, \nu_{\mu^c}, \nu_{\tau^c}\}$. The six neutrino fields are combined in the object ν_A, where A runs over the neutrino flavors and their conjugates. The most general Lorentz/CPT-violating form of the equations of motion is then given by [320]

$$(i\gamma^\mu \delta_\mu - M_{AB})\nu_B = 0, \tag{4.1}$$

where

$$M_{AB} \equiv m_{AB} + im_{5AB}\gamma_5 + a^\mu_{AB}\gamma_\mu + b^\mu_{AB}\gamma_5\gamma_\mu + \frac{1}{2}H^{\mu\nu}_{AB}\sigma_{\mu\nu}. \tag{4.2}$$

The four-vectors a^μ, b^μ, and the antisymmetric tensor $H^{\mu\nu}$ in Eq. (4.2) parametrize Lorentz violation. $H^{\mu\nu}$ is only Lorentz violating, while the parameters a^μ and b^μ are CPT violating as well. These parameters are highly restricted in our case where the coupling with DE is responsible for the Lorentz/CPT violation. The expansion of the Universe has an outward direction, thus the unit four-vector that parametrizes

the preferred frame of this cosmic expansion, l^μ, is orthogonal to the surfaces of constant DE density, which is closely aligned with the surfaces of constant CMB temperature [315, 333, 334, 335, 336]. Therefore, $a^\mu \propto l^\mu$ and $b^\mu \propto l^\mu$, where $l^\mu = (1,0,0,0)$ in the rest frame of the CMB. Also, $H^{\mu\nu}$ should be proportional to l^μ, but since it is not possible to create an anti-symmetric tensor from just one four-vector, $H^{\mu\nu}$ has to be zero in the case of our DE-neutrino coupling. Finally, the DE-neutrino coupling can be parametrized solely by the combination of a^μ and b^μ, namely $(a_L)^\mu_{ab} \equiv (a+b)^\mu_{ab}$, where we have $(a_L)^\mu_{ab} \propto l^\mu$ [315, 320]. Because the velocity of our solar system with respect to the CMB restframe is $\sim 10^{-3}$ times the speed of light, we have $(a_L)^\mu p_\mu \propto E(1 - \boldsymbol{v}\cdot\hat{\boldsymbol{p}})$, where $\boldsymbol{v}$ is our velocity with respect to the CMB rest frame and $\hat{\boldsymbol{p}}$ is the neutrino propagation direction.

A simple form of Langrangian that describes an interaction by the DE-neutrino coupling is given by

$$\mathcal{L}_{int} = -\lambda_{\alpha\beta}\frac{\partial_\mu \phi}{M_*}\bar{\nu}_\alpha \gamma^\mu (1-\gamma_5)\nu_\beta, \tag{4.3}$$

where ϕ is a quintessence field, $\lambda_{\alpha\beta}$ is a coupling constant matrix and M_* is the energy scale of the interaction. In this example, we have $a^\mu_L \sim \lambda\dot{\phi}(t) l^\mu / M_*$.[1]

The effective Hamiltonian that describes the propagation of the flavor eigenstates to leading order is given by

$$h_{eff} = \begin{bmatrix} p\delta_{ab} + (\tilde{m}^2)_{ab}/2p + (a_L)^\mu_{ab} p_\mu/p & 0 \\ 0 & p\delta_{ab} + (\tilde{m}^2)^*_{ab}/2p - (a_L)^{*\mu}_{ab} p_\mu/p \end{bmatrix}, \tag{4.4}$$

where the indices a, b run over the flavor eigenstates e, μ, τ. The upper left block describes the neutrino interactions, and the lower right the antineutrinos. Since the effective Hamiltonian is block diagonal, no mixing will take place between neutrinos and antineutrinos, and therefore we consider the two blocks for neutrinos and antineutrinos separately.

The Hamiltonian that describes the neutrino propagation in vacuum in the mass base is given by

$$H_m = \begin{bmatrix} E_1 & 0 & 0 \\ 0 & E_2 & 0 \\ 0 & 0 & E_3 \end{bmatrix}, \tag{4.5}$$

where $E_i = \sqrt{p^2 + m_i^2}$. The Hamiltonian in the flavor basis is then obtained by

[1] This interaction may also give rise to scattering between the neutrinos and DE-induced particles, for which we show that the mean-free path for the neutrinos is much larger than the Hubble length in Appendix 5.2.

rotating the basis as

$$H_f = U H_m U^\dagger, \tag{4.6}$$

where U is the standard Pontecorvo-Maki-Nakagawa-Sakata (PMNS) matrix for three-neutrino mixing [337].

The Hamiltonian that describes the DE-induced mixing in the basis in which it demonstrates itself in diagonal form, is given by

$$V_m = \begin{bmatrix} \pm k_1(1 - \boldsymbol{v}\cdot\hat{\boldsymbol{p}}) & 0 & 0 \\ 0 & \pm k_2(1 - \boldsymbol{v}\cdot\hat{\boldsymbol{p}}) & 0 \\ 0 & 0 & \pm k_3(1 - \boldsymbol{v}\cdot\hat{\boldsymbol{p}}) \end{bmatrix}, \tag{4.7}$$

in which k_i is a constant and the positive (negative) sign is for neutrinos (antineutrinos), and the Hamiltonian in the flavor basis is obtained through

$$V_f = U_{\rm DE} V_m U_{\rm DE}^\dagger, \tag{4.8}$$

where $U_{\rm DE}$ is an independent unitary matrix.

The mixing matrices U and $U_{\rm DE}$ are parameterized as

$$U_{(\rm DE)} = \begin{bmatrix} c_{12}c_{13} & s_{12}c_{13} & s_{13}e^{-i\delta} \\ -s_{12}c_{23} - s_{13}s_{23}c_{12}e^{i\delta} & c_{12}c_{23} - s_{12}s_{23}s_{13}e^{i\delta} & s_{23}c_{13} \\ s_{12}s_{23} - s_{13}c_{12}c_{23}e^{i\delta} & -s_{23}c_{12} - s_{12}s_{13}c_{23}e^{i\delta} & c_{13}c_{23} \end{bmatrix} \begin{bmatrix} 1 & 0 & 0 \\ 0 & e^{i\beta_1} & 0 \\ 0 & 0 & e^{i\beta_2} \end{bmatrix}. \tag{4.9}$$

In the standard PMNS matrix U, $c_{ij} = \cos\theta_{ij}$ and $s_{ij} = \sin\theta_{ij}$, where θ_{ij} are the vacuum mixing angles and δ is the CP-violating phase. For the values of the vacuum parameters, we use the best fit values from the Particle Data Group [338]. The equivalent mixing matrix for the DE-induced interaction is given by $U_{\rm DE}$, where $c_{ij_{\rm DE}} = \cos\theta_{ij_{\rm DE}}$ and $s_{ij_{\rm DE}} = \sin\theta_{ij_{\rm DE}}$, with $\theta_{ij_{\rm DE}}$ and $\delta_{\rm DE}$ the extra DE-induced mixing angles and CP-violating phase. The matrix on the right contains the two independent Majorana phases, relevant in the case of Majorana neutrinos. However, the oscillation probability does not depend on the Majorana phases, and therefore (DE induced) neutrino oscillations are not sensitive to these (DE induced) phases.

2.2 Oscillation probabilities

The Schrödinger equation in the flavor basis is given by

$$i\frac{\mathrm{d}}{\mathrm{d}t}\psi_f(t) = \mathscr{H}_f \psi_f(t), \tag{4.10}$$

where

$$\mathscr{H}_f = U H_m U^\dagger + U_{\rm DE} V_m U_{\rm DE}^\dagger. \tag{4.11}$$

The solution of the Schrödinger equation in Eq. (4.10) is

$$\psi_f(t) = e^{-i\mathscr{H}_f t}\psi_f(0). \tag{4.12}$$

In order to calculate $U_f(L) \equiv e^{-i\mathscr{H}_f L}$, where we replaced t with the oscillation distance L, we follow Ref. [339]. A more detailed derivation is summarised in Appendix 5.1.

The amplitude of the transition from ν_α to ν_β is

$$A_{\alpha\beta} \equiv \langle\beta|U_f(L)|\alpha\rangle = \phi\sum_{a=1}^{3} e^{-iL\lambda_a} M_{a\alpha\beta}, \tag{4.13}$$

where $\phi \equiv e^{-iL\mathrm{tr}\mathscr{H}_f/3}$, λ_a are the eigenvalues of the traceless part of the Hamiltonian $\mathscr{H}_f$, $T \equiv \mathscr{H}_f - (\mathrm{tr}\mathscr{H}_f)I/3$ and $M_{a\alpha\beta}$ is defined as

$$M_{a\alpha\beta} \equiv \frac{(\lambda_a^2 + c_1)\delta_{\alpha\beta} + \lambda_a T_{\alpha\beta} + (T^2)_{\alpha\beta}}{3\lambda_a^2 + c_1}, \tag{4.14}$$

where $c_1 = T_{11}T_{22} - T_{12}T_{21} + T_{11}T_{33} - T_{13}T_{31} + T_{22}T_{33} - T_{23}T_{32}$. We can calculate the oscillation probability with

$$P_{\alpha\to\beta} \equiv |A_{\alpha\beta}|^2. \tag{4.15}$$

Since T is Hermitian ($T^\dagger = T$), the three eigenvalues λ_a are all real. We now define

$$\begin{aligned} c_a &= \cos(L\lambda_a), && (4.16)\\ s_a &= \sin(L\lambda_a), && (4.17)\\ \mathcal{R}_{a\alpha\beta} &= \mathrm{Re}[M_{a\alpha\beta}], && (4.18)\\ \mathcal{I}_{a\alpha\beta} &= \mathrm{Im}[M_{a\alpha\beta}], && (4.19) \end{aligned}$$

and rewrite the oscillation probability as

$$\begin{aligned} P_{\alpha\beta} = \sum_{ab} \big[&(c_a c_b + s_a s_b)(\mathcal{R}_{a\alpha\beta}\mathcal{R}_{b\alpha\beta} + \mathcal{I}_{a\alpha\beta}\mathcal{I}_{b\alpha\beta}) \\ &+ (s_a c_b - s_b c_a)(\mathcal{R}_{b\alpha\beta}\mathcal{I}_{a\alpha\beta} - R_{a\alpha\beta}\mathcal{I}_{b\alpha\beta})\big]. \end{aligned} \tag{4.20}$$

We further use

$$\begin{aligned} c_a c_b + s_a s_b &= 1 - 2\sin^2 x_{ab} && (4.21)\\ s_a c_b - s_b c_a &= 2\sin x_{ab}\cos x_{ab}, && (4.22) \end{aligned}$$

where $x_{ab} = (\lambda_a - \lambda_b)L/2$, and arrive at

$$\begin{aligned} P_{\alpha\beta} = \delta_{\alpha\beta} - 4\sum_a \sum_{b<a} \left[(\mathcal{R}_{a\alpha\beta}\mathcal{R}_{b\alpha\beta} + \mathcal{I}_{a\alpha\beta}\mathcal{I}_{b\alpha\beta}) \sin^2 x_{ab} \right] \\ + 2\sum_a \sum_{b<a} \left[(\mathcal{R}_{b\alpha\beta}\mathcal{I}_{a\alpha\beta} - R_{a\alpha\beta}\mathcal{I}_{b\alpha\beta}) \sin 2x_{ab} \right] . \end{aligned} \tag{4.23}$$

Here in obtaining the first term, we used the fact that $P_{\alpha\beta} = \delta_{\alpha\beta}$ at $L = 0$.

Rather than on the individual parameters k_i that show up in the Hamiltonian of Eq. (4.7), the probability will depend on the differences $k_j - k_i$, which we call the effective mass parameter, $m_{\text{eff}_{ji}} \equiv k_j - k_i$. Since we consider the three-flavor case, two of them are independent: $m_{\text{eff}_{21}} \equiv k_2 - k_1$ and $m_{\text{eff}_{31}} \equiv k_3 - k_1$. When both independent effective mass parameters equal to zero, Eq. (4.23) returns the vacuum oscillation probability.

For distances much larger than the oscillation length, we may replace $\sin^2 x_{ab} \to 1/2$ and $\sin 2x_{ab} \to 0$, while for distances much shorter than the oscillation length, it is not possible to observe effects induced by the DE-neutrino coupling. For example, if the effective mass parameter has a value of $m_{\text{eff}} = 10^{-23}$ GeV, the oscillation length is approximately $L_{\text{osc}} \sim 10^{14}$ km. Since in our case, we are interested in astrophysical neutrinos, the probability that we use reduces to

$$P_{\alpha\beta} = \delta_{\alpha\beta} - 2\sum_a \sum_{b<a} \left[(\mathcal{R}_{a\alpha\beta}\mathcal{R}_{b\alpha\beta} + \mathcal{I}_{a\alpha\beta}\mathcal{I}_{b\alpha\beta}) \right] . \tag{4.24}$$

This is justified especially for sources at cosmological distances, $L \sim H_0^{-1}$, which is equivalent to assuming $m_{\text{eff}} \gg H_0 \approx 10^{-42}$ GeV. In the next section, we shall see that this is indeed the case for the values of m_{eff} that we consider.

As can be seen from the DE-induced Hamiltonian in Eq. (4.8), the DE-induced part of the probability has different sign for neutrinos and anti-neutrinos; i.e., CP is violated. It also does not depend on the neutrino energy, while the vacuum probability falls off over E_ν. Therefore, the impact of DE on neutrino oscillations will become more significant for higher neutrino energies, and thus the effect could be explored through experiments such as IceCube and KM3NeT.

Finally, the DE-induced part is frame dependent. It depends on our velocity with respect to the CMB rest frame, and the propagation direction of the incoming neutrino.

To summarize, the probability will depend on three new mixing angles, one extra CP-violating phase, and two independent effective mass parameters. We will investigate the impact of the DE-neutrino coupling on neutrino oscillations and explore how the

probability behaves for different values of the new mixing parameters in the next section. Throughout this chapter, we assume normal mass hierarchy.

3 Results

3.1 Behavior of the probability

To explore the effect of the DE-neutrino coupling on what we detect here at Earth, we determined the possible final flavor compositions at the time of detection in the presence of this coupling. The result can be seen in Fig. 4.1. We varied all the values of the new mixing parameters, and determined the final flavor composition for several starting flavor ratios at the source. The expected composition for vacuum oscillation is also included, for which the mixing parameters are fixed at the best-fit values of the Particle Data Group [338].

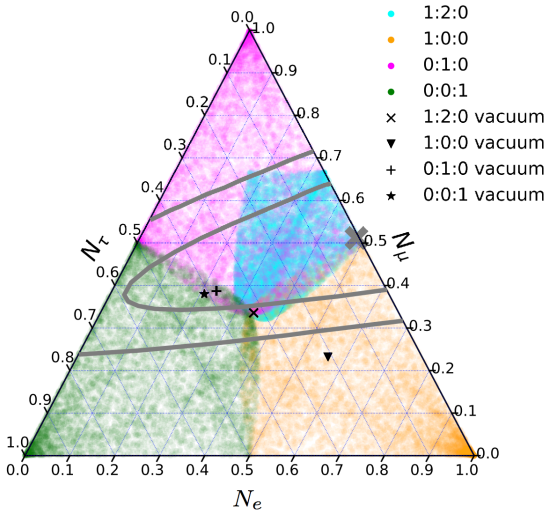

Figure 4.1: The possible ratios of ν_e:ν_μ:ν_τ at Earth for different starting flavor ratios ν_e:ν_μ:ν_τ at the source. The colored regions correspond to oscillation in the presence of DE-induced mixing, where we varied over all combinations of the values of the new mixing angles. The expected ratios for vacuum mixing (assuming normal hierarchy) are drawn in black. The solid grey contours show the allowed regions by IceCube at 68% and 95% confidence levels, while the grey cross represents their best-fit flavor ratio [340].

As can be seen, the part of the composition-triangle that could be reached at Earth, depends on the flavor composition at the source. The cyan colored area corresponds to the source composition 1:2:0 for the flavors e:μ:τ, which is the characteristic flavor composition from pion decays. This is the main channel in which astrophysical neutrinos are expected to be produced. In the case that there is no new physics, the expected flavor composition measured at detection is approximately 1:1:1 as shown as the "cross" symbol.

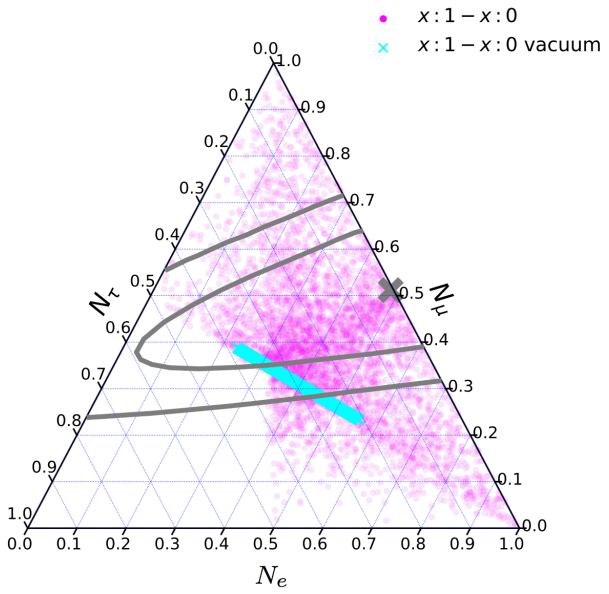

Figure 4.2: The possible ratios of ν_e:ν_μ:ν_τ at Earth for different proportions of ν_e and ν_μ at the source, and no ν_τ at production. The magenta region corresponds to oscillation in the presence of DE-induced mixing, where all combinations of the values of the new mixing angles are varied. The cyan region corresponds to vacuum oscillation. The solid grey contours show the allowed regions by IceCube at 68% and 95% confidence levels, while the grey cross represents their best-fit flavor ratio [340].

Starting from a purely single flavor state, the possible area after these DE-neutrino interactions can occupy only one-third of the entire triangle. No astrophysical process is known to produce τ neutrinos. In Fig. 4.2, the possible flavor compositions are shown for all flavor compositions at the source consisting of a combination of ν_e and ν_μ. The cyan colored region corresponds to the case that there is no new physics. If the observed flavor composition lies outside the cyan region, then it is not compatible with normal oscillation, and regarded as an indication of new physics. If the ratio

lies in the magenta region, this could be due to the DE-neutrino coupling. The lower left part of the triangle cannot be reached by conventional astrophysical neutrinos even with an effect of the DE-neutrino coupling we study. Therefore, it requires both ν_τ production at the source and non-standard neutrino oscillation such as the DE-neutrino interaction (Fig. 4.1).

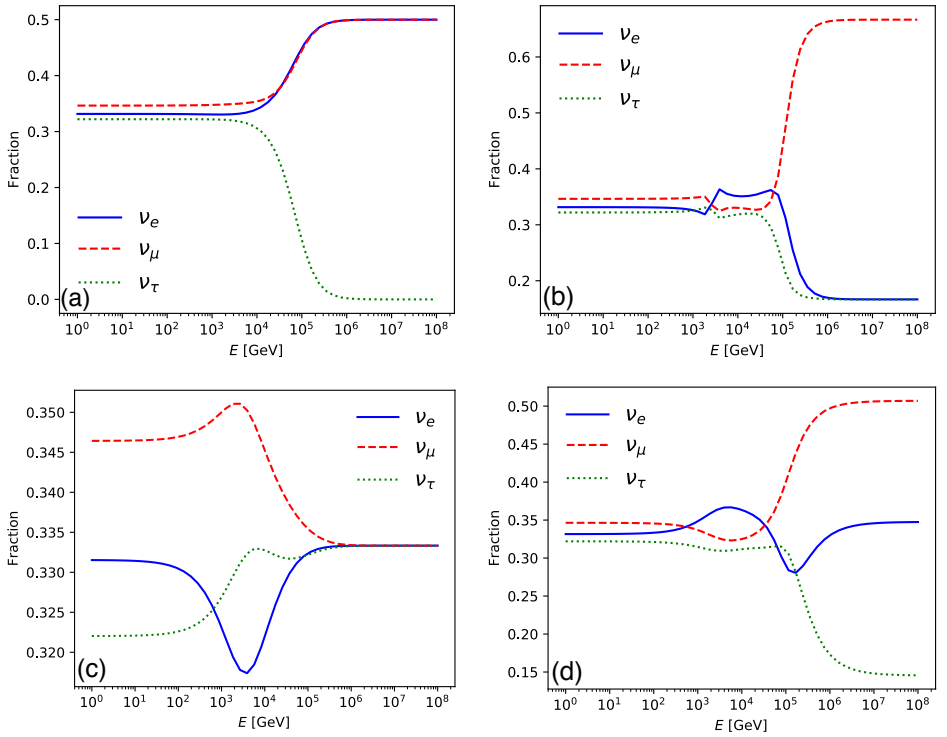

Figure 4.3: The flavor ratios as a function of neutrino energy for different sets of parameter values. The flavor composition at the source is set to 1:2:0. The effective mass parameters are set to $m_{\text{eff}_{21}} = \frac{1}{2} m_{\text{eff}_{31}} = 10^{-26}$GeV, and $\delta_{\text{CP}} = 0$. The values of the new mixing angles are set to (a) $\theta_{12} = 0.25\pi$ and $\theta_{13}, \theta_{23} = 0$; (b) $\theta_{13} = 0.25\pi$ and $\theta_{12}, \theta_{23} = 0$; (c) $\theta_{23} = 0.25\pi$ and $\theta_{12}, \theta_{13} = 0$ (bottom left); and (d) $\theta_{12}, \theta_{13}, \theta_{23} = 0.25\pi$ (maximal mixing). The transition from the domination of vacuum oscillation to DE-induced domination takes place at $E_\nu m_{\text{eff}} \sim 10^{-20}$ GeV^2.

In Fig. 4.3, we explore the behavior of the probability as a function of energy. In these plots, the flavor composition at the source is set to 1:2:0, and the values of the two independent effective mass parameters are set to $m_{\text{eff}_{21}} = m_{\text{eff}_{31}}/2 = 10^{-26}$ GeV. We set the new CP-violating phase equal to zero, and consider the cases that $\theta_{\text{DE}_{12}} =$

0.25π, $\theta_{\mathrm{DE}_{13}}, \theta_{\mathrm{DE}_{23}} = 0$ (Fig. 4.3a), $\theta_{\mathrm{DE}_{13}} = 0.25\pi$, $\theta_{\mathrm{DE}_{12}}, \theta_{\mathrm{DE}_{23}} = 0$ (Fig. 4.3b), $\theta_{\mathrm{DE}_{23}} = 0.25\pi$, $\theta_{\mathrm{DE}_{12}}, \theta_{\mathrm{DE}_{13}} = 0$ (Fig. 4.3c) and $\theta_{\mathrm{DE}_{12}} = \theta_{\mathrm{DE}_{13}} = \theta_{\mathrm{DE}_{23}} = 0.25\pi$ (maximal mixing, Fig. 4.3d). As visible from the plots, for lower energies, vacuum oscillation is still dominant. After a transition phase, that happens around $E_\nu m_{\mathrm{eff}} \sim 10^{-20}$ GeV^2, the mixing caused by the DE-neutrino coupling dominates.

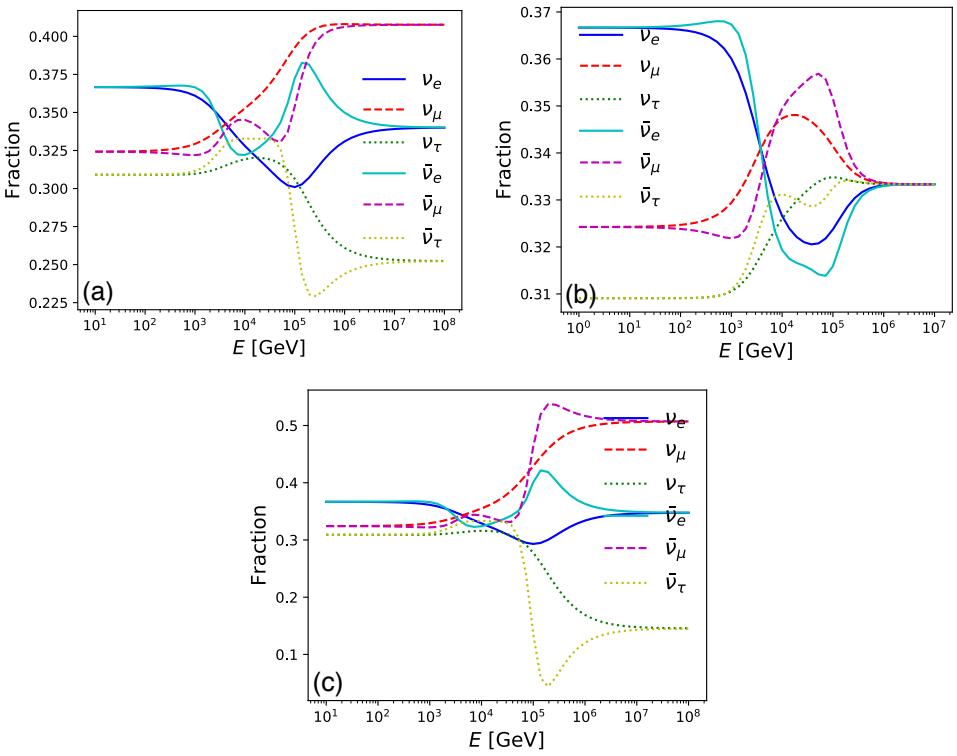

Figure 4.4: The flavor ratios as a function of neutrino energy for different values of δ_{DE}, for both neutrinos and anti-neutrinos. The values of the new mixing parameters are set to $\theta_{12}, \theta_{13}, \theta_{23} = 0.25\pi$, $m_{\mathrm{eff}_{21}} = \frac{1}{2} m_{\mathrm{eff}_{31}} = 10^{-26}$GeV and the starting flavor ratio is set to 1:2:0. The usual CP-violating phase δ_{DE} is set to zero. The new DE-induced CP-violating phase is set to (a) 0.25π, (b) 0.5π, and (c) 0. The effect in (c) comes solely from the sign difference of m_{eff} in the oscillation probability for neutrinos and anti-neutrinos.

We also explore the CP-violating effect of the DE-neutrino coupling. Figure 4.4 shows that neutrinos mix differently from antineutrinos. In Fig. 4.4a, all new mixing angles are set to maximal, 0.25π, and the new CP-violating phase is also set to maximal.

The CP-violating effect is visible over a wide energy range. Although IceCube and KM3NeT cannot distinguish between neutrinos and anti-neutrinos in general, they can recognize $\bar{\nu}_e$ through the Glashow resonance [341] by the measurement of the W^--boson produced on-shell ($\bar{\nu}_e e^- \to W^-$). Thus, if the Glashow resonance-energy of 6.3 PeV lies in the energy range of the CP-violating effect, it would be possible to distinguish electron neutrinos from electron antineutrinos at this energy, and therefore to detect the CP-violating effect. In Figs. 4.4b and 4.4c, the new CP-violating phase is fixed to $\delta_{cp} = 0.5$ and $\delta_{cp} = 0$, respectively. The case that $\delta_{cp} = 0$ in Fig. 4.4c is interesting, because the CP-violation is not induced by the new CP-violating phase, but is entirely due to the sign difference between neutrinos and anti-neutrinos in the Hamiltonian in Eq. (4.7). In the case of Fig. 4.4b, it is interesting to note that the flavor composition at earth changes from approximately 1:1:1, to exactly 1:1:1. This is also the case in Fig. 4.3c.

3.2 Sensitivity

Fig. 4.1 shows that all the possible final flavor compositions from the initial flavor ratio of 1:2:0 are still allowed in light of the IceCube constraints [340]. To this end, we also investigated the sensitivity for experiments to be able to detect the effects from the DE-neutrino coupling. For this, we compare the total amount of muon neutrinos with the null hypothesis that no new physics is detected. We calculate this for the case that $\theta_{13_{\rm DE}}, \theta_{23_{\rm DE}} = 0$, corresponding to the case explored in Fig. 4.3a. We set limits on the parameter space for the effective mass parameter $m_{\rm eff}$ and the mixing angle $\theta_{12_{\rm DE}}$. If a number of $N_\nu^{\rm tot}$ neutrino events is detected at the experiment, assuming a flavor ratio of 1:2:0 at the source, the number of ν_μ we expect to measure is given by

$$\begin{aligned} N_{\nu_\mu} &= \frac{N_\nu^{\rm tot} E_{\rm min}}{3} \int_{E_{\rm min}}^{E_{\rm max}} E^{-2} P_{e\mu} {\rm d}E \\ &\quad + \frac{2 N_\nu^{\rm tot} E_{\rm min}}{3} \int_{E_{\rm min}}^{E_{\rm max}} E^{-2} P_{\mu\mu} {\rm d}E. \end{aligned} \tag{4.25}$$

Here we assume that the neutrino energy spectrum multiplied by the effective area roughly scales as E^{-2}. In case that no new physics is detected, the expected number of muon neutrinos is $N_{\nu_\mu} = N_\nu^{\rm tot}/3$. To obtain the limits on $m_{\rm eff}$ and $\theta_{12_{\rm DE}}$ with 95% confidence level, we solve

$$N_{\nu_\mu} < \frac{N_\nu^{\rm tot}}{3} + 2\sqrt{\frac{N_\nu^{\rm tot}}{3}} \tag{4.26}$$

for $m_{\rm eff}$ and $\theta_{12_{\rm DE}}$, where we choose $m_{\rm eff_{31}} = 2 m_{\rm eff_{21}}$. In Fig. 4.5a, we show the sensitivity to probe for the value of $m_{\rm eff}$ for experiments measuring neutrino events in

the energy range from 100 TeV to 10 PeV — which holds for, for example, IceCube and KM3NeT — in case that they measure 100, 1000 and 10000 neutrino events, as a function of the mixing angle $\theta_{12_{\rm DE}}$. Given that IceCube already has found tens of neutrino events above ∼10 TeV [342, 343], proper analysis will enable to exclude $m_{\rm eff} \lesssim 10^{-27}$ GeV in the near future. In Fig. 4.5b, we show the same for (future) experiments sensitive to ultrahigh-energy (UHE) neutrinos, capable of detecting neutrinos in the energy range between 100 PeV and 10 EeV. Values of $m_{\rm eff}$ and the corresponding values of $\theta_{12_{\rm DE}}$ that lie above the coloured curves would result in an atypical increase of the amount of ν_μ at the detector. In a similar way, this could be calculated for ν_e and ν_τ.

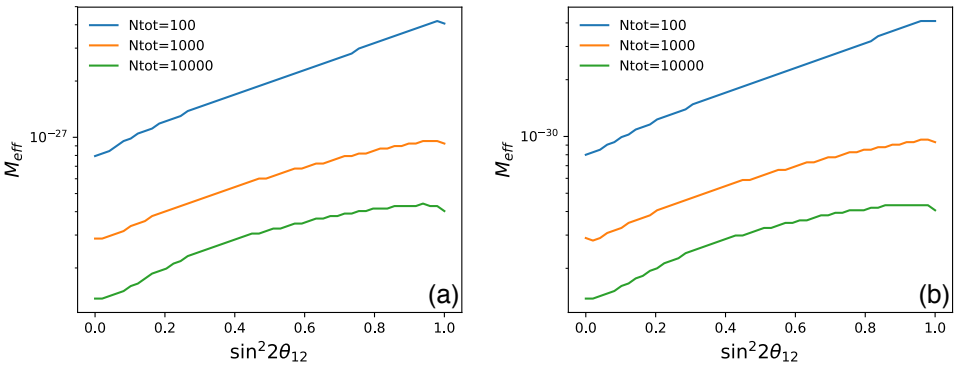

Figure 4.5: The sensitivity for neutrino experiments capable of distinguishing muon neutrinos to probe for the value of $m_{\rm eff}$, in case of a detection of 100, 1000 and 10000 events, for different neutrino energy ranges: (a) 0.1–100 PeV and (b) 0.1–100 EeV. When the genuine values of the parameters $m_{\rm eff}$ and θ_{12} lie above the colored lines, more ν_μ than compatible with standard physics will be detected. In this example, the new mixing angles are set to $\theta_{13}, \theta_{23} = 0$. The flavor composition at the source is set to 1:2:0.

Looking back at the toy model for a possible Lagrangian of the DE-neutrino coupling could look like in Eq. (4.3), we follow Ref. [315] to explore the mass scale of the interaction corresponding to a certain value of the effective mass parameter $m_{\rm eff}$. We have $a_L^\mu \sim \lambda\dot{\phi}(t)l^\mu/M_*$ and $m_{eff} \sim \Delta\lambda\dot{\phi}(t)/M_*$, with $\Delta\lambda$ the difference between the eigenvalues of $\lambda_{\alpha\beta}$. For quintessence we assume $\dot{\phi} \sim M_{\rm Pl}H_0(1+w)^{1/2}$ [310, 315], where $M_{\rm Pl}$ is the Planck mass. The energy scale of the interaction is therefore given

by

$$M_* \simeq 10^6(\Delta\lambda)\left(\frac{1+w}{0.01}\right)^{1/2}\left(\frac{10^{-30}\text{GeV}}{m_{\text{eff}}}\right)\text{GeV}. \tag{4.27}$$

Therefore, the experiments corresponding to Fig. 4.5a and Fig. 4.5b probe up to mass scales of $M_* \sim 10^5$ GeV and $M_* \sim 10^8$ GeV respectively.

3.3 Directional dependence

There are multiple new physics hypotheses that could result in a flavor composition that is not compatible with normal physics (see, e.g., Refs. [316, 86, 87]), and the DE-neutrino coupling is just one of the possibilities. However, the directional dependence of the DE-neutrino coupling is very specific to this model. The DE-induced part of the probability is proportional to $(1 - \boldsymbol{v}\cdot\hat{\boldsymbol{p}})$, and therefore results in a different mixing probability for identical neutrinos with different propagation directions. Since our velocity with respect to the CMB rest frame is $\sim 10^{-3}c$, the effects of the directional component will be small compared to the general effects of the DE-neutrino coupling. To calculate the directional effect, we follow Ref. [315] with some modifications to set our coordinate system. The origin is set at the south pole of the Earth, with the z-axis aligned along the rotational axis of the Earth, such that the north pole lies on the positive axis. The x-axis is set along the direction to the Sun at spring equinox, while the y-axis is set along this direction at summer solstice. The seasonal rotation can be expressed by the azimuthal angle ϕ_s, where $\phi_s = 0$ and $\phi_s = \pi$ for spring and autumn equinox respectively. Since the velocity of the Sun with respect to the CMB rest frame is $v_\odot = 369$ km s^{-1} in the direction $\alpha = 168^\circ$, $\delta = -7.22^\circ$, where α and δ are right ascension and declination respectively, in our coordinate system this velocity is $\boldsymbol{v}_\odot = v_\odot(\cos\delta\cos\alpha, \cos\delta\sin\alpha, \sin\delta) = (-385, 76.1, -46.4)$ km s^{-1}. Because the Earth moves around the Sun with an average orbital speed of $v_\oplus = 29.8$ km s^{-1}, the velocity of the Earth with respect to the CMB rest frame is

$$\begin{aligned}\boldsymbol{v}_\oplus &= \boldsymbol{v}_\odot + v_\oplus\begin{pmatrix}\sin\phi_s\\ -\cos\phi_s\cos\theta_{\text{inc}}\\ -\cos\phi_s\sin\theta_{\text{inc}}\end{pmatrix}\\ &= \begin{pmatrix}-358 + 29.8\sin\phi_s\\ 76.1 - 27.3\cos\phi_s\\ -46.4 - 11.9\cos\phi_s\end{pmatrix}\text{km s}^{-1},\end{aligned} \tag{4.28}$$

where θ_{inc} is the inclination between the x-y plane and the orbital plane around the Sun. In our coordinate frame, the south pole is set to $(0, 0, 0)$. The propagation

direction of the incoming neutrino is therefore described by the unit vector

$$\hat{\boldsymbol{p}} = \begin{pmatrix} \cos\theta_\nu \cos\phi_\nu \\ \sin\theta_\nu \cos\phi_\nu \\ \sin\phi_\nu \end{pmatrix}, \tag{4.29}$$

where ϕ_ν and θ_ν are the polar and azimuthal angle of the incoming neutrino at the south pole respectively. Since the source lies outside Earth, the propagation direction of the neutrino path with respect to the CMB background does not depend on the rotation of the Earth, although it would in the case of an Earth-based neutrino beam. The mixing probability has terms that are proportional to $(1 - \boldsymbol{v}\cdot\hat{\boldsymbol{p}})^2$, $(1 - \boldsymbol{v}\cdot\hat{\boldsymbol{p}})$ and terms that are not dependent on $(1 - \boldsymbol{v}\cdot\hat{\boldsymbol{p}})$ at all. We expect the effect to be larger when the terms $\propto (1 - \boldsymbol{v}\cdot\hat{\boldsymbol{p}})$ dominate, which is the case in the transition phase.

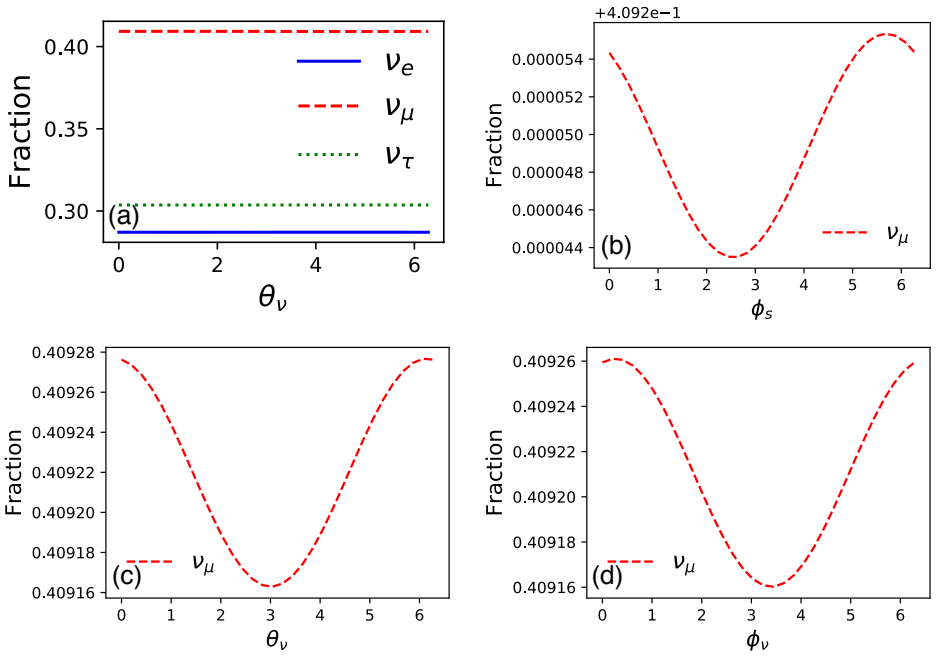

Figure 4.6: The effect of the directional dependence on the flavor composition as a function of incoming azimuthal angle (a, c), polar angle (d) and the angle corresponding to the seasonal position of Earth (b). The DE-induced parameters are set to $\theta_{12}, \theta_{13}, \theta_{23} = 0.25\pi$ and $m_{\text{eff}_{21}} = \frac{1}{2} m_{\text{eff}_{31}} = 10^{-26}$GeV, and the flavor composition at the source is set to 1:2:0. The results are shown for a neutrino energy of $E_\nu = 10^5$ GeV, which lies inside the transition range from vacuum domination towards DE-induced domination. For energies outside the transition phase, the effect is an order of magnitude smaller.

In Fig. 4.6, the effect on the final flavor composition as a function of the different variable angles is shown. In Fig. 4.6a, it is seen that the effect is much smaller than the effects of the other new parameters explored earlier in this chapter. We have to zoom in on one particular flavor to be able to visualize the effect. In Fig. 4.6b, the fraction of ν_μ is plotted as a function of the seasonal shift ϕ_s. The effect is extremely small, with a maximal change of $\sim$0.002% depending on the season in which the neutrinos are detected. Clearly, at this moment, it is far beyond our current abilities to measure such small differences. The advantage of the seasonal shift is that, in the case that a source produces neutrinos on a regular basis such as blazars, the flavor ratio of neutrinos originating from that source could be evaluated in different seasons to search for a seasonal effect. The effect of the propagation direction of the neutrinos is slightly larger than the seasonal effect, as can be seen from Figs. 4.6c and 4.6d, in which the fraction of μ_ν is plotted as a function of the incoming directions θ_ν and ϕ_ν respectively. The maximal change between the flavor fractions depending on the incoming direction is $\sim 0.03\%$. Although this effect is an order of magnitude larger than the effect of the seasonal shift, it is still outside our observational reach to detect such small effects. However, eventually future experiments might become more sensitive, and meanwhile in the years or decades to come, data are being collected, contributing to better statistics. In the case that new physics with the effects described in Sec. 3.1 is found, the directional effect would be the evidence for a DE-neutrino coupling rather than some other solution. It would be also evidence for a non-cosmological constant type of DE.

4 Conclusion

We are only at the beginning stage of collecting data from high energy neutrinos, and exciting times lie ahead. It will not take long before IceCube and KM3NeT will determine if the measured flavor ratio at Earth is compatible with normal physics. We explore a possible origin for new physics results in neutrino telescopes and how this would establish in measurements here on Earth.

The physics we investigate is a possible coupling between dark energy and neutrinos, which engenders an additional source for neutrino mixing. Such a coupling might exist in the case that DE is a dynamical field rather than a cosmological constant. We study the impact on neutrino oscillations in the three-neutrino framework and find that this could result in significant observable effects on Earth. The part of the oscillation probability that is induced by DE is independent of energy in the propagation Hamiltonian, has different sign for neutrinos and anti-neutrinos, and contains a

directional component. Furthermore, the probability depends on three extra mixing angles, one new CP-violating phase, and two independent mass parameters m_{eff}. Because of the energy independency of the DE induced part of the Hamiltonian, while the vacuum oscillation term is proportional to $\propto \frac{\Delta m^2}{2E}$, the effect of the DE-neutrino coupling becomes larger for higher neutrino energies. Below are our main findings.

1. The transition from the energy scale in which vacuum oscillation dominates, to the energy scale where the DE-induced mixing dominates, happens around $E_\nu m_{\text{eff}} \sim 10^{-20}$ GeV^2.

2. We explored the effect of the coupling on the flavor composition of astrophysical neutrinos that we would measure on Earth. Depending on the flavor composition at the source and the values of the new mixing parameters, the possible final flavor ratios cover the entire flavor composition triangle, while vacuum oscillation covers only a limited area. If no tau-neutrinos are produced in astrophysical sources, however, part of the flavor composition triangle cannot be reached even through mixing induced by DE.

3. We also explored the effect on the flavor composition due to the sign difference in the probability between the neutrinos and anti-neutrinos and the new CP-violating phase. Neutrinos and antineutrinos behave differently over a wide energy range, which might be possible to detect if the effective mass parameter m_{eff} happens to have a value between $\sim 10^{-29}$ and $\sim 10^{-25}$ GeV. In that case, the energy range showing CP-violation covers the Glashow resonance of 6.3 PeV, which enables experiments like IceCube and KM3NeT to distinguish between ν_e and $\bar{\nu}_e$.

4. We also determined the sensitivity for current and future experiments to probe the value of the effective mass parameters m_{eff}. We find that current experiments are able to measure anomalous effects due to the DE-neutrino coupling, and can probe the values of the new mixing parameters, for a genuine value of the effective mass parameter down to $m_{\text{eff}} \sim 10^{-27}$, depending on the number of detected neutrino events. Experiments capable of detecting ultrahigh-energy neutrinos could probe further down to $m_{\text{eff}} \sim 10^{-30}$.

5. Because the cosmic expansion has a preferred frame, namely the rest frame of the CMB, the value of m_{eff} does depend on our velocity with respect to the CMB rest frame, and gets slightly altered for different propagation directions of the incoming neutrinos (directional dependence), as well as the position of the Earth with respect to the Sun (the seasonal dependence). These effects are small, resulting only in differences between the flavor composition on a sub-

percentage level, but of big importance in the case new physics is found, since this effect is an unique feature of the DE-neutrino coupling.

5 Appendix

5.1 The amplitude of the flavor transition

The exponential of an $N \times N$ matrix M can be expressed as

$$a_0 I + a_1 M + ... + a_{N-1} M^{N-1}. \tag{4.30}$$

The matrix M can also be expressed as

$$M = M_0 + \frac{1}{N}(\mathrm{tr}M)I, \tag{4.31}$$

where M_0 is an $N \times N$ traceless matrix. By combining equations 4.30 and 4.31, and defining the complex phase $\phi \equiv e^{-iL\mathrm{tr}\mathscr{H}_f/3}$ and the traceless matrix $T \equiv \mathscr{H}_f - (\mathrm{tr}\mathscr{H}_f)I/3$, we can write

$$e^{-i\mathscr{H}_f L} = \phi e^{-iLT} = \phi(a_0 I - iLTa_1 - L^2T^2a_2). \tag{4.32}$$

The coefficients a_0, a_1 and a_2 can be computed from the following system of linear equations:

$$\begin{aligned} e^{-iL\lambda_1} &= a_0 - iL\lambda_1 a_1 - L^2\lambda_1^2 a_2, & (4.33)\\ e^{-iL\lambda_2} &= a_0 - iL\lambda_2 a_1 - L^2\lambda_2^2 a_2, & (4.34)\\ e^{-iL\lambda_3} &= a_0 - iL\lambda_3 a_1 - L^2\lambda_3^2 a_2, & (4.35) \end{aligned}$$

where λ_1, λ_2 and λ_3 are the eigenvalues of T, by solving

$$\mathbf{a} = \Lambda^{-1}\mathbf{e}, \tag{4.36}$$

where

$$\mathbf{e} = \begin{pmatrix} e^{-iL\lambda_1} \\ e^{-iL\lambda_2} \\ e^{-iL\lambda_3} \end{pmatrix}, \Lambda = \begin{pmatrix} 1 - iL\lambda_1 - L^2\lambda_1^2 \\ 1 - iL\lambda_2 - L^2\lambda_2^2 \\ 1 - iL\lambda_3 - L^2\lambda_3^2 \end{pmatrix}, \mathbf{a} = \begin{pmatrix} a_0 \\ a_1 \\ a_2 \end{pmatrix}, \tag{4.37}$$

such that eventually we have

$$\begin{aligned} U_f(L) \equiv e^{-i\mathscr{H}_f L} &= \frac{1}{(\lambda_1-\lambda_2)(\lambda_1-\lambda_3)}\phi e^{-iL\lambda_1}[\lambda_2\lambda_3 I - (\lambda_2+\lambda_3)T + T^2] \\ &+ \frac{1}{(\lambda_2-\lambda_1)(\lambda_2-\lambda_3)}\phi e^{-iL\lambda_2}[\lambda_1\lambda_3 I - (\lambda_1+\lambda_3)T + T^2] \\ &+ \frac{1}{(\lambda_3-\lambda_1)(\lambda_3-\lambda_2)}\phi e^{-iL\lambda_3}[\lambda_1\lambda_2 I - (\lambda_1+\lambda_2)T + T^2]. \end{aligned} \tag{4.38}$$

The eigenvalues λ_i of T are solutions of the equation

$$\lambda^3 + c_2\lambda^2 + c_1\lambda + c_0 = 0, \tag{4.39}$$

where

$$\begin{aligned} c_0 &= -\mathrm{det}T, & (4.40)\\ c_1 &= T_{11}T_{22} - T_{12}T_{21} + T_{11}T_{33} - T_{13}T_{31} \\ &\quad + T_{22}T_{33} - T_{23}T_{32}, & (4.41)\\ c_2 &= -\mathrm{tr}T. & (4.42) \end{aligned}$$

5.2 Estimation of the mean free path

In the case that DE is a scalar field, in theory there could be a non-zero cross section for neutrino scatterings with DE-induced particles. In this Appendix, we show that this would have no effect on the neutrino propagation that we discuss in this chapter. To show this, we estimate the mean free path due to this DE-neutrino scattering interaction, following [5]. In order to simplify the estimate, here we assume the weak interaction for the coupling strength. We expect that this is well justified for high energies where the transition from vacuum to DE-induced oscillations occur.

Neglecting the neutrino mass, the cross section in the rest frame of the DE-induced particle is approximately

$$\sigma_{\nu\phi} \sim G_{\mathrm{F}} E m_\phi \sim 10^{-38}\ \mathrm{cm}^2 \left(\frac{E m_\phi}{\mathrm{GeV}^2}\right), \tag{4.43}$$

where G_{F} is the Fermi coupling constant, E is the neutrino energy, and m_ϕ is the mass of the DE-induced particle. The mean free path can then be calculated by $\ell \sim (n_\phi \sigma_{\nu\phi})^{-1}$, where n_ϕ is the number density of the DE-induced particles. Considering a neutrino of 100 PeV and assuming that the energy density of the DE-induced particle is of similar order as the local dark matter density, $\rho \sim 0.4\ \mathrm{GeV/cm}^3$ [344, 345, 346], we estimate $\ell \sim 10^5$ Mpc, which is much larger than the Hubble length. For lower neutrino energies, this value will be even larger. Thus, we can safely ignore any effect of a possible non-zero cross section for interactions between neutrinos and DE-induced particles.

5 Conclusions and Outlook

Working in the field of dark matter sometimes induces mixed feelings. The mystery around the missing mass makes the subject very attractive. How exciting it is to contribute to the solution of such a big problem in contemporary physics. However, it is also quite an unthankful field to work in. The lack of detections could result in some scepticism. But now and then a spark of hope gets lighted, for example when the excess in Reticulum II was observed, a galaxy without DM was detected, or when EDGES found an anomalous result suggesting a DM interpretation. Such moments refuel the motivation to unravel the nature of dark matter. Whatever this nature might be, it is still a challenging open question in astroparticle physics.

Neutrinos are much easier to love and more rewarding in their relation with the physicist. At least, we know for sure that they exist. Their flavor changing properties make them, in my humble opinion, by far the most interesting particles in the standard model. Besides studying their properties, neutrinos could also be used as a messenger in studying (the properties of) other physical processes, as we did in chapter 3 and chapter 4. With IceCube up and running and KM3NeT following in the near future, neutrino astrophysics is only becoming an even more interesting field.

In chapter 2, we investigated the impact of axisymmetric dark matter mass models on the upper limits on the dark matter annihilation cross section. We analysed seven classical dwarfs, Draco, Carina, Fornax, Leo I, Leo II, Sextans and Sculptor. For four of the selected dwarfs (Sextans, Carina, Sculptor and Fornax) axisymmetric mass models suggest a cored density profile rather than the commonly adopted cusped profile. We found that upper limits on the annihilation cross section for some of these dwarfs are significantly higher than the ones achieved using an NFW profile.

Therefore, upper limits in the literature obtained using spherical symmetric cusped profiles, such as the NFW, might be overestimated. Our results show that it is extremely important to use observationally motivated density profiles going beyond the usually adopted NFW in order to obtain accurate constraints on the dark matter annihilation cross section.

In chapter 3 we explored MeV dark matter in the context of the 21-cm EDGES results. We investigated the case of MeV milli-charged DM constituting 2% of the total DM in the Universe. We determined upper limits on the annihilation cross section using data from Super-Kamiokande, and predicted the limits that could be obtained through Hyper-Kamiokande, JUNO and DUNE. We found that data from Super-Kamiokande is not yet able to constrain this model, but future experiments might be. We furthermore explored MeV DM annihilation into solely neutrinos in general, and gave an update on the current limits.

In chapter 4, we explored the impact of a coupling between neutrinos and scalar-dark energy on the oscillation probability and flavor transitions in the three-flavor scheme. We find that DE-induced effects become observable for $E_\nu m_{\text{eff}} \sim 10^{-20}\text{GeV}^2$ and that CP is violated over a wide energy range. We also show that current and future experiments have the sensitivity to detect anomalous effects induced by a DE-neutrino coupling and probe the new mixing parameters. The DE-induced effects on neutrino oscillation can be distinguished from other new physics possibilities with similar effects, through the detection of the directional dependence of the interaction, which is specific to this interaction with DE. However, current experiments will not yet be able to measure the small changes of $\sim 0.03\%$ in the flavor composition due to this directional effect.

Similar flavor ratio effects as studies in chapter 4 could occur when neutrinos undergo interactions with dark matter. The effect would be larger when neutrinos propagate through dense DM regions. This would result in an anisotropic distribution of expected flavor ratios on the sky. Considering the DM distribution in the halo of our galaxy, and the smaller subhalos of the satellite galaxies, a map could be constructed of the expected alterations by interactions with DM, based on their direction of origin. At a certain level, this idea has been explored in the case of the galactic center in Ref. [326]. Unfortunately, our work performed on this subject is not in a close-to-finished state, and not part of this thesis.

In this thesis, we explored several aspects of the dark sector, using several methods. In contemporary astroparticle physics, I believe an important role is reserved for the neutrino, in both the search for dark matter and other new physics, and in the study of

astrophysical sources and processes. The recent identification of blazars as one of the high-energy neutrino sources marked the start of high-energy neutrino astrophysics. In this context, I believe the search for new physics effects on the neutrino flavor ratio is a very promising subject as well. This method can probe new physics effects that can not be detected in other ways, and is therefore a very exciting subject to work on.

Populaire Samenvatting

Alles wat je om je heen ziet, ook jijzelf, is opgebouwd uit moleculen, die op hun beurt weer zijn opgebouwd uit atomen. Atomen kunnen ook weer opgedeeld worden in protonen en neutronen, die de kern van de atomen vormen. Protonen en neutronen zijn opgebouwd uit quarks, wat elementaire deeltjes zijn. Elementaire deeltjes zijn de allerkleinste deeltjes waar alle materie uit bestaat. De protonen en neutronen in de atoomkern, worden omringd door elektronen, die we ook kennen van bijvoorbeeld de elektriciteit in huis. Een ander deeltje dat iedereen kent, is de foton, het lichtdeeltje. Maar er zijn ook deeltjes die wat minder bekend zijn, maar toch in groten getale aanwezig: zo schieten er per seconde ongeveer 45 biljoen neutrino's afkomstig van de zon door je lichaam! Neutrino's zijn ongeladen deeltjes die heel licht zijn, en zo goed als met de lichtsnelheid reizen. Ze ontstaan in sterrenkundige objecten, zoals de zon en andere sterren, maar ook in kernreacties op aarde. Neutrino's komen voor in drie verschillende smaken: elektron-neutrino's, muon-neutrino's en tau-neutrino's. Het bijzondere aan neutrino's is dat ze meestal een combinatie zijn van deze drie smaken, die tijdens de weg die ze afleggen, ook nog continu verandert. Een neutrino dat als elektron-neutrino begint, kan dus op een gegeven moment een tau-neutrino zijn. Dit noemen we *neutrino-oscillatie*. Sommige deeltjes zijn niet stabiel genoeg om zomaar op aarde voor te komen. Om deze deeltjes te onderzoeken, proberen wetenschappers met een grote deeltjesversneller de omstandigheden van het vroege heelal na te bootsen, om ze op die manier te kunnen creëren. Op die manier is een aantal jaar geleden het Higgs-deeltje ontdekt, dat er

voor zorgt dat de andere deeltjes massa kunnen hebben. Al deze deeltjes, en nog een aantal die ik hier verder niet heb genoemd, worden beschreven in het standaardmodel van elementaire deeltjes.

Toch is de materie die in het standaardmodel wordt beschreven, en die voor ons zo normaal is, juist best bijzonder. Het blijkt namelijk dat dit eigenlijk maar ongeveer 20% is van de totale materie in het heelal. Van 80% weten we niet wat het is! Deze onbekende materie noemen we *donkere materie*. Een van de aanwijzingen voor het bestaan van donkere materie, is het gedrag van de rotatiecurve van sterrenstelsels. De sterren in een sterrenstelsel draaien allemaal rond het midden van het sterrenstelsel, waar zich vaak een zwart gat bevindt, zoals bijvoorbeeld in onze eigen Melkweg. Volgens de zwaartekrachtswetten van Newton zouden de sterren die zich meer aan de buitenkant van het sterrenstelsel bevinden langzamer om het midden moeten draaien dan sterren die zich meer aan de binnenkant bevinden. Uit waarnemingen blijkt dat deze snelheid juist constant blijft. De sterren aan de buitenkant draaien zó snel dat ze volgens de zwaartekrachtsregels eigenlijk uit hun baan zouden moeten slingeren. Omdat dat niet gebeurt, denken wetenschappers dat we dus niet alle materie in het sterrenstelsel waarnemen, maar dat er ook nog onzichtbare materie aanwezig is die al die sterren bij elkaar houdt.

Wetenschappers proberen uit te zoeken wat deze donkere materie nu precies is. Een van de populairste ideeën is dat donkere materie bestaat uit WIMPS, *weakly interacting massive particles*. Dat zijn deeltjes die maar heel licht interacties aangaan met de deeltjes uit het standaardmodel, en daarom dus zo moeilijk waarneembaar zijn. Als deze deeltjes hun eigen anti-deeltje zijn, dan kunnen ze met zichzelf annihileren. Dat betekent dat ze elkaar opheffen, waarbij energie en andere deeltjes vrijkomen die we wel kunnen observeren. Een methode om donkere materie waar te nemen is via *indirecte detectie*, waarbij we dus naar deze vrijgekomen deeltjes zoeken. De deeltjes waarnaar we zoeken zijn gamma-straling, dat zijn fotonen in een bepaalde energie-bandbreedte, en neutrino's.

We zoeken naar deze deeltjes door met detectoren en telescopen naar

de ruimte te kijken in de richting waarvan we vermoeden dat daar veel donkere materie aanwezig is. Dit is bijvoorbeeld het geval in het centrum van de Melkweg, maar ook in de zogenaamde *dwarf spheroidal galaxies*. Dwarf spheroidal galaxies zijn satelliet-dwergsterrenstelsels van de Melkweg, kleine sterrenstelsels die om ons eigen sterrenstelsel heendraaien. Er is maar weinig ster-activiteit in deze sterrenstelsels, terwijl ze wel heel zwaar zijn. Daarom vermoeden we dat er veel donkere materie aanwezig moet zijn, en dat ze dus erg geschikt zijn voor indirecte detectie. Met de detectoren kijken we naar gamma-straling en neutrino's die uit de richting van zo'n dwergsterrenstelsel komen. Als dat meer is dan we verwachten op basis van andere sterrenkundige processen zou dat kunnen betekenen dat we de vrijgekomen deeltjes van de annihilatie van donkere materie hebben waargenomen. Tot nu toe is dat helaas nog niet duidelijk gebeurd. Als er geen donkere materie wordt waargenomen, kunnen we wel het beeld aanpassen dat we hebben van de precieze eigenschappen van een donkere-materiedeeltje, zoals de massa en de zogenaamde *werkzame doorsnede* van donkere-materie-annihilatie. De werkzame doorsnede vertelt ons hoe waarschijnlijk het is dat twee donkere-materiedeeltjes die elkaar tegenkomen daadwerkelijk annihileren. Wetenschappers hebben een idee van deze waarschijnlijkheid, en berekenen dan hoeveel gamma-straling of neutrino's we zouden verwachten te zien. Zien we die niet, dan moeten we die waarschijnlijkheid naar beneden bijstellen. Op die manier begrenzen we de mogelijke waarde van de werkzame doorsnede.

In het onderzoek dat ik heb verricht voor dit proefschrift hebben we ook bijgedragen aan indirecte detectie in dwergsterrenstelsels. In hoofdstuk 2 beschrijf ik ons onderzoek naar de donkere materie in zeven dwergsterrenstelsels. Om naar donkere materie te zoeken, is het belangrijk om te weten hoe het is verspreid. In de meeste analyses van dwergsterrenstelsels wordt het zogenaamde *NFW-model* gebruikt om deze verdeling van de donkere-materiedichtheid te beschrijven. In dit model is de verdeling van de donkere materie bolvormig, waarbij de dichtheid heel erg groot is in

het midden van de bol, en heel steil afneemt naar de buitenkant van de bol toe. Dit is een algemeen model dat is bepaald door alle sterrenstelsels op een grote hoop te gooien. Dit blijkt een goede benadering te geven, maar het is natuurlijk preciezer om voor elk sterrenstelsel individueel te kijken hoe de donkere materie is verdeeld. Als je dat doet, blijkt de verdeling bij de meeste dwergsterrenstelsels er meer als een rugbybal uit te zien dan als een perfecte bol, en neemt de dichtheid ook veel minder steil af vanuit het midden. Wij onderzochten de gamma-straling in de richting van zeven dwergsterrenstelsels op tekenen van donkere materie, en deden dit zowel met het NFW-model als aanname van de verdeling, als met de op maat gemaakte modellen. In geen gevallen vonden we een teken van donkere materie, en we hebben daarmee begrenzingen geplaatst op de werkzame doorsnede van donkere-materie-annihilatie. Als we de begrenzingen bepaald met behulp van het NFW-model vergelijken met de begrenzingen bepaald met het op maat gemaakte profiel, bevinden we dat de grenzen met het op maat gemaakte model zwakker zijn dan de grenzen met het NFW-model. Dat betekent dat we de mogelijke waarde van de waarschijnlijkheid dat twee donkere materie deeltjes annihileren eigenlijk minder naar beneden mogen bijstellen dan men tot nu toe heeft gedaan.

Waar we in hoofdstuk 2 gekeken hebben naar gamma-straling die mogelijk afkomstig was van donkere materie, keken we in hoofdstuk 3 naar neutrino's afkomstig van donkere materie. Recente resultaten van een experiment dat onderzoek doet naar het gas in een periode in het vroege heelal wijzen erop dat dit gas veel koeler was dan verwacht. Wetenschappers denken dat dit komt door botsingen tussen het gas en donkere-materiedeeltjes, waardoor het gas afkoelde. Andere deeltjes waren tijdens die periode namelijk te energetisch: botsingen tussen deze deeltjes en het gas zouden het gas juist hebben opgewarmd. Verder onderzoek naar deze verklaring wees uit dat de donkere-materiedeeltjes die hiervoor verantwoordelijk zouden zijn een aantal eigenschappen moeten hebben en aan een aantal voorwaardes moet voldoen. Zo moeten de deeltjes relatief licht zijn

(ongeveer duizend keer lichter dan de massa die we normaal gesproken verwachten) en ze mogen maar 2% van de totale donkere materie beslaan. Verder moet hun annihilatie een bepaalde waarde voor de werkzame doorsnede hebben. Wij hebben een donkere-materiemodel onderzocht dat aan deze eisen voldoet, waarin donkere materie alleen in muon- en tau-neutrino's kan annihileren, niet in andere deeltjes. We hebben uitgerekend hoeveel neutrino's we naar aanleiding van deze annihilatie van donkere-materiedeeltjes (vanuit de Melkweg, maar ook daarbuiten) op aarde zouden moeten detecteren. Vervolgens hebben we ongeveer tien jaar aan data van een neutrino-detector op aarde, Super-Kamiokande genaamd, onderzocht op signalen van deze donkere materie en hebben we een grens opgesteld voor de mogelijke werkzame doorsnede. Deze grens was niet sterk genoeg om dit donkere-materiemodel uit te sluiten. Daarom hebben we een voorspelling gedaan van de begrenzing die een aantal toekomstige gevoeligere en grotere experimenten zullen kunnen behalen. Daaruit bleek dat ook deze toekomstige experimenten aan tien jaar data niet genoeg zullen hebben om dit donkere-materiemodel uit te sluiten, maar misschien wel als ze lang genoeg data blijven verzamelen. Verder bleek dat het voor een hypothetisch experiment ter grootte van Hyper-Kamiokande (de opvolger van Super-Kamiokande), met de specificaties van JUNO (een ander toekomstig experiment), waarschijnlijk wel mogelijk is dit donkere-materiemodel uit te sluiten. Ook hebben we de begrenzing op de werkzame doorsnede bepaald voor gewone lichte (in gewicht) donkere materie, annihilerend naar alledrie de neutrino-smaken.

In hoofdstuk 4 deden we geen onderzoek naar donkere materie, maar naar een ander onderdeel van de zogenaamde donkere sector: *donkere energie*. Dit is de benaming voor de energie die de uitdijing van het heelal aandrijft. Dit kan een constante zijn, de kosmologische constante, of een scalair veld, dat over tijd en ruimte kan verschillen. In dat laatste geval kan dat effect hebben op neutrino-oscillaties. Zoals eerder beschreven, kunnen de verschillende neutrino-smaken op de weg die zij afleggen veranderen in een neutrino van een andere smaak. Elke neutrino heeft een bepaalde kans om na een bepaalde afstand een van de andere neutrino's te zijn. Wanneer een neutrino door materie reist, is deze kans

een beetje anders dan wanneer hij door vacuüm reist, omdat neutrino's interacties kunnen aangaan met de deeltjes in de materie. Zo'n zelfde effect kan optreden tussen donkere energie en neutrino's. Als er in een sterrenkundige bron in de verhouding één elektron-neutrino, twee muon-neutrino's en geen tau-neutrino's worden geproduceerd, meten we op aarde, na oscillatie, onder normale omstandigheden de verhouding één elektron-neutrino, één muon-neutrino en één tau-neutrino. In het geval dat er effecten optreden van nog onbekende natuurkunde kan deze verhouding afwijken. Wij hebben bepaald wat het effect is van een koppeling tussen donkere energie en neutrino's op deze verhouding in de smaken die we op aarde meten. In het geval dat we een afwijkende verhouding meten, kan dat dus het gevolg van deze koppeling zijn. Verder heeft de uitdijing van het heelal een voorkeursrichting, namelijk in alle richtingen naar buiten toe. Dit betekent dat de effecten op de neutrino-oscillatie ook een richtingsafhankelijkheid hebben. Wij hebben ook deze richtingsafhankelijkheid onderzocht. Deze effecten zijn echter zo klein dat ze met de huidige neutrino-telescopen niet op te merken zijn. De waarneming van deze richtingsafhankelijkheid zou wel het onstuitbare bewijs zijn voor het bestaan van een donkere-energie-neutrinokoppeling.

Popular Summary

Everything that you see around you, including yourself, is build up from molecules, which, in their turn, are build up from atoms. Atoms again can be divided into protons and neutrons, that make up the nucleus of an atom. Protons and neutrons consist of quarks, which are elementary particles. Elementary particles are the smallest particles possible, of which all matter is made up. The protons and neutrons in the nucleus are surrounded by electrons, which we also know from, for example, the electricity in our houses. Another particle that everybody knows of, is the photon, the light particle. But there are also particles that are less famous, but still present in immense amounts: for example, about 45 trillion neutrinos coming from the sun are crossing your body every second! Neutrinos are light-weighted neutral particles, that travel almost with the speed of light. They are produced in astrophysical sources, such as the Sun and other stars, but also in nuclear reactions at Earth. Neutrinos exist in three distinct flavors: electron neutrinos, muon neutrinos and tau neutrinos. The special thing about neutrinos is that they usually are a combination of these three flavors, which continuously changes during their journey. So, a neutrino starting as an electron neutrino, could be a tau neutrino at some later point. We call this *neutrino oscillation*. Some particles are not stable enough to appear on Earth under ordinary circumstances. To investigate these particles, scientists use enormous particle accelerators to try to create similar circumstances as those during the early Universe. This way, the Higgs particle was discovered a few years ago, which gives the other particles their masses. All these

particles, and some others that I did not mention, are described in the Standard Model of elementary particles.

However, the matter described by the Standard Model, which is so ordinary to all of us, is actually quite special. It turns out that this ordinary matter makes up only 20% of the total matter in the Universe. We do not know what the other 80% is made of! We call this unknown matter *Dark Matter*. One of the indications for the existence of dark matter, are the rotation curves of galaxies. The stars in a galaxy orbit its center, where often a black hole is located, like for example in our own Milky Way. According to Newton's laws of gravity, the stars located more in the outer regions of the galaxy should orbit on a slower speed around the center than stars located more in the inner regions. However, from observations it turned out that this orbital velocity stays constant. The stars in the outer regions orbit that fast, that according to the laws of gravity they should actually swing out of orbit. Since that does not happen, scientists think that we do not observe all the matter that is in there, but that there is some invisible matter present as well, keeping all the stars together.

Scientists try to find out what this dark matter is actually made of. One of the most popular ideas is that this dark matter consists of WIMPS, *weakly interacting massive particles*. These are particles that only undergo interactions with other particles in the SM very weakly, and therefore they are difficult to observe. If these particles are their own antiparticles, they could annihilate with themselves. This means that they cancel each other out, in which energy and other particles are released which we are able to observe. One method to observe dark matter is through *indirect detection*, in which we look for this released particles. The particles that we look for are gamma-rays, photons in a specific energy range, and neutrinos. We look for these particles by aiming detectors and telescopes at the sky in the direction that we suspect to comprise a lot of dark matter. This is for example the case in the center of the Milky Way, but also in the so-called *dwarf spheroidal galaxies*. Dwarf

spheroidal galaxies are satellite galaxies of the Milky Way: small galaxies that orbit our own galaxy. There is only little star-activity in these galaxies, while they are quite heavy in mass. Therefore we think they contain a lot of dark matter, which make them very suitable to search for dark matter using indirect detection. We use the detectors to look for gamma-rays and neutrinos coming from the direction of such a dwarf system. If we detect more of such particles than we expect based on other astrophysical processes, this could mean that we detected the particles that were released in annihilations of dark matter. Unfortunately this did not yet clearly happen. When no dark matter is observed, we can modify our image of the precise properties of the dark matter particle, such as its mass and the *cross section* of dark matter annihilation. The cross section tells us how likely it is that two dark matter particles that come across actually annihilate. Scientists have an idea of this likeliness and calculate the amount of gamma-rays or neutrinos that we would expect to see. If we do not see this calculated amount, we need to adjust this likeliness to some lower value. This way we put upper limits on the possible value of the cross section.

In the research that I performed for this thesis we also contributed to the indirect detection in dwarf galaxies. In chapter 2 I describe our research on dark matter in seven dwarf galaxies. To be able to search for dark matter, it is important to know how it is distributed. In most analyses of dwarf galaxies the so-called *NFW model* is being used to describe the dark matter density distribution. In this model the distribution of dark matter is spherical of shape. Its density is very large in the center of the sphere and decreases very steeply towards the outer parts. This model is a universal model, determined by putting all galaxies on one big pile. This turns out to be a very good approximation, but of course it is more precise to determine the dark matter distribution for every individual galaxy separately. When you do this it turns out that the dark matter distribution in most galaxies looks more like a rugby ball than like a perfect sphere. Furthermore, the density is much shallower in

the center. We studied gamma-rays coming from the direction of seven dwarf galaxies and looked for signs of dark matter. We did this for both the NFW profile and the customised profile. We did not find any signs of dark matter and put limits on the dark matter annihilation cross section. We find that the limits on the cross section determined with the customised profile are weaker than the limits determined using a NFW profile. This means that up til now, scientists adjusted the possible value of the likeliness that two dark matter particles annihilate to a lower value than one is actually allowed to.

While we looked for gamma-rays possibly coming from dark matter in chapter 2, in chapter 3 we looked for neutrinos coming from dark matter. Recent results of an experiment studying the gas during the early Universe imply that this gas was much cooler than expected. Scientists think that this is due to interactions between the gas and dark matter particles, resulting in the cooling of the gas. Other particles were too energetic in this period: interactions between these particles and the gas would result in the heating of the gas instead. More research on this explanation taught us what conditions these dark matter particles need to fulfil. To be able to explain the cooling of the gas, the dark matter particles need to be relatively light (about thousand times lighter than the mass that we usually expect), and they could only make up 2% of the total dark matter in the Universe. Furthermore, their cross section needs to be of a certain value. We investigated a dark matter model that fulfils these conditions, in which dark matter can only annihilate into muon- and tau neutrinos. We calculated how many neutrinos we would expect to detect on Earth, coming from the annihilation of this type of dark matter in both the Milky Way and outside. Thereafter we analysed about ten years of data from the neutrino detector Super-Kamiokande and put limits on the annihilation cross section. The limit is not strong enough to exclude the dark matter model. Therefore we also predicted the limits that we could obtain using several future experiments, which are larger and more sensitive than Super-Kamiokande. It turned out that these

future experiments are also not able to exclude the dark matter model using ten years of data, but they might be able to do this when they run for a long enough time. We also found that a hypothetical experiment with the size of Hyper-Kamiokande (the successor of Super-Kamiokande) and the specifications of JUNO (another future experiment) would probably be able to exclude the model. We also determined the limits on the cross section in the case of a more general light dark matter model, in which it makes up the entire 100% of the dark matter in the Universe and annihilates into all three neutrino flavors.

In chapter 4 we did not study dark matter. Instead we studied another subject in the dark sector: *dark energy*. This is the name for the energy driving the expansion of the Universe. This could be a constant, the cosmological constant, but it could also be a scalar-field that varies over space and time. In the latter case this could have an effect on neutrino oscillation. Like explained earlier, during their journey the neutrinos can change flavor. Every flavor neutrino has some probability to, after some distance, turn into a neutrino of another flavor. When a neutrino travels through matter this probability differs from the probability when a neutrino travels through vacuum, due to possible interactions between neutrinos and the particles in the matter. A similar effect could arise between neutrinos and dark energy. Neutrinos are produced in astrophysical sources with the ratio of one electron neutrino to two muon neutrinos to no tau neutrinos. Under normal circumstances we would measure, after neutrino oscillation, the ratio of one electron neutrino to one muon neutrino to one tau neutrino at Earth. When the neutrino oscillations get affected by physics that we not yet know of, the measured flavor ratio at Earth could deviate from the expectation. We determined the effect on this flavor ratio of a coupling between dark energy and neutrinos. In case we measure a flavor ratio at Earth that is not compatible to the expected ratio, this could be due to this coupling. Furthermore, the expansion of the Universe has a preferred direction: it goes outwards in all directions. This means that the effects on neutrino oscillation also have a directional dependence. We also studied this directional dependence. The effects we found are so small that it is not possible to observe them with the current neutrino telescopes. However, the observation of this directional dependence would be the smoking gun for the existence

of a dark energy-neutrino coupling.

Bibliography

[1] N. Klop, F. Zandanel, K. Hayashi, and S. Ando, Phys. Rev. **D95**, 123012 (2017), 1609.03509.

[2] N. Klop and S. Ando, Phys. Rev. **D97**, 063006 (2018), 1712.05413.

[3] N. Klop and S. Ando, Phys. Rev. **D98**, 103004 (2018), 1809.00671.

[4] M. Herrero, NATO Sci. Ser. C **534**, 1 (1999), hep-ph/9812242.

[5] C. Giunti and C. W. Kim, *Fundamentals of Neutrino Physics and Astrophysics* (, 2007).

[6] F. Englert and R. Brout, Phys. Rev. Lett. **13**, 321 (1964), [,157(1964)].

[7] P. W. Higgs, Phys. Rev. Lett. **13**, 508 (1964), [,160(1964)].

[8] D. Huterer and M. S. Turner, Phys. Rev. **D60**, 081301 (1999), astro-ph/9808133.

[9] S. Tsujikawa, Class. Quant. Grav. **30**, 214003 (2013), 1304.1961.

[10] Planck, P. A. R. Ade *et al.*, Astron. Astrophys. **571**, A15 (2014), 1303.5075.

[11] W. Pauli, in *Letter to a local meeting on radioactivity at Tübingen, Germany*, 1930.

[12] A. de Gouvea, TASI lectures on neutrino physics, in *Physics in D≥4. Proceedings, Theoretical Advanced Study Institute in elementary particle physics, TASI 2004, Boulder, USA, June 6-July 2, 2004*, pp. 197–258, 2004, hep-ph/0411274.

[13] S. M. Bilenky, Eur. Phys. J. **H38**, 345 (2013), 1210.3065.

[14] F. Reines and C. L. Cowan, Phys. Rev. **92**, 830 (1953).

[15] R. Davis, Jr., Phys. Rev. **97**, 766 (1955).

[16] G. Danby *et al.*, Phys. Rev. Lett. **9**, 36 (1962).

[17] C. S. Wu, E. Ambler, R. W. Hayward, D. D. Hoppes, and R. P. Hudson, Phys. Rev. **105**, 1413 (1957).

[18] T. D. Lee and C.-N. Yang, Phys. Rev. **105**, 1671 (1957), [,245(1957)].

[19] B. Pontecorvo, Sov. Phys. JETP **6**, 429 (1957), [Zh. Eksp. Teor. Fiz.33,549(1957)].

[20] B. Pontecorvo, Sov. Phys. JETP **7**, 172 (1958), [Zh. Eksp. Teor. Fiz.34,247(1957)].

[21] M. Nakagawa, Birth of neutrino oscillation, in *Scientific works of Masami Nakagawa*, pp. 414–424, 1998, hep-ph/9811358, [,414(1998)].

[22] V. N. Gribov and B. Pontecorvo, Phys. Lett. **28B**, 493 (1969).

[23] Super-Kamiokande, Y. Fukuda *et al.*, Phys. Rev. Lett. **81**, 1562 (1998), hep-ex/9807003.

[24] SNO, Q. R. Ahmad *et al.*, Phys. Rev. Lett. **87**, 071301 (2001), nucl-ex/0106015.

[25] Particle Data Group, M. Tanabashi *et al.*, Phys. Rev. **D98**, 030001 (2018).

[26] L. Wolfenstein, Phys. Rev. **D17**, 2369 (1978).

[27] S. P. Mikheyev and A. Yu. Smirnov, Sov. J. Nucl. Phys. **42**, 913 (1985), [,305(1986)].

[28] S. P. Mikheev and A. Yu. Smirnov, Nuovo Cim. **C9**, 17 (1986).

[29] I. Esteban, M. C. Gonzalez-Garcia, M. Maltoni, I. Martinez-Soler, and T. Schwetz, JHEP **01**, 087 (2017), 1611.01514.

[30] F. Capozzi *et al.*, Phys. Rev. **D95**, 096014 (2017), 1703.04471.

[31] Planck, N. Aghanim *et al.*, Astron. Astrophys. **596**, A107 (2016), 1605.02985.

[32] M. Auger *et al.*, JINST **7**, P05010 (2012), 1202.2192.

[33] KamLAND-Zen, A. Gando *et al.*, Phys. Rev. **C85**, 045504 (2012), 1201.4664.

[34] GERDA, K. H. Ackermann *et al.*, Eur. Phys. J. **C73**, 2330 (2013), 1212.4067.

[35] Majorana, R. Gaitskell *et al.*, (2003), nucl-ex/0311013.

[36] C. Kraus *et al.*, Eur. Phys. J. **C40**, 447 (2005), hep-ex/0412056.

[37] V. M. Lobashev *et al.*, Nucl. Phys. Proc. Suppl. **87**, 275 (2000), [,275(1999)].

[38] Kamiokande-II, E. W. Beier, THE KAMIOKANDE-II DETECTOR, in *7th Workshop on Grand Unification: ICOBAN 86 Toyama, Japan, April 16-18, 1986*, 1986.

[39] Kamiokande-II, K. Hirata *et al.*, Phys. Rev. Lett. **58**, 1490 (1987), [,727(1987)].

[40] Super-Kamiokande, K. Martens, The current status of the Super-Kamiokande experiment, in *Nuclear and particle physics with high-intensity proton accelerators. Proceedings, 25th International Symposium, Tokyo, Japan, December 3-6, 1996*, pp. 31–40, 1996.

[41] L. J. Watson, D. J. Mortlock, and A. H. Jaffe, Mon. Not. Roy. Astron. Soc. **418**, 206 (2011), 1010.0911.

[42] AMANDA, R. Morse *et al.*, The AMANDA neutrino astronomy project, in *5th International Symposium on Neutrino Telescopes Venice, Italy, March 2-4, 1993*, pp. 309–320, 1993.

[43] ANTARES, M. E. Moorhead, High-energy neutrino astronomy with ANTARES, in *Proceedings, fourth SFB-375 Ringberg workshop 'neutrino astrophysics' held Ringberg Castle, Tegernsee, Germany, 20-24 October 1997*, pp. 127–129, 1997, [,127(1997)].

[44] IceCube, G. C. Hill, Neutrino Astronomy with IceCube and AMANDA, in *Proceedings, 29th International Cosmic Ray Conference (ICRC 2005) - by Forschungszentrum Karlsruhe, Institute for Nuclear Physics, and University Karlsruhe, Institute for Experimental Nuclear Physics: Pune, India, August 3-11, 2005*, 2005.

[45] IceCube, A. Goldschmidt, The IceCube detector, in *27th International Cosmic Ray Conference (ICRC 2001) Hamburg, Germany, August 7-15, 2001*, pp. 1237–1240, 2001.

[46] IceCube, D. Williams, Int. J. Mod. Phys. Conf. Ser. **46**, 1860048 (2018).

[47] IceCube, M. G. Aartsen *et al.*, Phys. Rev. Lett. **113**, 101101 (2014), 1405.5303.

[48] IceCube, M. G. Aartsen *et al.*, The IceCube Neutrino Observatory - Contributions to ICRC 2015 Part II: Atmospheric and Astrophysical Diffuse Neutrino Searches of All Flavors, in *Proceedings, 34th International Cosmic Ray Conference (ICRC 2015): The Hague, The Netherlands, July 30-August 6, 2015*, 2015, 1510.05223.

[49] IceCube, M. G. Aartsen *et al.*, (2017), 1710.01191.

[50] A. Loeb and E. Waxman, JCAP **0605**, 003 (2006), astro-ph/0601695.

[51] F. W. Stecker, J. Phys. Conf. Ser. **60**, 215 (2007), astro-ph/0610208.

[52] K. Murase, M. Ahlers, and B. C. Lacki, Phys. Rev. **D88**, 121301 (2013), 1306.3417.

[53] H.-N. He, T. Wang, Y.-Z. Fan, S.-M. Liu, and D.-M. Wei, Phys. Rev. **D87**, 063011 (2013), 1303.1253.

[54] L. A. Anchordoqui, T. C. Paul, L. H. M. da Silva, D. F. Torres, and B. J. Vlcek, Phys. Rev. **D89**, 127304 (2014), 1405.7648.

[55] X.-C. Chang and X.-Y. Wang, Astrophys. J. **793**, 131 (2014), 1406.1099.

[56] X.-C. Chang, R.-Y. Liu, and X.-Y. Wang, Astrophys. J. **805**, 95 (2015), 1412.8361.

[57] N. Senno, P. Mészáros, K. Murase, P. Baerwald, and M. J. Rees, Astrophys. J. **806**, 24 (2015), 1501.04934.

[58] K. Emig, C. Lunardini, and R. Windhorst, JCAP **1512**, 029 (2015), 1507.05711.

[59] K. Bechtol, M. Ahlers, M. Di Mauro, M. Ajello, and J. Vandenbroucke, Astrophys. J. **836**, 47 (2017), 1511.00688.

[60] F. W. Stecker, C. Done, M. H. Salamon, and P. Sommers, Phys. Rev. Lett. **66**, 2697 (1991), [Erratum: Phys. Rev. Lett.69,2738(1992)].

[61] F. W. Stecker, Phys. Rev. **D88**, 047301 (2013), 1305.7404.

[62] O. Kalashev, D. Semikoz, and I. Tkachev, J. Exp. Theor. Phys. **120**, 541 (2015), 1410.8124.

[63] E. Waxman and J. N. Bahcall, Phys. Rev. Lett. **78**, 2292 (1997), astro-ph/9701231.

[64] K. Murase and K. Ioka, Phys. Rev. Lett. **111**, 121102 (2013), 1306.2274.

[65] S. Ando and J. F. Beacom, Phys. Rev. Lett. **95**, 061103 (2005), astro-ph/0502521.

[66] S. Dado and A. Dar, Phys. Rev. Lett. **113**, 191102 (2014), 1405.5487.

[67] S. Ando, I. Tamborra, and F. Zandanel, Phys. Rev. Lett. **115**, 221101 (2015),

1509.02444.

[68] F. Tavecchio and G. Ghisellini, Mon. Not. Roy. Astron. Soc. **451**, 1502 (2015), 1411.2783.

[69] P. Padovani and E. Resconi, Mon. Not. Roy. Astron. Soc. **443**, 474 (2014), 1406.0376.

[70] P. Padovani, M. Petropoulou, P. Giommi, and E. Resconi, Mon. Not. Roy. Astron. Soc. **452**, 1877 (2015), 1506.09135.

[71] F. Krauß *et al.*, Astron. Astrophys. **566**, L7 (2014), 1406.0645.

[72] Liverpool Telescope, MAGIC, H.E.S.S., AGILE, Kiso, VLA/17B-403, INTEGRAL, Kapteyn, Subaru, HAWC, Fermi-LAT, ASAS-SN, VERITAS, Kanata, IceCube, Swift NuSTAR, M. G. Aartsen *et al.*, Science **361**, eaat1378 (2018), 1807.08816.

[73] IceCube, M. G. Aartsen *et al.*, Science **361**, 147 (2018), 1807.08794.

[74] Icecube homepage, `https://icecube.wisc.edu/science/icecube/detector`, Accessed: 2018-10-02.

[75] KM3NeT, A. Kappes, (2007), 0711.0563.

[76] KM3Net, S. Adrian-Martinez *et al.*, J. Phys. **G43**, 084001 (2016), 1601.07459.

[77] ANITA, A. Silvestri *et al.*, NATO Sci. Ser. II **209**, 297 (2005), astro-ph/0411007, [,297(2004)].

[78] CARAVANE, G. F. Bignami *et al.*, The Cos-B Experiment for Gamma-Ray Astronomy., in *9th ESLAB Symposium on the Context and Status of Gamma Ray Astronomy – the Context and Status of Gamma Ray Astronomy, Frascati, Italy Frascati, Italy, June 10 - 12, 1974*, pp. 307–322, 1974.

[79] B. N. Swanenburg *et al.*, Astrophys. J. **243**, L69 (1981).

[80] GBM, Fermi-LAT, J. Conrad, L. Latronico, F. Longo, and B. Lott, CERN Cour. **48N9**, 13 (2008).

[81] Fermi-LAT, F. Acero *et al.*, Astrophys. J. Suppl. **218**, 23 (2015), 1501.02003.

[82] J. P. Rachen and P. Meszaros, Phys. Rev. **D58**, 123005 (1998), astro-ph/9802280.

[83] T. Kashti and E. Waxman, Phys. Rev. Lett. **95**, 181101 (2005), astro-

ph/0507599.

[84] L. A. Anchordoqui, H. Goldberg, F. Halzen, and T. J. Weiler, Phys. Lett. **B593**, 42 (2004), astro-ph/0311002.

[85] IceCube, M. G. Aartsen *et al.*, Nature Phys. **14**, 961 (2018), 1709.03434.

[86] M. Bustamante, J. F. Beacom, and W. Winter, Phys. Rev. Lett. **115**, 161302 (2015), 1506.02645.

[87] R. W. Rasmussen, L. Lechner, M. Ackermann, M. Kowalski, and W. Winter, (2017), 1707.07684.

[88] Particle Data Group, M. Tanabashi *et al.*, Phys. Rev. D **98**, 030001 (2018).

[89] F. Zwicky, Helv. Phys. Acta **6**, 110 (1933), [Gen. Rel. Grav.41,207(2009)].

[90] F. Zwicky, Astrophys. J. **86**, 217 (1937).

[91] V. C. Rubin and W. K. Ford, Jr., Astrophys. J. **159**, 379 (1970).

[92] V. C. Rubin, W. K. Ford, Jr., and N. Thonnard, Astrophys. J. **225**, L107 (1978).

[93] V. C. Rubin, N. Thonnard, and W. K. Ford, Jr., Astrophys. J. **238**, 471 (1980).

[94] G. S. Shostak and D. H. Rogstad, Astronomy and Astrophysics **24**, 405 (1973).

[95] D. H. Rogstad, G. S. Shostak, and A. H. Rots, Astronomy and Astrophysics **22**, 111 (1973).

[96] D. H. Rogstad, I. A. Lockhart, and M. C. H. Wright, Astrophysical Journal **193**, 309 (1974).

[97] G. A. Seielstad and M. C. H. Wright, Astrophysical Journal **184**, 343 (1973).

[98] M. S. Roberts and R. N. Whitehurst, Astrophysical Journal **201**, 327 (1975).

[99] W. K. Huchtmeier, Astronomy and Astrophysics **45**, 259 (1975).

[100] A. Bosma, *The distribution and kinematics of neutral hydrogen in spiral galaxies of various morphological types*, PhD thesis, PhD Thesis, Groningen Univ., (1978), 1978.

[101] T. S. van Albada, J. N. Bahcall, K. Begeman, and R. Sancisi, Astrophys. J. **295**, 305 (1985).

[102] J. P. Ostriker, P. J. E. Peebles, and A. Yahil, Astrophysical Journal **193**, L1

(1974).

[103] J. de Swart, G. Bertone, and J. van Dongen, (2017), 1703.00013, [Nature Astron.1,0059(2017)].

[104] WMAP Science Team, E. Komatsu *et al.*, PTEP **2014**, 06B102 (2014), 1404.5415.

[105] Planck, N. Aghanim *et al.*, (2018), 1807.06209.

[106] Planck, P. A. R. Ade *et al.*, Astron. Astrophys. **594**, A13 (2016), 1502.01589.

[107] MACHO, C. Alcock *et al.*, Astrophys. J. **542**, 281 (2000), astro-ph/0001272.

[108] EROS, T. Lasserre, Astron. Astrophys. **355**, L39 (2000), astro-ph/0002253.

[109] EROS-2, P. Tisserand *et al.*, Astron. Astrophys. **469**, 387 (2007), astro-ph/0607207.

[110] Virgo, LIGO Scientific, B. P. Abbott *et al.*, Phys. Rev. Lett. **116**, 061102 (2016), 1602.03837.

[111] S. Bird *et al.*, Phys. Rev. Lett. **116**, 201301 (2016), 1603.00464.

[112] S. Clesse and J. García-Bellido, Phys. Dark Univ. **15**, 142 (2017), 1603.05234.

[113] P. Ivanov, P. Naselsky, and I. Novikov, Phys. Rev. D **50**, 7173 (1994).

[114] M. Yu. Khlopov, Res. Astron. Astrophys. **10**, 495 (2010), 0801.0116.

[115] B. J. Carr, K. Kohri, Y. Sendouda, and J. Yokoyama, Phys. Rev. **D81**, 104019 (2010), 0912.5297.

[116] D. Blais, C. Kiefer, and D. Polarski, Phys. Lett. **B535**, 11 (2002), astro-ph/0203520.

[117] N. Afshordi, P. McDonald, and D. N. Spergel, Astrophys. J. **594**, L71 (2003), astro-ph/0302035.

[118] P. H. Frampton, M. Kawasaki, F. Takahashi, and T. T. Yanagida, JCAP **1004**, 023 (2010), 1001.2308.

[119] B. Carr, F. Kuhnel, and M. Sandstad, Phys. Rev. **D94**, 083504 (2016), 1607.06077.

[120] D. Gaggero *et al.*, Phys. Rev. Lett. **118**, 241101 (2017), 1612.00457.

[121] S. D. M. White, C. S. Frenk, and M. Davis, Astrophys. J. **274**, L1 (1983),

[,80(1984)].

[122] D. Clowe *et al.*, Astrophys. J. **648**, L109 (2006), astro-ph/0608407.

[123] M. Markevich and D. Clowe, in *X-ray: NASA/CXC/CfA/M.Markevitch et al.; Optical: NASA/STScI; Magellan/U.Arizona/D.Clowe et al.; Lensing Map: NASA/STScI; ESO WFI; Magellan/U.Arizona/D.Clowe et al.*, 2006.

[124] R. D. Peccei, CP violation: A Theoretical review, in *2nd Workshop on Physics and Detectors for DAPHNE (DAPHNE 95) Frascati, Italy, April 4-7, 1995*, 1995, hep-ph/9508389.

[125] R. D. Peccei and H. R. Quinn, Phys. Rev. Lett. **38**, 1440 (1977), [,328(1977)].

[126] S. Weinberg, Phys. Rev. Lett. **40**, 223 (1978).

[127] F. Wilczek, Phys. Rev. Lett. **40**, 279 (1978).

[128] J. Preskill, M. B. Wise, and F. Wilczek, Phys. Lett. **B120**, 127 (1983), [,URL(1982)].

[129] M. Dine and W. Fischler, Physics Letters B **120**, 137 (1983).

[130] J. E. Kim, Phys. Rept. **150**, 1 (1987).

[131] L. D. Duffy and K. van Bibber, New J. Phys. **11**, 105008 (2009), 0904.3346.

[132] ADMX, N. Du *et al.*, Phys. Rev. Lett. **120**, 151301 (2018), 1804.05750.

[133] A. Garcon *et al.*, (2017), 1707.05312.

[134] CAST, S. Aune *et al.*, Solar axion search with the CAST experiment, in *Proceedings, 34th International Conference on High Energy Physics (ICHEP 2008): Philadelphia, Pennsylvania, July 30-August 5, 2008*, 2008, 0810.1874.

[135] J. K. Vogel *et al.*, IAXO - The International Axion Observatory, in *8th Patras Workshop on Axions, WIMPs and WISPs (AXION-WIMP 2012) Chicago, Illinois, July 18-22, 2012*, 2013, 1302.3273.

[136] P. W. Graham, I. G. Irastorza, S. K. Lamoreaux, A. Lindner, and K. A. van Bibber, Ann. Rev. Nucl. Part. Sci. **65**, 485 (2015), 1602.00039.

[137] A. Boyarsky, M. Drewes, T. Lasserre, S. Mertens, and O. Ruchayskiy, (2018), 1807.07938.

[138] S. Weinberg, Phys. Lett. **82B**, 387 (1979).

[139] H. Georgi and S. L. Glashow, Phys. Rev. Lett. **32**, 438 (1974).

[140] B. Zumino, Physica **A96**, 99 (1979).

[141] H. Komatsu and J. Kubo, Nucl. Phys. **B263**, 265 (1986).

[142] G. Bertone, D. Hooper, and J. Silk, Phys. Rept. **405**, 279 (2005), hep-ph/0404175.

[143] G. Jungman, M. Kamionkowski, and K. Griest, Phys. Rept. **267**, 195 (1996), hep-ph/9506380.

[144] G. Steigman, B. Dasgupta, and J. F. Beacom, Phys. Rev. **D86**, 023506 (2012), 1204.3622.

[145] M. Milgrom, ApJ**270**, 365 (1983).

[146] M. Milgrom, Acta Phys. Polon. **B32**, 3613 (2001), astro-ph/0112069.

[147] E. P. Verlinde, SciPost Phys. **2**, 016 (2017), 1611.02269.

[148] P. van Dokkum *et al.*, Nature **555**, 629 (2018), 1803.10237.

[149] XENON1T, E. Aprile, Springer Proc. Phys. **148**, 93 (2013), 1206.6288.

[150] F. Kahlhoefer, Int. J. Mod. Phys. **A32**, 1730006 (2017), 1702.02430.

[151] J. F. Navarro, C. S. Frenk, and S. D. M. White, Astrophys. J. **462**, 563 (1996), astro-ph/9508025.

[152] J. F. Navarro, C. S. Frenk, and S. D. M. White, Astrophys. J. **490**, 493 (1997), astro-ph/9611107.

[153] J. F. Navarro *et al.*, Mon. Not. Roy. Astron. Soc. **349**, 1039 (2004), astro-ph/0311231.

[154] J. Einasto, Trudy Astrofizicheskogo Instituta Alma-Ata **5**, 87 (1965).

[155] J. Einasto, Publications of the Tartu Astrofizica Observatory **36**, 414 (1968).

[156] J. Einasto and U. Haud, Astronomy and Astrophysic **223**, 89 (1989).

[157] A. Burkert, IAU Symp. **171**, 175 (1996), astro-ph/9504041, [Astrophys. J.447,L25(1995)].

[158] B. Moore, Nature **370**, 629 (1994).

[159] T. Fukushige and J. Makino, Astrophys. J. **477**, L9 (1997), astro-ph/9610005.

[160] J. Diemand *et al.*, Nature **454**, 735 (2008), 0805.1244.

[161] T. Ishiyama *et al.*, Astrophys. J. **767**, 146 (2013), 1101.2020.

[162] W. J. G. de Blok, S. S. McGaugh, and V. C. Rubin, Astron. J. **122**, 2396 (2001).

[163] G. Gilmore *et al.*, Astrophys. J. **663**, 948 (2007), astro-ph/0703308.

[164] W. J. G. de Blok, Adv. Astron. **2010**, 789293 (2010), 0910.3538.

[165] M. Kuhlen, J. Diemand, and P. Madau, Astrophys. J. **671**, 1135 (2007), 0705.2037.

[166] M. D. Schneider, C. S. Frenk, and S. Cole, JCAP **1205**, 030 (2012), 1111.5616.

[167] C. Vera-Ciro, L. V. Sales, A. Helmi, and J. F. Navarro, Mon. Not. Roy. Astron. Soc. **439**, 2863 (2014), 1402.0903.

[168] M. Irwin and D. Hatzidimitriou, Mon. Not. Roy. Astron. Soc. **277**, 1354 (1995).

[169] A. McConnachie and M. Irwin, Mon. Not. Roy. Astron. Soc. **365**, 1263 (2006), astro-ph/0511004.

[170] K. Hayashi and M. Chiba, Astrophys. J. **755**, 145 (2012), 1206.3888.

[171] K. Hayashi and M. Chiba, Astrophys. J. **810**, 22 (2015), 1507.07620.

[172] W. B. Atwood *et al.*, The Astrophysical Journal **697**, 1071 (2009), 0902.1089.

[173] E. A. Baltz *et al.*, JCAP **0807**, 013 (2008), 0806.2911.

[174] HAWC, G. Sinnis, AIP Conf. Proc. **745**, 234 (2005), [,234(2005)].

[175] MAGIC, E. Lorenz, The project for a 17-m diameter air Cherenkov telescope for gamma astronomy, in *Very high-energy phenomena in the universe. Proceedings, 32nd Rencontres de Moriond, Les Arcs, France, January 18-25, 1997*, pp. 167–173, 1997.

[176] VERITAS, R. W. Lessard, Astropart. Phys. **11**, 243 (1999).

[177] HESS, B. Khelifi, First results from the H.E.S.S. detector, in *Proceedings, 2nd Workshop on Science with the New Generation of High Energy Gamma-ray Experiments : Between Astrophysics and Astroparticle Physics (SciNeGHE 2004): Bari, Italy, June 21, 2004*, pp. 89–100, 2004.

[178] CTA Consortium, T. Schweizer, G. Hermann, W. Hofmann, and M. Teshima,

Cherenkov Telescope Array: The next-generation ground-based gamma-ray observatory, in *Proceedings, 30th International Cosmic Ray Conference (ICRC 2007): Merida, Yucatan, Mexico, July 3-11, 2007* Vol. 3, pp. 1313–1316, 2007, 0709.2048, [3,1313(2007)].

[179] Fermi-LAT, W. B. Atwood *et al.*, Astrophys. J. **697**, 1071 (2009), 0902.1089.

[180] L. Goodenough and D. Hooper, (2009), 0910.2998.

[181] Fermi-LAT, V. Vitale and A. Morselli, Indirect Search for Dark Matter from the center of the Milky Way with the Fermi-Large Area Telescope, in *Fermi gamma-ray space telescope. Proceedings, 2nd Fermi Symposium, Washington, USA, November 2-5, 2009*, 2009, 0912.3828.

[182] D. Hooper and L. Goodenough, Phys. Lett. **B697**, 412 (2011), 1010.2752.

[183] D. Hooper and T. Linden, Phys. Rev. **D84**, 123005 (2011), 1110.0006.

[184] K. N. Abazajian and M. Kaplinghat, Phys. Rev. **D86**, 083511 (2012), 1207.6047, [Erratum: Phys. Rev.D87,129902(2013)].

[185] C. Gordon and O. Macias, Phys. Rev. **D88**, 083521 (2013), 1306.5725, [Erratum: Phys. Rev.D89,no.4,049901(2014)].

[186] O. Macias and C. Gordon, Phys. Rev. **D89**, 063515 (2014), 1312.6671.

[187] K. N. Abazajian, N. Canac, S. Horiuchi, and M. Kaplinghat, Phys. Rev. **D90**, 023526 (2014), 1402.4090.

[188] B. Zhou *et al.*, Phys. Rev. **D91**, 123010 (2015), 1406.6948.

[189] F. Calore, I. Cholis, and C. Weniger, JCAP **1503**, 038 (2015), 1409.0042.

[190] F. Calore, I. Cholis, C. McCabe, and C. Weniger, Phys. Rev. **D91**, 063003 (2015), 1411.4647.

[191] Fermi-LAT, M. Ajello *et al.*, Astrophys. J. **819**, 44 (2016), 1511.02938.

[192] Fermi-LAT, M. Ackermann *et al.*, Astrophys. J. **840**, 43 (2017), 1704.03910.

[193] J. M. Siegal-Gaskins, (2013), 1308.2228, [Proc. Nat. Acad. Sci.112,2243(2015)].

[194] K. N. Abazajian, JCAP **1103**, 010 (2011), 1011.4275.

[195] R. Bartels, S. Krishnamurthy, and C. Weniger, Phys. Rev. Lett. **116**, 051102 (2016), 1506.05104.

[196] S. K. Lee, M. Lisanti, B. R. Safdi, T. R. Slatyer, and W. Xue, Phys. Rev. Lett. **116**, 051103 (2016), 1506.05124.

[197] R. T. Bartels, T. D. P. Edwards, and C. Weniger, (2018), 1805.11097.

[198] M. Mateo, Ann. Rev. Astron. Astrophys. **36**, 435 (1998), astro-ph/9810070.

[199] M. Winter, G. Zaharijas, K. Bechtol, and J. Vandenbroucke, Astrophys. J. **832**, L6 (2016), 1607.06390.

[200] Fermi-LAT, M. Ackermann *et al.*, Phys. Rev. Lett. **115**, 231301 (2015), 1503.02641.

[201] Fermi-LAT, MAGIC, M. L. Ahnen *et al.*, JCAP **1602**, 039 (2016), 1601.06590.

[202] Fermi-LAT, M. Wood, B. Anderson, A. Drlica-Wagner, J. Cohen-Tanugi, and J. Conrad, PoS **ICRC2015**, 1226 (2016), 1507.03530.

[203] DES, Fermi-LAT, A. Albert *et al.*, Astrophys. J. **834**, 110 (2017), 1611.03184.

[204] D. Hooper and T. Linden, JCAP **1509**, 016 (2015), 1503.06209.

[205] DES, Fermi-LAT, A. Drlica-Wagner *et al.*, Astrophys. J. **809**, L4 (2015), 1503.02632.

[206] A. Geringer-Sameth *et al.*, Phys. Rev. Lett. **115**, 081101 (2015), 1503.02320.

[207] J. D. Bowman, A. E. E. Rogers, and J. N. Hewitt, Astrophys. J. **676**, 1 (2008), 0710.2541.

[208] J. R. Pritchard and A. Loeb, Rept. Prog. Phys. **75**, 086901 (2012), 1109.6012.

[209] J. D. Bowman, A. E. E. Rogers, R. A. Monsalve, T. J. Mozdzen, and N. Mahesh, Nature **555**, 67 (2018).

[210] A. Cohen, A. Fialkov, R. Barkana, and M. Lotem, Mon. Not. Roy. Astron. Soc. **472**, 1915 (2017), 1609.02312.

[211] R. Barkana, Nature **555**, 71 (2018), 1803.06698.

[212] A. Fialkov, R. Barkana, and A. Cohen, Phys. Rev. Lett. **121**, 011101 (2018), 1802.10577.

[213] H. Tashiro, K. Kadota, and J. Silk, Phys. Rev. **D90**, 083522 (2014), 1408.2571.

[214] J. B. Muñoz, E. D. Kovetz, and Y. Ali-Haïmoud, Phys. Rev. **D92**, 083528 (2015), 1509.00029.

[215] J. B. Muñoz and A. Loeb, Nature **557**, 684 (2018), 1802.10094.

[216] A. Berlin, D. Hooper, G. Krnjaic, and S. D. McDermott, Phys. Rev. Lett. **121**, 011102 (2018), 1803.02804.

[217] E. D. Kovetz *et al.*, (2018), 1807.11482.

[218] E. Komatsu *et al.*, ApJS **192**, 18 (2011), 1001.4538.

[219] G. Bertone, D. Hooper, and J. Silk, Physics Reports **405**, 279 (2005), hep-ph/0404175.

[220] J. M. Gaskins, Contemp. Phys. **57**, 496 (2016), 1604.00014.

[221] E. Aliu *et al.*, ApJ **697**, 1299 (2009), 0810.3561.

[222] V. A. Acciari *et al.*, ApJ **720**, 1174 (2010), 1006.5955.

[223] J. Aleksić *et al.*, JCAP **6**, 035 (2011), 1103.0477.

[224] M. Ackermann *et al.*, Physical Review Letters **107**, 241302 (2011), 1108.3546.

[225] E. Aliu *et al.*, Physics Review D **85**, 062001 (2012), 1202.2144.

[226] J. Aleksić *et al.*, JCAP **2**, 008 (2014), 1312.1535.

[227] A. A. Abdo *et al.*, ApJ **712**, 147 (2010), 1001.4531.

[228] M. Ackermann *et al.*, Physics Review D **89**, 042001 (2014), 1310.0828.

[229] A. Abramowski *et al.*, Physics Review D **90**, 112012 (2014), 1410.2589.

[230] A. Geringer-Sameth, S. M. Koushiappas, and M. G. Walker, Phys. Rev. **D91**, 083535 (2015), 1410.2242.

[231] A. Drlica-Wagner *et al.*, ApJl **809**, L4 (2015), 1503.02632.

[232] MAGIC Collaboration, JCAP **2**, 039 (2016), 1601.06590.

[233] S. Li *et al.*, Phys. Rev. D **93**, 043518 (2016).

[234] A. Abramowski *et al.*, Physical Review Letters **106**, 161301 (2011), 1103.3266.

[235] D. Hooper and T. Linden, Physics Review D **84**, 123005 (2011), 1110.0006.

[236] A. Abramowski *et al.*, Physical Review Letters **114**, 081301 (2015), 1502.03244.

[237] F. Calore, I. Cholis, and C. Weniger, JCAP **3**, 038 (2015), 1409.0042.

[238] T. Daylan *et al.*, Physics of the Dark Universe **12**, 1 (2016), 1402.6703.

[239] F. Calore, I. Cholis, C. McCabe, and C. Weniger, Physics Review D **91**, 063003 (2015), 1411.4647.

[240] M. Ajello *et al.*, ApJ **819**, 44 (2016).

[241] J. Aleksić *et al.*, ApJ **710**, 634 (2010), 0909.3267.

[242] M. Ackermann *et al.*, JCAP **5**, 025 (2010), 1002.2239.

[243] A. Abramowski *et al.*, ApJ **750**, 123 (2012), 1202.5494.

[244] S. Ando and D. Nagai, JCAP **7**, 017 (2012), 1201.0753.

[245] T. Arlen *et al.*, ApJ **757**, 123 (2012), 1208.0676.

[246] M. Ackermann *et al.*, ApJ **812**, 159 (2015), 1510.00004.

[247] B. Anderson *et al.*, JCAP **2**, 026 (2016), 1511.00014.

[248] Y.-F. Liang *et al.*, Phys. Rev. D **93**, 103525 (2016).

[249] M. Ackermann *et al.*, Physics Review D **85**, 083007 (2012), 1202.2856.

[250] M. Fornasa *et al.*, MNRAS **429**, 1529 (2013), 1207.0502.

[251] S. Ando and E. Komatsu, Physics Review D **87**, 123539 (2013), 1301.5901.

[252] S. Ando, A. Benoit-Lévy, and E. Komatsu, Physics Review D **90**, 023514 (2014), 1312.4403.

[253] G. A. Gómez-Vargas *et al.*, Nuclear Instruments and Methods in Physics Research A **742**, 149 (2014), 1303.2154.

[254] M. Fornasa and M. A. Sánchez-Conde, Physics Reports **598**, 1 (2015), 1502.02866.

[255] A. Cuoco *et al.*, ApJs **221**, 29 (2015), 1506.01030.

[256] S. Camera, M. Fornasa, N. Fornengo, and M. Regis, JCAP **6**, 029 (2015), 1411.4651.

[257] N. Fornengo, L. Perotto, M. Regis, and S. Camera, ApJl **802**, L1 (2015), 1410.4997.

[258] M. Regis *et al.*, Phys. Rev. Lett. **114**, 241301 (2015), 1503.05922.

[259] S. Ando and K. Ishiwata, JCAP **1606**, 045 (2016), 1604.02263.

[260] M. Fornasa *et al.*, (2016), 1608.07289.

[261] M. L. Mateo, Annual Review of Astronomy and Astrophysics **36**, 435 (1998), astro-ph/9810070.

[262] L. E. Strigari, S. M. Koushiappas, J. S. Bullock, and M. Kaplinghat, Physics Review D **75**, 083526 (2007), astro-ph/0611925.

[263] L. E. Strigari *et al.*, ApJ **678**, 614 (2008), 0709.1510.

[264] M. A. Sánchez-Conde, M. Cannoni, F. Zandanel, M. E. Gómez, and F. Prada, JCAP **12**, 011 (2011), 1104.3530.

[265] A. Chiappo *et al.*, (2016), 1608.07111.

[266] J. Einasto, Trudy Astrofizicheskogo Instituta Alma-Ata **5**, 87 (1965).

[267] A. W. McConnachie, Astronomical Journal **144**, 4 (2012), 1204.1562.

[268] C. A. Vera-Ciro, L. V. Sales, A. Helmi, and J. F. Navarro, MNRAS **439**, 2863 (2014), 1402.0903.

[269] P. Ullio and M. Valli, JCAP **1607**, 025 (2016), 1603.07721.

[270] V. Bonnivard, C. Combet, D. Maurin, and M. G. Walker, Mon. Not. Roy. Astron. Soc. **446**, 3002 (2015), 1407.7822.

[271] G. D. Martinez, mnras **451**, 2524 (2015), 1309.2641.

[272] J. Binney and S. Tremaine, *Galactic dynamics* (, 1987).

[273] S. Colafrancesco, S. Profumo, and P. Ullio, Phys. Rev. **D75**, 023513 (2007), astro-ph/0607073.

[274] K. Hayashi *et al.*, Mon. Not. Roy. Astron. Soc. **461**, 2914 (2016), 1603.08046.

[275] J. Binney and S. Tremaine, *Galactic Dynamics: Second Edition* (Princeton University Press, 2008).

[276] M. Cappellari, mnras **390**, 71 (2008), 0806.0042.

[277] E. Tempel and P. Tenjes, mnras **371**, 1269 (2006), astro-ph/0606680.

[278] H. C. Plummer, mnras **71**, 460 (1911).

[279] T. Sjostrand, S. Mrenna, and P. Z. Skands, JHEP **05**, 026 (2006), hep-ph/0603175.

[280] Super-Kamiokande, K. Bays *et al.*, Phys. Rev. **D85**, 052007 (2012), 1111.5031.

[281] S. Ando and K. Sato, New J. Phys. **6**, 170 (2004), astro-ph/0410061.

[282] J. F. Beacom, Ann. Rev. Nucl. Part. Sci. **60**, 439 (2010), 1004.3311.

[283] C. Lunardini, Astropart. Phys. **79**, 49 (2016), 1007.3252.

[284] Hyper-Kamiokande, K. Abe *et al.*, (2018), 1805.04163.

[285] DUNE, J. Strait, DUNE Physics, in , 2015.

[286] JUNO, V. Antonelli and L. Miramonti, PoS **NEUTEL2017**, 056 (2018), 1710.07401.

[287] S. Palomares-Ruiz and S. Pascoli, Phys. Rev. **D77**, 025025 (2008), 0710.5420.

[288] A. Olivares-Del Campo, S. Palomares-Ruiz, and S. Pascoli, Implications of a Dark Matter-Neutrino Coupling at Hyper-Kamiokande, in *Moriond EW 2018, March 10-17, 2018*, 1805.09830.

[289] E. G. Adelberger *et al.*, Phys. Rev. Lett. **98**, 131104 (2007), hep-ph/0611223.

[290] D. J. Kapner *et al.*, Phys. Rev. Lett. **98**, 021101 (2007), hep-ph/0611184.

[291] H. Yuksel, S. Horiuchi, J. F. Beacom, and S. Ando, Phys. Rev. **D76**, 123506 (2007), 0707.0196.

[292] S. Ando and E. Komatsu, Phys. Rev. **D87**, 123539 (2013), 1301.5901.

[293] N. Hiroshima, S. Ando, and T. Ishiyama, Phys. Rev. **D97**, 123002 (2018), 1803.07691.

[294] A. Strumia and F. Vissani, Phys. Lett. **B564**, 42 (2003), astro-ph/0302055.

[295] S. Skadhauge and R. Zukanovich Funchal, JCAP **0704**, 014 (2007), hep-ph/0611194.

[296] J. F. Beacom and M. R. Vagins, Phys. Rev. Lett. **93**, 171101 (2004), hep-ph/0309300.

[297] JUNO, H. Lu and E. Baussan, J. Phys. Conf. Ser. **888**, 012088 (2017).

[298] A. G. Cocco, A. Ereditato, G. Fiorillo, G. Mangano, and V. Pettorino, JCAP **0412**, 002 (2004), hep-ph/0408031.

[299] DUNE, V. A. Kudryavtsev, J. Phys. Conf. Ser. **718**, 062032 (2016), 1601.03496.

[300] V. De Romeri, E. Fernandez-Martinez, and M. Sorel, JHEP **09**, 030 (2016), 1607.00293.

[301] JUNO, F. An *et al.*, J. Phys. **G43**, 030401 (2016), 1507.05613.

[302] T. D. P. Edwards and C. Weniger, (2017), 1712.05401.

[303] T. D. P. Edwards and C. Weniger, JCAP **1802**, 021 (2018), 1704.05458.

[304] K. K. Boddy *et al.*, (2018), 1808.00001.

[305] Super-Kamiokande, M. Malek *et al.*, Phys. Rev. Lett. **90**, 061101 (2003), hep-ex/0209028.

[306] LAGUNA, D. Angus *et al.*, European strategy for future neutrino physics. 69 Proceedings, Workshop, Geneva, Switzerland, October 1-3, 2009 , 226 (2010), 1001.0077.

[307] S. Weinberg, Rev. Mod. Phys. **61**, 1 (1989).

[308] S. M. Carroll, Living Rev. Rel. **4**, 1 (2001), astro-ph/0004075.

[309] E. J. Copeland, M. Sami, and S. Tsujikawa, Int. J. Mod. Phys. **D15**, 1753 (2006), hep-th/0603057.

[310] R. R. Caldwell and M. Kamionkowski, Ann. Rev. Nucl. Part. Sci. **59**, 397 (2009), 0903.0866.

[311] T.-K. Kuo and J. T. Pantaleone, Rev. Mod. Phys. **61**, 937 (1989).

[312] IceCube, M. G. Aartsen *et al.*, JINST **12**, P03012 (2017), 1612.05093.

[313] ANITA, P. W. Gorham *et al.*, Astropart. Phys. **32**, 10 (2009), 0812.1920.

[314] Pierre Auger, A. Aab *et al.*, Nucl. Instrum. Meth. **A798**, 172 (2015), 1502.01323.

[315] S. Ando, M. Kamionkowski, and I. Mocioiu, Phys. Rev. **D80**, 123522 (2009), 0910.4391.

[316] C. A. Argüelles, T. Katori, and J. Salvado, Phys. Rev. Lett. **115**, 161303 (2015), 1506.02043.

[317] S. R. Coleman and S. L. Glashow, Phys. Rev. **D59**, 116008 (1999), hep-ph/9812418.

[318] V. D. Barger, S. Pakvasa, T. J. Weiler, and K. Whisnant, Phys. Rev. Lett. **85**, 5055 (2000), hep-ph/0005197.

[319] G. Barenboim, L. Borissov, and J. D. Lykken, Phys. Lett. **B534**, 106 (2002),

hep-ph/0201080.

[320] V. A. Kostelecky and M. Mewes, Phys. Rev. **D69**, 016005 (2004), hep-ph/0309025.

[321] J. Christian, Phys. Rev. **D71**, 024012 (2005), gr-qc/0409077.

[322] D. Hooper, D. Morgan, and E. Winstanley, Phys. Rev. **D72**, 065009 (2005), hep-ph/0506091.

[323] T. Katori, V. A. Kostelecky, and R. Tayloe, Phys. Rev. **D74**, 105009 (2006), hep-ph/0606154.

[324] A. Kostelecky and M. Mewes, Phys. Rev. **D85**, 096005 (2012), 1112.6395.

[325] J. S. Diaz, A. Kostelecky, and M. Mewes, Phys. Rev. **D89**, 043005 (2014), 1308.6344.

[326] P. F. de Salas, R. A. Lineros, and M. Tórtola, Phys. Rev. **D94**, 123001 (2016), 1601.05798.

[327] J. S. Díaz and F. R. Klinkhamer, Phys. Rev. D **93**, 053004 (2016).

[328] M. C. Gonzalez-Garcia and M. Maltoni, Phys. Rev. **D70**, 033010 (2004), hep-ph/0404085.

[329] IceCube, R. Abbasi *et al.*, Phys. Rev. **D79**, 102005 (2009), 0902.0675.

[330] J. N. Bahcall, V. Barger, and D. Marfatia, Phys. Lett. **B534**, 120 (2002), hep-ph/0201211.

[331] V. A. Kostelecky and N. Russell, Rev. Mod. Phys. **83**, 11 (2011), 0801.0287.

[332] Super-Kamiokande, K. Abe *et al.*, Phys. Rev. **D91**, 052003 (2015), 1410.4267.

[333] C. Gordon, W. Hu, D. Huterer, and T. M. Crawford, Phys. Rev. **D72**, 103002 (2005), astro-ph/0509301.

[334] A. L. Erickcek, S. M. Carroll, and M. Kamionkowski, Phys. Rev. **D78**, 083012 (2008), 0808.1570.

[335] J. P. Zibin and D. Scott, Phys. Rev. **D78**, 123529 (2008), 0808.2047.

[336] A. L. Erickcek, M. Kamionkowski, and S. M. Carroll, Phys. Rev. **D78**, 123520 (2008), 0806.0377.

[337] C. Giganti, S. Lavignac, and M. Zito, Prog. Part. Nucl. Phys. **98**, 1 (2018),

1710.00715.

[338] Particle Data Group, K. A. Olive *et al.*, Chin. Phys. **C38**, 090001 (2014).

[339] T. Ohlsson and H. Snellman, J. Math. Phys. **41**, 2768 (2000), hep-ph/9910546, [Erratum: J. Math. Phys.42,2345(2001)].

[340] IceCube, M. G. Aartsen *et al.*, Astrophys. J. **809**, 98 (2015), 1507.03991.

[341] S. L. Glashow, Phys. Rev. **118**, 316 (1960).

[342] IceCube, M. G. Aartsen *et al.*, Astrophys. J. **833**, 3 (2016), 1607.08006.

[343] IceCube, M. G. Aartsen *et al.*, (2017), PoS(ICRC2017)981.

[344] R. Catena and P. Ullio, JCAP **1008**, 004 (2010), 0907.0018.

[345] M. Pato, F. Iocco, and G. Bertone, JCAP **1512**, 001 (2015), 1504.06324.

[346] Q. Xia *et al.*, Mon. Not. Roy. Astron. Soc. **458**, 3839 (2016), 1510.06810.

Acknowledgements

First and foremost, I want to express my gratitude to Shin'ichiro Ando, my daily supervisor and promotor, for his supervision and support. I was given a lot of freedom – both in the choice of projects as in working on them – and encouragement to perform my research and solve occurring problems myself, while getting the help I needed when necessary. This freedom and trust in my scientific skills greatly contributed to my growth into a mature physicist.

I also would like to thank the GRAPPA institute and their members for being my scientific family for the last four years. Special thanks to Fabio Zandanel, with whom I collaborated closely during the first two years of my PhD.

I am grateful to the University of Amsterdam, and the Institute of Physics in particular, for hosting me during my PhD research.

Lots of thanks to Hans van Deurzen for his support and confidence in my abilities, and for the reassuring words: "Het komt wel goed". Without you I would be crocheting stuffed animals for some time already ;) .

The work presented in this thesis is part of the research programme of the Foundation for Fundamental Research on Matter (FOM), which is part of the Netherlands Organisation for Scientific Research (NWO). Part of the work was carried out on the Dutch national e-infrastructure with the support of SURF Cooperative.